DE TTK

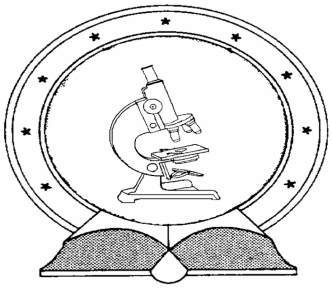

1949

Transmission of charged particles through a single glass microcapillary

PhD Thesis
Egyetemi doktori (PhD) értekezés

Réka Judit Bereczky

Supervisor / Témavezető
Dr. Károly Tőkési

University of Debrecen
PhD School in Physics

Debreceni Egyetem
Természettudományi Doktori Tanács
Fizikai Tudományok Doktori Iskolája

Debrecen, 2012

Prepared at
the University of Debrecen
PhD School in Physics
and
the Institute of Nuclear Research
of the Hungarian Academy of Sciences
(ATOMKI)

Készült
a Debreceni Egyetem
Fizikai Tudományok Doktori Iskolájának
Atom- és molekulafizika programja keretében
a Magyar Tudományos Akadémia
Atommagkutató Intézetében
(ATOMKI)

The work is supported by the TÁMOP-4.2.2/B-10/1-2010-0024 project. The project is co-financed by the European Union and the European Social Fund.

Ezen értekezést a Debreceni Egyetem Természettudományi Doktori Tanács Fizikai Tudományok Doktori Iskola Atom- és molekulafizika programja keretében készítettem a Debreceni Egyetem Természettudományi doktori (PhD) fokozatának elnyerése céljából.

Debrecen, 2012.

Bereczky Réka Judit

Tanúsítom, hogy Bereczky Réka Judit doktorjelölt 2006 - 2012 között a fent megnevezett doktori iskola Atom- és molekulafizika programjának keretében irányításommal végezte munkáját. Az értekezésben foglalt eredményekhez a jelölt önálló alkotó tevékenységével meghatározóan hozzájárult.
Az értekezés elfogadását javaslom.

Debrecen, 2012.

Dr. Tőkési Károly
témavezető

Transmission of charged particles through a single glass microcapillary

Értekezés a doktori (PhD) fokozat megszerzése érdekében a fizika tudományágban

Írta: Bereczky Réka Judit
okleveles biológia - fizika szakos tanár

Készült a Debreceni Egyetem Fizikai Tudományok Doktori Iskolája Atom- és molekulafizika programja keretében

Témavezető: Dr. Tőkési Károly

A doktori szigorlati bizottság:

elnök: Dr. ....
tagok: Dr. ....
Dr. ....

A doktori szigorlat időpontja: 2012. .....

Az értekezés bírálói:

Dr. ....
Dr. ....

A bírálóbizottság:

elnök: Dr. ....
tagok: Dr. ....
Dr. ....
Dr. ....
Dr. ....

Az értekezés védésének időpontja: 2012. .....

Contents

List of publications

Publications related to the thesis

1. **R.J. Bereczky**, G. Kowarik, F. Aumayr and K. Tőkési, Transmission of 4.5 keV Ar^{9+} ions through a single glass macrocapillary, Nucl. Instr. and Meth. B 267 (2009) 317.

2. **R.J. Bereczky**, G. Kowarik, C. Lemaignan, F. Aumayr, K. Tőkési, Transmission of 4.5 keV Ar^{9+} ions through a single glass macrocapillary. Journal of Physics 194 (2009) 132019.

3. **R.J. Bereczky**, B.S. Dassanayake, S. Das, K. Tőkési, J.A. Tanis, Guiding of electrons through a single glass macrocapillary. Journal of Physics 194 (2009) 132014.

4. **R.J. Bereczky**, G. Kowarik, C. Lemaignan, A. Macé, F. Ladinig, R. Raab, F. Aumayr, and K. Tőkési, Guiding Of Slow Highly Charged Ions Through A Single Mesoscopic Glass Capillary, CAARI 2010. AIP (2011) 119.

5. **R.J. Bereczky**, G. Kowarik, K. Tőkési and F. Aumayr, Sample holder for studying temperature dependent particle guiding, Nucl. Instr. and Meth. B. 279 (2012) 182.

6. G. Kowarik, **R.J. Bereczky**, F. Aumayr and K. Tőkési, Production of a microbeam of slow highly charged ions with a single microscopic glass capillary, Nucl. Instr. and Meth. B 267 (2009) 2277.

7. G. Kowarik, **R.J. Bereczky**, F. Ladinig, D. Schrempf, C. Lemell, J. Burgdörfer, K. Tőkési and F. Aumayr, The Way to Optimum Ion Guiding through Insulating Capillaries, arXiv: 1109.3953v1.

8. B.S. Dassanayake, S. Das, **R.J. Bereczky**, K. Tőkési, J.A. Tanis, Energy dependence of electron transmission through a single glass macrocapillary. Physical Review A 81 (2010) 020701(R).

9. B.S. Dassanayake, **R.J. Bereczky**, S. Das, A. Ayyad, K. Tőkési and J.A. Tanis, Time evolution of electron transmission through a single glass macrocapillary: charge build-up, sudden discharge, and recovery, Physical Review A 83 (2011) 012707.

10. B.S. Dassanayake, S. Das, A. Ayyad, **R.J. Bereczky**, K. Tőkési and J.A. Tanis, Charge evolution and energy loss associated with electron transmission through a macroscopic single glass capillary, Nucl. Instr. and Meth. B 269 (2011) 1243.

11. B.S. Dassanayake, S. Das, **R.J. Bereczky**, K. Tőkési, J.A. Tanis, Energy dependence of electron transmission though a single glass capillary. Journal of Physics: Conference Series 194 (2009) 132016.

12. B.S. Dassanayake, S. Das, **R.J. Bereczky**, K. Tőkési, J. A. Tanis, Time evolution of electron transmission through a single glass capillary. Journal of Physics: Conference Series 194 (2009) 132011.

13. Accepted ITS LEIF proposal, No: P09076A: The influence of external electric fields onto capillary guiding (2009).

Other scientific publications related to the PhD work

1. **R.J. Bereczky**, K. Tőkési, D. Varga, Z.M. Zhang and Z.J. Ding, Insulator nanocapillary production from biological sample, 2008 Surface and Interface Analysis 40 (2008) 584.

2. S.F. Mao, Z.M. Zhang, K. Tőkési, A. Csík, J. Tóth, **R.J. Bereczky**, Z.J. Ding, XPS study of nano thin films on substrate, Surface and Interface Analysis 40 (2008) 728.

3. M. Novák, **R.J. Bereczky**, Z.M. Zhang, Z. Ding J. Tóth, D. Varga, K. Tőkési, Energy loss spectra of iron. Surface and Interface Analysis 40 (2008) 522.

4. Z. Juhász, B. Sulik, R. Rácz , S. Biri, **R.J. Bereczky**, K. Tőkési, Á. Kövér, J. Pálinkás, N. Stolterfoht, Ion guiding accompanied by formation of neutrals in polyethylene terephthalate polymer nanaocapillaries: Further insight into a self-organizing process, Physical Review A 82 (2010) 062903.

5. K. Tőkési, I. Rajta, **R.J. Bereczky**, K. Vad, Investigation of MeV proton microbeam transmission between two flat plates - the cases of homogeneous metallic and insulator plates, Nucl. Instr. and Meth. B. 279 (2011) 173.

Invited talks

1. **R.J. Bereczky**, G. Kowarik, K. Tőkési and F. Aumayr: Guiding of slow highly charged ions through a single mesoscopic glass capillary, CAARI 2010 21st International Conference on the Application of Accelerators in Research and Industry, Denton, Texas, USA, 8-13 August 2010.

2. **R.J. Bereczky**: The effect of temperature on guiding of slow highly charged ions through mesoscopic glass, 5th Conference on Elementary Processes in Atomic Systems. CEPAS 2011. Belgrade, Serbia, 21-25 June 2011.

3. **R.J. Bereczky**: Controlling the guiding properties of mesoscopic glass capillaries for slow highly charged ions, ICPEAC, XXVII International Conference on Photonic, Electronic and Atomic Collisions, Belfast, Northern Ireland, UK, 27 July - 2 August 2011.

Educational publications

1. **R. J. Bereczky**, G. Kowarik, F. Aumayr and K. Tőkési, Guiding of HCl through a single macroscopic glass-capillary, ITSLEIF Newsletters 11 (2008)

2. K. Tőkési, **R.J. Bereczky**, Töltésüket megőrző parányok önterelődése makrokapillárisokban, Természet világa (2012) in press.

Other publications related to the PhD work

- 23 posters and 12 talks
- 15 ATOMKI Annual reports

Chapter 1

Introduction

The interaction of highly charged ions (HCI) with surfaces has been the focal point of many experiments in the last few decades. In recent years focus has shifted to the study of the transmission of charged particles through linear structures such as pores and capillaries.

The first experiment was conducted using metallic capillaries [1, 2] which was in good agreement with the theoretical interpretations [3-6]. Later insulator capillaries were introduced by Stolterfoht et al. [7] who firstly observed guided transmission of slow, highly charged ions through polyethylene terephthalate (PET, Mylar) nanocapillaries. In contrast to the case of metallic capillaries, the experiments with insulating ones showed not only directional guiding of the ions, even though the capillary axis is tilted with large angles compared to the direction of the incident beam, but also the remarkable fact that the ions keep their initial charge state as a consequence of a self-organized charge-up inside the capillary [7-12].

Following the pioneering work of Stolterfoht et al. several groups studied the ion guiding through insulating foils like Polyethylene-Terephthalate (PET) [8, 9], silicon dioxide (SiO_2) [10] and alumina oxide (Al_2O_3) [11, 12] nanocapillaries with aspect ratios around 100. Ikeda et al. [13] observed ion guiding through a single tapered glass capillary. For nanocapillaries in foils, depending on the wall material and the corresponding production technique, large differences have been found in the transmission properties. The SiO_2 capillaries were obtained by thermally oxidizing a membrane of silicon nanocapillaries, fabricated by an etching process, whereas the PET foil was first irradiated by heavy highly charged ions and after the irradiation the capillaries were produced by

chemical etching of the ion tracks using NaOH. While the angular distribution of the HCIs passing through PET capillaries was very broad, and a significant fraction of the projectiles was transmitted through the capillaries even for tilt angles up to 25° with respect to the incident beam direction, the angular distribution of the guided beam for the case of SiO_2 nanocapillaries was very narrow, with full widths at half maximum (FWHM) of $\sim 1°$. In the case of transmission of HCIs through anodic alumina capillaries, where the sample was prepared by electro-chemical oxidization of alumina foils, it was found that the FWHM of the angular distribution of the transmitted ions was about 4.3° and nearly independent of the tilt angle. This corresponds to much larger angular broadening than can be expected from the aspect ratio, as was also found for the PET nanocapillaries.

During the latest experiments the guided transmission of low energy electrons through Al foils with randomly distributed capillaries was also observable through PET [14] and Al_2O_3 [15] capillaries. Secondary electron emission coefficients for electron impact with a few hundred eV energy may suggest even positive charge-up resulting in attraction rather than repulsion from the surface. This suggests that a fundamentally different guiding scenario prevails.

Although during the past few years many research groups joined to this field of research and carried out various experiments with insulator capillaries many details of the interactions remained unknown. For the first time insulating foils with randomly distributed capillaries were used, which foreshadow many uncertainties both in experimental and theoretical points of views. For example, it is not possible to ensure a perfect parallelism of the nanocapillaries in the foil. Another significant problem is that the collective effect of all the neighbouring tubes has to be taken into account. Therefore to avoid these difficulties in my PhD work I made systematic measurements on the guiding of charged particles through a single, cylindrical shaped glass capillary. Recently it is technically not possible to perform measurements with a single nanotube. Partly because it is difficult to produce such a sample, and partly because it is challenging to carry out the measurements with it. Therefore we use capillaries with microscopic dimensions.

My dissertation is organized as follows: in the second chapter I briefly summarize the theoretical background of the charged-particle guiding phenomenon. In the third chapter I describe the experimental methods that were used. In the fourth chapter I present the new results of my PhD work. The dissertation is finished with an outlook and the bibliography.

Chapter 2

Interaction of charged particles with capillaries

In this section I give a short overview of the recent theoretical description of the guided transmission of charged particles through insulating nanocapillaries. In the descriptions the charged projectiles are considered with charge state q and energy E impinging on a capillary target with a tilt angle with respect to the surface normal and the capillary axis. A schematic view of projectile trajectories inside the nanocapillaries considered is given in Figure 2.1. Capillaries with a length L and diameter d have aspect ratios L/d of 50 - 150, with the corresponding geometric opening angles $\gamma_0 \approx 0.25^\circ$ - 1°. The dielectric material is characterized by a static dielectric constant of ε_r. Front and back sides of a capillary target are usually covered by a thin layer (several tens of nanometers) of conducting material which prevents a global charge-up of the whole target during beam exposure. For the close-contact interaction between the charged projectile and a surface we distinguish two kinds of projectiles: electrons and ions, in particular HCI. Irrespective of the projectile, the time structure of charged particle guiding is linked to the charge-up. Therefore, observables such as the transmission rate evolve on the same time scale, being of the order of minutes. When charge-up is negligible even a time-independent approach is sufficient.

2.1 Theoretical background of ion guiding

What happens when a HCI passes through an insulating capillary? Upon impact on the internal capillary wall HCI undergo a sequence of charge transfer process leading eventually to full neutralization. The secondary electron emission coefficient is low for the HCI parameters (velocity, charge state) considered in this work.

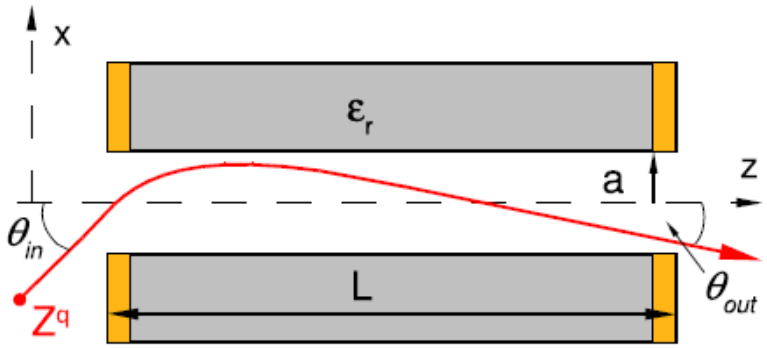

Figure 2.1: Schematic view of charged projectile guiding through capillaries.

Moreover, as long as secondary electrons do not leave the nanocapillary, the aggregate charge deposited by the HCI impact is equal to its initial charge state q. In the simulation it is assumed that q elementary charges are Gaussian distributed on the surface with a width of distribution r_d 1000 a.u [18, 19].

In equilibrium, a single principal charge-patch is formed around the impact region near the entrance of the capillary (in the first 10-15 % of the capillary) deflecting subsequent projectiles, see Figure 2.2. Projectiles impact around a arclength of $b/(2\pi a) = 0.5$. Charge is accumulated near the exit only at later stages, i.e. for a charge deposition on the target $>$ 200 nC. This secondary

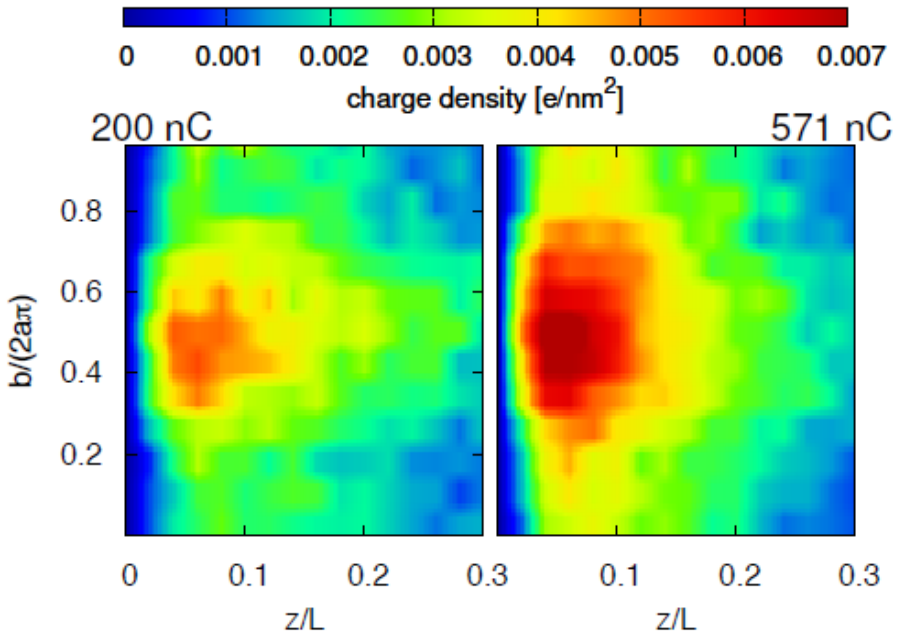

Figure 2.2: Close-up of the charge density on the internal wall near the capillary entrance for two different moments in time (different charge depositions on target) as indicated in the figure.

charge patch is, in fact, is spread rather wide. Its center is situated on the side of the capillary that is opposite to the principal charge patch.

Figure 2.3 shows the secondary charge-patch near the capillary exit during its formation in time. Note that the color scale has been adapted to the much lower charge deposition as compared to the principal patch (Figure 2.2). Early simulations of HCI guiding have already suggested the possibility of forming charge patches additionally to the main charge patch always present. Although the former are weak as compared to the principal patch, they further deflect the trajectories well inside the capillary. Analogously to the principal patch the secondary patch(es) build up in time, too, and during their formation the transmitted beam is thus moving. Theoretical work has very early suggested

the existence of two classes of guided trajectories - the first class being deflected only once at the primary charge patch as well as a second class containing those that are deflected additionally near the exit. The existence of the second class has been predicted to depend on the geometry of the capillary. Although the time-dependence of the beam of the transmitted profiles has not been explicitly discussed at that time, it is evident that the formation of the second charge patch supporting the second class of trajectories is delayed relative to the build-up of the principal charge patch. Once equilibrium is reached the transmitted beam becomes stable and centered around the capillary axis.

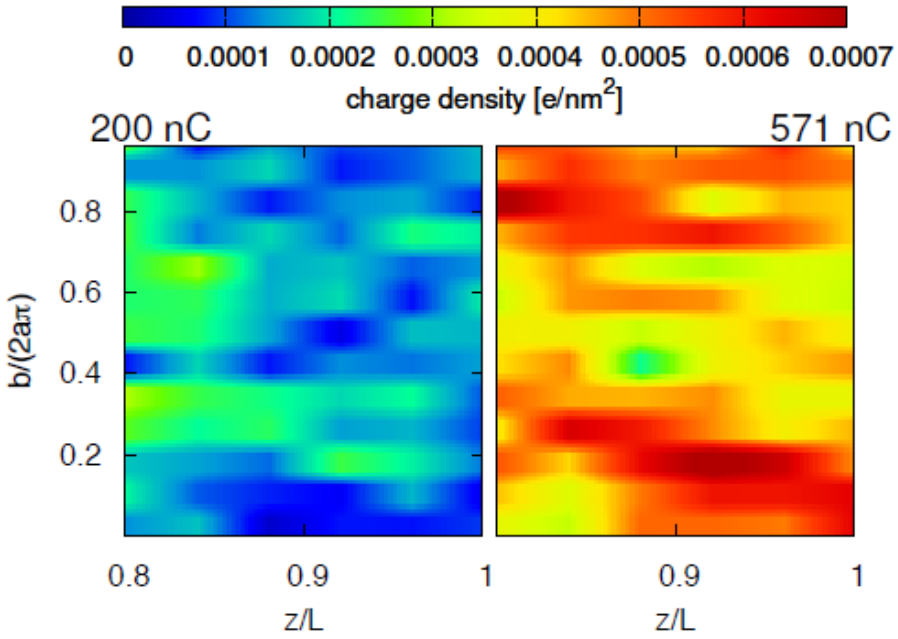

Figure 2.3: Close-up of the charge density on the internal wall near the capillary exit for two different moments in time (different charge depositions on the target) as indicated in the figure. Note the different color scale as compared to Figure 2.2).

2.2 Theoretical background of electron guiding

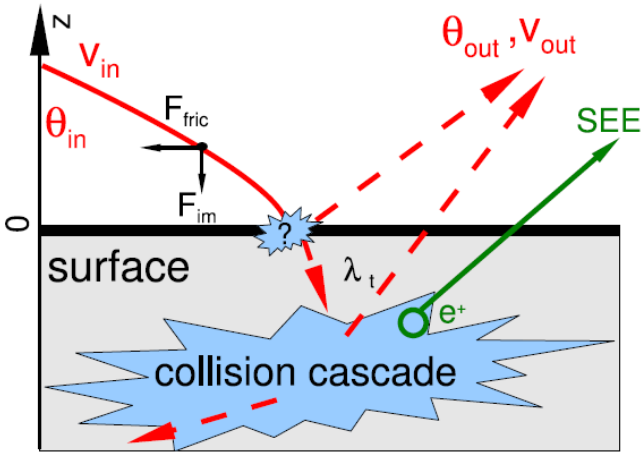

Figure 2.4: Scenario of electron-surface interaction with the internal capillary surface. The notations can be found in the text.

According to our recent knowledge the following scenario (see also schematic view in Figure 2.4) applies when an electron approaches (with a velocity v_{in} and incoming angle Θ_{in}) the surface of the internal wall of a capillary: even in the absence of a charged surface, electrons are attracted to the surface by their image force. Within the framework of dielectric response theory from which the image force is deduced, also a decelerating force parallel to the surface emerges. This so-called friction force is related to the various surface excitations, like the excitation of surface plasmons. In contrast to the image force, above-surface energy loss increases with the velocity of the projectile. At close contact with the planar surface potential electrons may be reflected coherently in specular direction. Otherwise, they are transmitted into the bulk. In such a case electron transport inside a solid needs to be described. As a result of electron transport incident projectiles can be absorbed in the solid or are reemitted into

the vacuum. Both processes may be accompanied by the emission of secondary electrons (SEE) which leaves a positively charged hole behind. Charge-up is found to be significantly different from HCI guiding [17, 18]. Its influence being in many cases negligible for larger tilt angles, charge-up suppresses transmission through an untilted nanocapillary. This effect can be attributed to the attraction of projectiles towards the internal wall after a positively charged patch on the internal wall (caused by secondary electron emission) has developed. Above-surface loss is found to be crucial for a full description of transmission through untilted capillaries because it represents the dominant inelastic process for 0°. At larger angles of incidence this inelastic process is rather unimportant.

The trajectory of the incoming electron is influenced by the Coulomb fields F_{C} of the charged surface (which can be both positive or negative) and its own dynamical image force F_{im} (which is always attractive but weak at high projectile speeds). Furthermore, the response of the target material to the external charge leads to a friction force F_{fric} which decelerates the electron. Upon impact on the surface the electron can either be coherently and elastically reflected by the surface potential of the surface, a process which contributes at small perpendicular velocities, or it can penetrate to the material initiating a collision cascade involving elastic large-angle scattering at atomic cores as well as small-angle scattering due to inelastic losses from scattering events at electrons in the target. Upon penetration of the surface the energy lost in scattering events along the trajectory is transferred to low-energy secondary electrons which may also escape from the surface and contribute to both the charging of the surface as well as to the detected electron count. Eventually, primary and secondary electrons may escape from the surface which influences the charge balance on the capillary wall. If no electron escapes a negative charge is deposited, if only one electron leaves the surface, the surface remains neutral, if more than one electron escapes a positive charge is left behind [16]. We note that, however, we still do not have clear evidence how did the surface of the capillary charge up using electrons.

We need further investigations to check it.

Chapter 3

Experimental methods

3.1 Ion guiding measurements

3.1.1 The ECR-ion source: SOPHIE

The ECRIS (Electron Cyclotron Resonance Ion Source) uses electron cyclotron resonance to heat a plasma. The plasma is created and heated by microwaves with a frequency corresponding to the strength of a magnetic field applied from the outside. This field is provided by strong permanent magnets in a hexapolar configuration and provides a necessary confinement of the plasma. For electrons the cyclotron frequency is given by:

$$\omega_{\mathrm{ECR}} = e \cdot \frac{B_{\mathrm{ECR}}}{m_{\mathrm{e}}}, \tag{3.1}$$

where e is the elementary charge, m_e is the mass of the electron and B_{ECR} is the exterior magnetic field.

Typical microwave frequencies for an ECRIS are in the range from 2.45 to 28 GHz. Microwaves with the angular frequency ω_{ECR} excite the electrons at their cyclotron resonance frequency. Inside the plasma, the heated electrons collide with the gas molecules and progressively ionize them. ECR ion sources can produce not only singly charged ions with high intensities, but multiply charged ions even highly charged ions.

SOPHIE (SOurce for Production of Highly charged Ions using ECR) is a 14.5 GHz ECRIS [20] for production of highly charged ions with a plasma-confining magnetic field. Figure 3.1 shows the schematic drawing of the ion

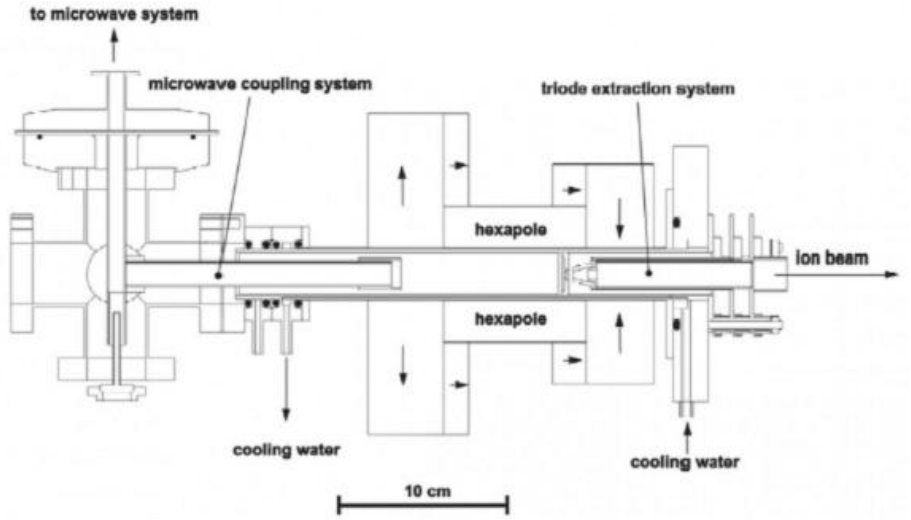

Figure 3.1: Schematic drawing of the ion source SOPHIE

source SOPHIE. The magnetic confinement field is generated by four permanent magnet rings and a Halbach-type hexapole magnet with an outer diameter of 80 mm. Two of the rings are axially and two are radially magnetized and thus provide an axial mirror field with a maximum induction of about 0.9 T. Microwave power with a frequency between 12.75 and 14.5 GHz is transmitted from ground potential via an insulating window into the water cooled plasma chamber fitted with an aluminum liner. The ECRIS is fully computer-controlled by a LabVIEW based program.

3.1.2 The beamline: MUSIC

The beamline MUSIC (MUltipurpose Solid-target Irradiation Chamber) is used for various kinds of experiments, for example irradiation experiments concerning the production of nanostructures on insulating surfaces, or electron emission measurements.

The vacuum system is able to reach the ultra-high vacuum regime by means of two turbo-molecular pumps. The pre-vacuum is provided by a rotary vane

pump equipped with a zeolite trap, a compressed air regulated valve and a vacuum valve. The high-quality ion beam is provided by a beam collimation track. The collimation track is able to collimate the ion beams to 250 micrometer diameter and about 2 mrad divergence. It electrostatic lens system, to decelerate and focus the beam. Scanning plates scan the target area by means of an electric field, that varies with time. They are mounted on the last element of the deceleration lens. Two quadrupoles of deflection plates for beam guiding including a set of plates at the end for scanning the target. A motorized and computer-operated x-, y-, z-, φ-manipulator. The four main movements are controlled by stepper motors.

3.1.3 The CSIGA (Capillary Slow Ion Guiding Apparatus)

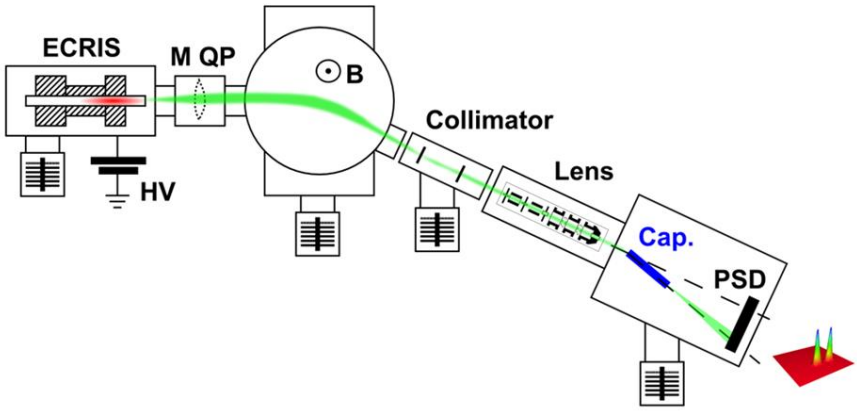

Figure 3.2: Schematic view of the experimental setup. The ion source (ECRIS) provides a variety of ion species, which are mass-charge-selected in a magnetic field and focused by magnetic quadrupol lenses (M QP) onto an entrance aperture. A system of electrostatic deflection plates and lens elements provides the final beam of 3 mm diameter at the capillaries entrance. The PSD is located excentrically roughly 18 cm behind the capillary.

The glass capillary was positioned in a differentially pumped UHV chamber, with a residual pressure better than 5×10^{-9} mbar. Figure 3.2 shows a schematic view of the experimental setup. The beam diameter at the entrance of the capillary could be estimated to roughly 3 mm with an opening angle of full widths at half maximum (FWHM) of 2.2°. Approximately 18 cm behind the entrance of the capillary, a position sensitive detector (PSD) mainly consisting of a Chevron-type micro-channel-plate and a wedge-and-strip anode is used to record the transmitted ions [21]. The capillary holder itself could be moved in x, y and z-direction with high accuracy by stepper motors. Also the tilting against the beam axis in the horizontal plane (Ψ-direction) was stepper-motor controlled, allowing step sizes as small as 0.02°. The location of the turning axis was chosen as way to cross the entrance of the capillary in order to keep the beam facing side of the capillary in a fixed position when turning. When moving the capillary out of its vertical position, a reference intensity could be measured by allowing ion passage through a hole of known diameter ($d = 0.5$ mm) directly onto the channelplate detector. This direct beam measurement was also used to estimate the initial angular distribution entering the capillary. Tilting measurements were performed such way, that the discharged capillary was positioned axially with respect to the beam, and from there the tilt angle was increased stepwise into one direction. The other tilt direction was either measured starting again from the straight position with a discharged capillary or by returning stepwise from the outermost deflection from the first tilt direction into the other one, passing the straight position in a charged-up condition.

3.2 Electron guiding

The electron guiding experiments were carried out in the tandem Van de Graaff accelerator facility at Western Michigan University (the accelerator was not used). The scheme of the experimental setup is shown in Figure 3.3. A commercially available tungsten filament was used as the source of electrons of the desired energy. The transmitted electrons were analysed by an electrostatic parallel-plate analyser placed few centimeters behind the sample. Electron events were counted using a channel electron multiplier (CEM) coupled to the analyser. The background pressure in the scattering chamber was $\sim 10^{-6}$ torr. A μ-metal sheet was used to minimize the magnetic field effects inside the chamber.

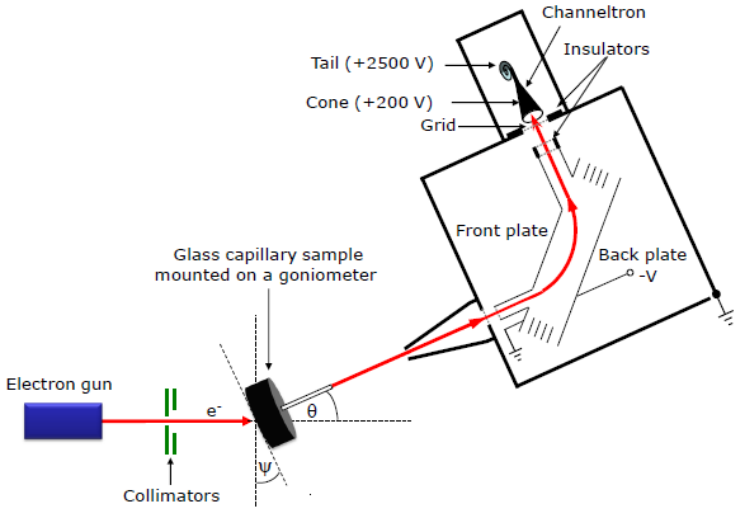

Figure 3.3: Schematic diagram of the experimental apparatus. Ψ and Θ are the sample tilt and observation (spectrometer) angles measured with respect to the incident electron beam direction.

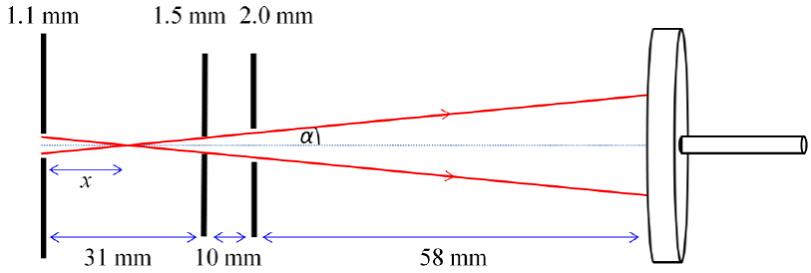

Figure 3.4: Arrangement of the setup. The diameters of the apertures are shown above the corresponding aperture. Blue arrows indicate the distances between different objects.

A LabView program was used to communicate with electronics as well as to control the electronic devices to acquire data. The beam which comes through the 1.1 mm exit aperture of the electron gun was collimated by a set of two apertures of diameters 1.5 and 2.0 mm, respectively (see Figure 3.4). The beam collimation can be found from the geometry of the setup, $\Gamma_{\text{coll}} = 2.16^{\circ}$. The direct transmission occurs when the transmitting electron beam does not interact with the inner wall of the capillary and the electrons travel on a straight line path. Direct transmission takes place from $\Psi = 0°$ as far as angle Ψ^*, which is specified depending on the sample geometry and beam collimation. When the tilt angle is increased from its zero position, the direct transmission gradually decreases and finally drops to zero when overlap between the entrance and exit of the capillary no longer exists. The electron beam was allowed to strike the sample and was controlled by focusing and vertical/horizontal steering of the beam. The sample was mounted in a goniometer with two rotational degrees of freedom, namely, tilt angle Ψ rotation about a vertical axis (from -20° to 20°) and azimuthal rotation about a horizontal axis (from 0° to 360°) with respect to the incident beam, for precise positioning. The goniometer was controlled using the LabView software. Figure 3.5 is a schematic diagram of the spectrometer and the CEM. Two spectrometers were employed for the experiment which had similar energy resolutions but different angular resolutions. Both the spectrometers were made with 45° plane mirror analysers which can deflect incoming electrons by 90° towards the channel electron multiplier (CEM) as shown in Figure 3.5. It was possible to rotate the spectrometer about the vertical axis of

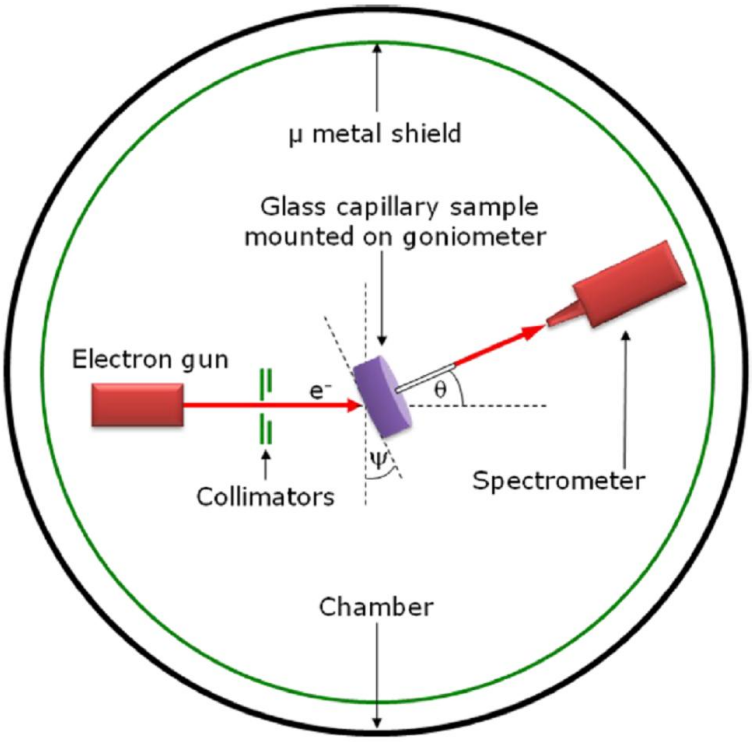

Figure 3.5: Schematic plot of the experimental apparatus. The ψ and Θ are the sample tilt and observation (spectrometer) angles measured with respect to the incident electron beam direction. The back plate of the parallel plate spectrometer was negatively biased to select the desired energy of the transmitted beam through the sample.

the goniometer with respect to the incoming beam (from $\Theta = -30^{\circ}$ to $+30^{\circ}$). The spectrometer had several modes of operation depending on desired energy resolution and electron energy range to be investigated. In the presented experiments low resolution and high energy mode of the spectrometer was used. The energy (E) of the deflected electrons was determined by the voltage applied to the spectrometer plates.

The spectrometer used in the experiments had a spectrometer constant (the quotient of the potential on the electrodes and the energy of the focused electrons) of 0.60. According to the geometry of the spectrometers employed in the experiment, the energy resolution was found to be 0.03 (3%) for both of them. By supplying the desired voltage to the back plate of the spectrometer (using the LabView program), only electrons with the preferred energy are deflected by 90 and sent towards the CEM. An electron energy spectrum can be obtained by stepping the back plate voltage, allowing electrons with different energies to enter the CEM through grounded grids as the back plate voltage is varied. The electrons transmitted through the grid were then counted using a channel electron multiplier. The CEM used in the experiment was Burle model 4821. The cone of the CEM was biased to +200 V at the entrance for initial acceleration of the electrons and to +2700 V at the tail for optimal detection efficiency. The CEM pulses were normalized mostly with respect to the current as read on the sample (goniometer) or to the current on the collimator.

A block diagram of the electronics used for the experiment is shown in Figure 3.6. Even though there are three high voltage power supplies in the Figure 3.6, only one was employed as just one spectrometer was used at any particular time for all measurements. A LeCroy 2415 High Voltage Power Supply was utilized to provide the appropriate voltages to the spectrometer plates. The stepper motor which was used to precisely position the whole spectrometer assembly (with respect to the beam direction) was controlled by a Joerger SMC-R Stepping Motor Controller. The exact position of the spectrometer was verified with a Joerger CS-5 Optically Isolated Input Register. The signal received from the CEM was normalized with respect to the current as read on the sample.

Before collecting the angular dependence data for electron transmission, the zero position of the sample with respect to the incoming beam direction was set by varying the tilt angle Ψ, azimuthal angle Φ, and spectrometer (observation) angle Θ in small steps until the maximum transmission of electrons through the capillary was obtained. Then these three angles were redefined as the zero position ($\Psi = \Theta = \Phi = 0°$). The spectrometer used for this part of the experiment had an angular resolution of $\sim 2.4^{\circ}$.

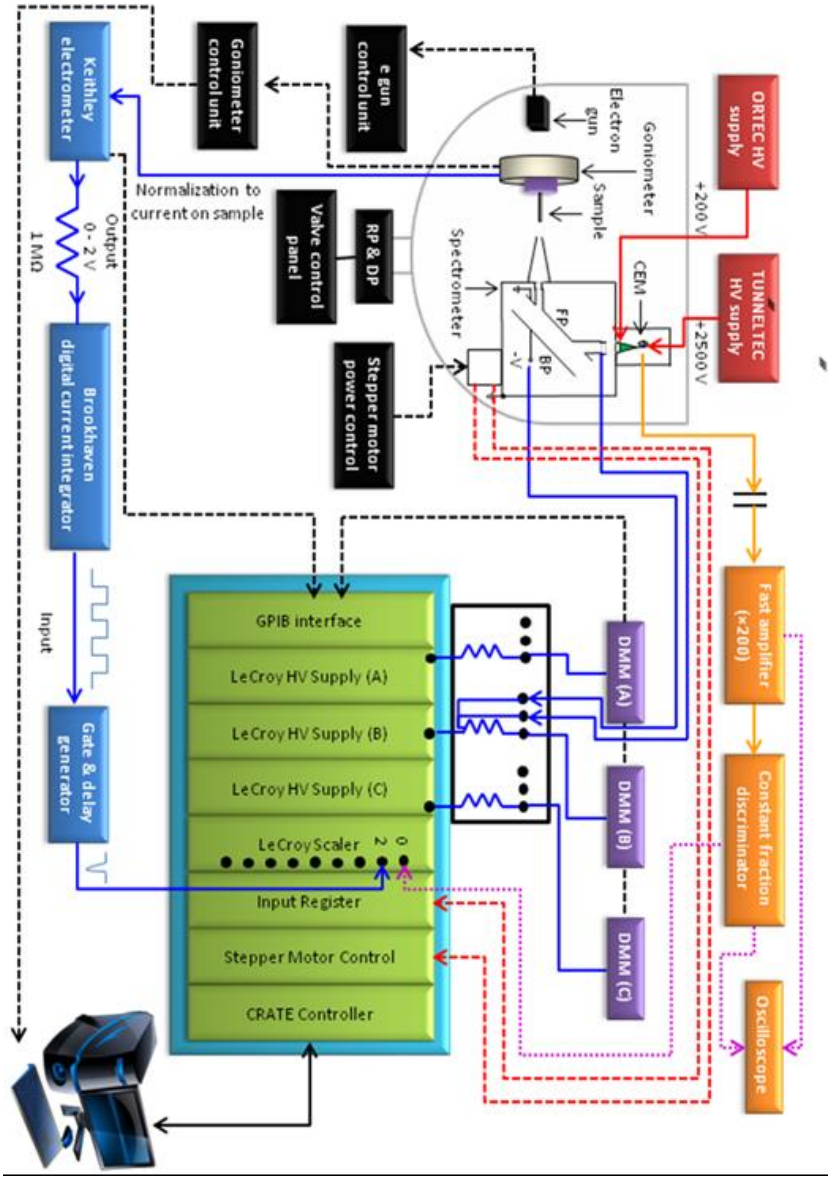

Figure 3.6: Block diagram of the electronics, which was used for the electron guiding experiments.

Chapter 4

Results

4.1 New developments for the capillary experiments

4.1.1 Sample preparation

The key issue of our capillary measurements is the preparation of the sample. During our measurements we used single, macroscopic-sized DURAN borosilicate glass tubes. Borosilicate glass is a type of glass with the main glass-forming constituents silica and boron oxide. DURAN has the following approximate composition: SiO_2 (80.6%), B_2O_3 (13.0%), Na_2O (4.0%), and Al_2O_3 (2.3%). Some of the material properties of borosilicate are given in Table 4.1.

The material is known for its low chemical reactivity, except in the presence of hydrofluoric acid, hot phosphoric acid, and hot alkalis. The low thermal expansion and high working temperatures (~ 240 °C) make it a good candidate for studying the electron transmission process even at higher beam energies.

To the preparation of the appropriate capillary sample borosilicate tubes are heated up and pulled apart on both ends with a constant force until the chosen smaller diameter is obtained. The diameter of the final product can be controlled by tuning the temperature and the force applied. We used capillaries, with the length of l $\approx$ 14 mm and the inner diameter of d $\approx$ 0.17 mm. The length to inner diameter ratio (aspect ratio) of a capillary is between 70 and 100. A special diamond cutter is used to cut the capillary to get a suitable

Table 4.1: *Properties of the borosilicate glass*

Property	Values
Density	2.23 g/cm^3
Transformation temperature	525°C
Softening point	825°C
Annealing point	560°C
Maximum short-time working temperature	500°C
Modulus of elasticity E (Young's modulus)	64× 103 N × mm^{-2}
Poisson´s ratio (μ)	$0,20$
Thermal conductivity at 90 °C	$1,2W\times$ $m^{-1}\times$ K^{-1}
Thermal expansion coefficient	$3.3 \times 10^{-6}/K$
Dielectric constant (ε)	$4,6$

length. To determine the inner diameter of the tube an optical microscope is used.

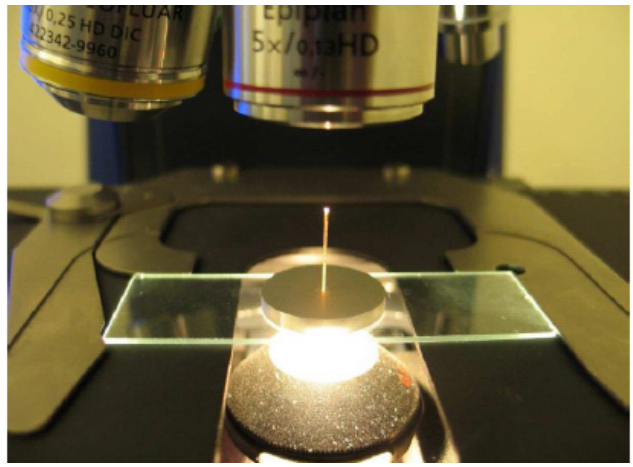

Figure 4.1: Photo of a fixed capillary sample.

For the systematic measurements with the new type of capillary I developed a process to prepare the appropriate samples. A photo of the sample can be seen in Figure 4.1.

The procedure of the sample preparation is as follows:

- I fixed the capillary into an aluminium disk holder. The capillary is perpendicular to the surface of the holder.

- I covered the samples and their holder with graphite to carry away any excess charge deposited on them, and to guarantee symmetry and uniform charge transport. Graphite is used during the temperature dependent measurement to fix the capillary in its position and to ensure good electrical as well as thermal contact between the glass and the surrounding metal parts.

- The critical point of the guiding measurements with capillaries is the precise alignment of the capillary and the beam axis. Therefore I designed a special tool to assure the perpendicularity of the capillary sample to the sample holder.

4.1.2 Analysis of the glass capillary with XPS and profilometer

XPS measurements were performed on 3 different kinds of capillaries to analyze the composition and the cleanness of the glass sample. Figure 4.2 shows the Al Kα excited XPS spectra measured from the microcapillaries which were used during our measurements.

The XPS spectra were measured by using the ESA-31 home-built spectrometer [22]. It consists of a 180° hemispherical electrostatic analyser with a 250 mm working radius, floatable up to 10 kV and completed with a multielement zooming electron-optical lens. The analyser works in the pass energy range of 10 - 500 eV with $\Delta E_{\mathrm{an}}/E_{\mathrm{pass}} \approx 5 \times 10^{-3}$, and the energy resolution ΔE_{an} is 1.5 eV at 5 keV electron energy. The base pressure of the sputtering system and the argon pressure during the deposition were 1×10^{-7} mbar and 3×10^{-5} mbar, respectively. Prior to the measurements *in situ* cleaning of the sample surface was performed using Ar^{+} ion sputtering at 2 keV kinetic energy. During the measurements, the vacuum was better than 3×10^{-9} mbar.

The spectra were normalized to the height of the oxygen peaks. The blue curve (a) in Figure 4.2 was measured on the uncleaned outer surface of the capillary. This capillary sample was cleaned neither before putting it into the chamber, nor in the chamber before the XPS measurement. The red curve (b) in Figure 4.2 shows the composition of the pure glass sample (outer surface). This was taken after cleaning the sample with isopropanol and bombarded with 6 keV Ar^{2+} ions for 2 minutes with the current of 100 - 150 μA. That is the reason

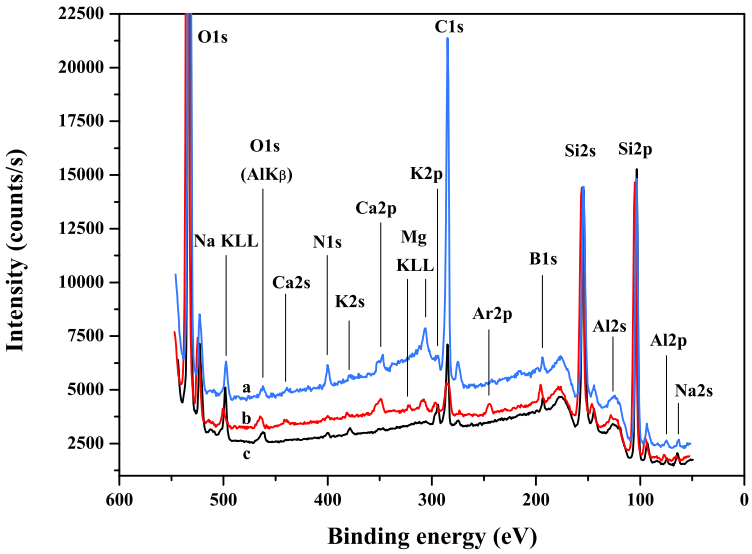

Figure 4.2: XPS analysis of the inner surface of the glass capillary samples.

why the argon peak is visible in this spectrum. The black curve (c) in Figure 4.2 shows the uncleaned, inner surface of the capillary. Also the impurities and composition of the sample that we used. We can conclude that the spectrum from the uncleaned inner surface of the capillary is close to the precisely cleaned sample that which was bombarded later on (the red, (b) spectrum in Figure 4.2).

The roughness of the inner surface of the capillary was measured with a profilometer. Figure 4.3 shows the roughness of the inner surface of the sample. We found that the roughness of the sample is ~ 3.2 nm.

4.1.3 The temperature dependent guiding apparatus

The experimental setup at TU Wien which was used so far to investigate the transmission of HCIs through a single glass capillary has only slightly been

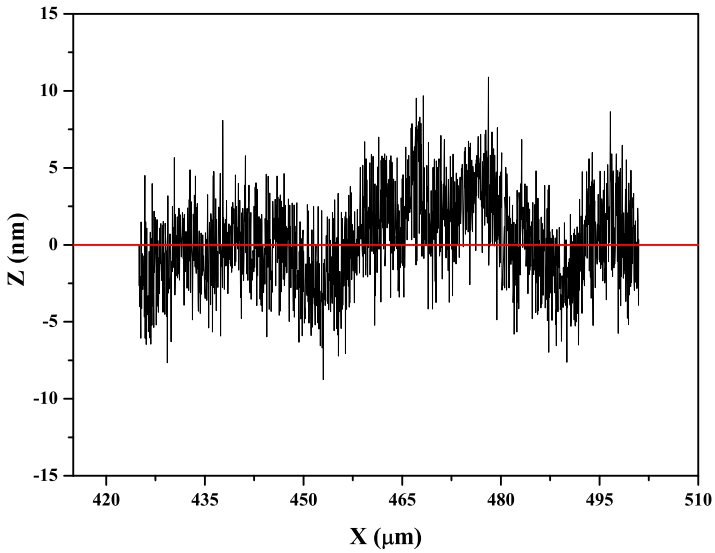

Figure 4.3: Analysis of the roughness of the capillary's inner surface with profilometer.

modified to allow temperature dependent measurements with the glass tube. Figure 4.4 shows the schematic view of the beam line with the modifications.

For the temperature dependent guiding experiments a completely new heatable sample holder was designed [67]. We developed and built such a heatable sample holder to allow accurate and reproducible studies of the temperature dependence of the ion guiding effect. Figure 4.5 shows the modified chamber with the temperature regulated sample holder.

The target holder (for an exploded view see Figure 4.6) consists of two main parts, the upper and the lower plates. The two plates of the sample holder, which function as an oven, are made of copper. These parts surround the capillary in order to guarantee a uniform temperature along the whole tube. The temperature of the copper parts is monitored by a K-Type thermocouple. Stainless steel coaxial heaters surrounding the oven are used for heating. The heating power

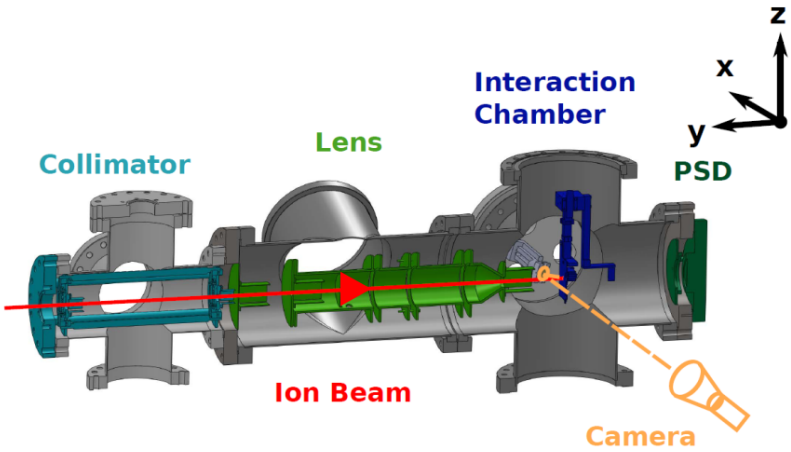

Figure 4.4: Cut through the beamline. The beam enters through the lens system and hits the sample holder. A mirror is installed in front of the capillary, in order to have a direct line of sight into a video camera. High magnifying optics is used to monitor the entrance position.

of up to a few watts is regulated by a proportional, integral, derivative (PID) controller. Charge state analysis of the transmitted ions is possible by means of a pair of electrostatic deflector plates located near to the exit of the capillary. Transmission rates are recorded after dynamical equilibrium is reached.

At first the idea was to heat the capillary sample just with one copper plate, taking advantage of the good thermal conductivity of the copper. Figure 4.7 shows the result of a simulated temperature distribution when only one of the surrounding plates was heated. Both the three-dimensional design of the sample holder and the simulation of the temperature distribution have been made with the SolidWorks software package. Our results clearly show that the temperature distribution is not uniform enough. Therefore heating of both plates is needed.

The upper plate is electrically isolated to allow the measurement of the current of the incident ion beam. On the upper plate two large holes are prepared with the diameter of 12 mm. Onto the back part of the upper hole an aperture with a diameter of 100 μm is mounted (see Figure 4.6). The aperture is centered with respect to the capillary. On the lower hole a reference aperture of similar

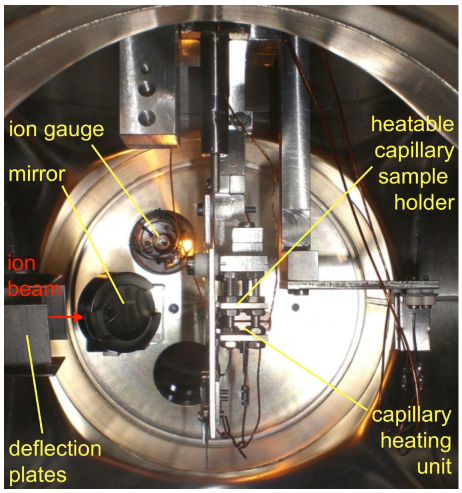

Figure 4.5: Photo of the target chamber showing the capillary heating unit mounted on the new sample holder and parts of the mirror assembly.

size is mounted, which can be brought into the axis of the beam by moving the sample holder 25 mm upwards. The entrance aperture position is matched with the manipulator rod's rotation axis, so that tilting the beam does not influence the lateral position of the aperture.

The lower plate of the holder is also electrically isolated. The pressure onto the capillary by the copper plates can be adjusted with the adjusting nuts. The capillary itself is covered by graphite on its outside surface to guarantee symmetry and uniform charge transport. This graphite is also used to fix the capillary in its position and to ensure good electrical as well as thermal contact between the glass and the surrounding metal parts.

Cooling of the capillary was achieved by a copper feed-through connected to a liquid nitrogen bath outside the UHV chamber. This solution allows us to change the temperature of the sample from -30°C up to 90°C.

In the case of ion guiding measurements one of the crucial points is the accurate determination of the position of the sample and the reproducibility of positioning it with respect to the beam axis. Therefore we developed a method for the exact definition of the lateral position. A high-magnification

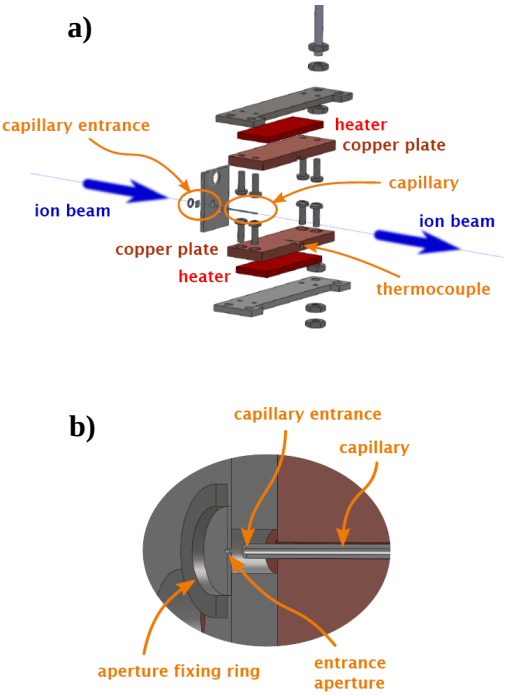

Figure 4.6: Details of the temperature regulated capillary holder developed in order to study the effect of electrical conductivity on guiding of slow highly charged ions through mesoscopic glass capillaries. (a) exploded view of the heating unit and (b) a cut through of the entrance region. For further details see text.

video camera has been installed, which provided real time images and was fixed outside of the vacuum chamber.

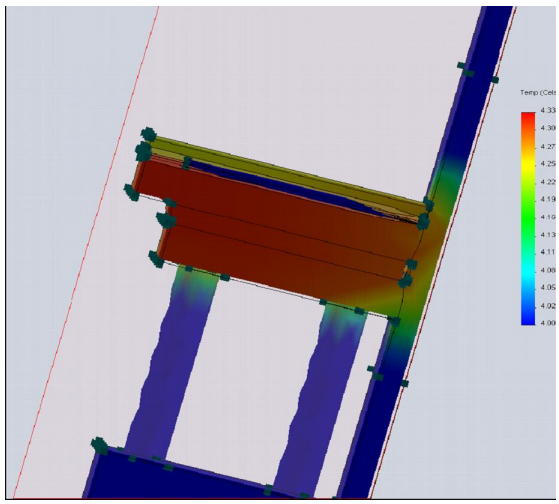

Figure 4.7: Simulation of the temperature of the heated sample holder.

4.1.4 Investigation of the conductivity of the borosilicate glass

We measured the conductivity of a flat borosilicate glass sample as a function of the temperature. We wanted to gain more information about this behavior, because we use the conductivity of the glass to control the guiding properties of the capillary. The basic electrical circuit is shown in Figure 4.8. Graphite electrodes in a circular shape were applied to the specimen [41]. On one side, one single electrode covers some area, faced on the other by a smaller circular electrode. It is surrounded by a ring of the same outer diameter, as the electrode on the opposite side.

The bulk conductivity is measured by grounding the outer ring, and applying a voltage between the other electrodes. The current is measured with a pico-ampere-meter (Keithley 6485). We applied voltages between a few volts and 1 kV with an external power supply (Hewlett Packard 6516A). To determine the surface conductivity, the measuring voltage is applied between the ring and the inner circular electrode. A second kind of geometry was also used, where the electrodes were applied to the inside and the outside, respectively,

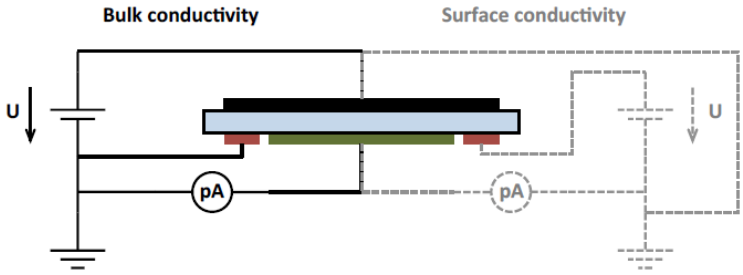

Figure 4.8: Schematic illustration of the electrical circuit used for measuring the bulk conductivity (solid lines) and the surface conductivity (dashed lines). The borosilicate sample (blue) is covered on one side with a circular electrode (black), on the other side a ring electrode (red) is surrounds a central circular electrode (green).

of a glass tube. There again, three electrodes were used to determine the bulk and surface conductivity independently. From the applied voltage U and the measured current I, we obtain the specific conductivity, σ_s as

$$\sigma_b = \frac{s}{A}\frac{I}{U}, \tag{4.1}$$

where s denotes the sample thickness and the effective area A, corresponding the overlap between the two opposite electrodes. For the surface conductivity one obtains

$$\sigma_s = \frac{g}{l}\frac{I}{U}, \tag{4.2}$$

where the gap distance between the outer ring and the inner circular electrode is denoted by g, and the effective circumference l, corresponding to the inner diameter of the outer ring of the electrode. Similar laws can be found for the tube-shaped sample geometry, which is not shown here in more detail.

In order to avoid any influence by the surrounding, the measurements were actually performed in vacuum. Therefore, stainless steel wires held the specimen

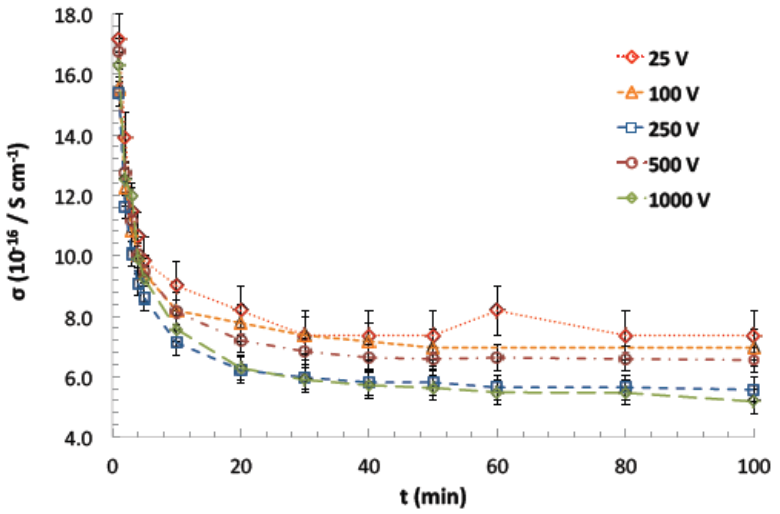

Figure 4.9: The measured bulk conductivity as a function of time. t=0 corresponds to the time when the voltage is turned on.

inside a standard T-piece, which was evacuated prior to the measurements using a turbo-molecular pump. The vacuum vessel was heated and cooled later on, respectively, from the outside by electrical heaters on the one hand, or a fridge on the other. By this, a temperature range from about -18°C to 90°C was covered. The actual sample temperature was monitored by a K-type thermocouple, which was attached to the glass sample.

When applying a voltage to the sample, the measured current starts to drop immediately, showing some exponential-like behavior as can be seen in Figure 4.9. An equilibrium value is reached after a few hours. Charge transport in glasses is a complex phenomenon, mainly based on the cations in the glass. The observed time dependence can be attributed to polarization effects [42].

The effect shows a weak dependence of the applied voltage. For the conductivity measurement presented, a voltage of 100 V was applied; this has been chosen as a compromise between avoiding high field effects on the one hand and electronic noise problems in the very low current regime, on the other. A comparison with total conductivity data of another borosilicate (Pyrex, Type 7740) from the literature [43] shows similar behavior as a function of temperature, but of a slightly different magnitude. Concerning the temperature dependence, however, the relative change is comparable.

4.1.5 Construction of samples to external electric field experiments

We plan to investigate [73] the influence of an external electric field on the self-organized formation of charged patches inside a macroscopic-size glass capillary. This would be important because this could lead to a possible enhancement of transmission or a better beam emittance at the exit of the capillary. We designed two different configurations, these two configurations referred as 1 and 2 can be seen in Figure 4.10.

Figure 4.10: Schematic plot of the two different electrode configurations. The black stripes show the single electrodes along the outer surface of the capillary.

The other key task of this measurement is to develop how to fit the dimensions regarding to the width of a single electrode. Considering the limitations on the capillaries length, the main goal was to minimize the uncovered areas in order to create stronger electric fields.

To check how strong the electric fields between the electrodes can get and to allow for inhomogeneous fields, a computer software called Poisson Superfish was

used. This software is a collection of programs for calculating static electric and magnetic fields amongst others. Our results of the calculations are illustrated in Figure 4.11 and 4.12).

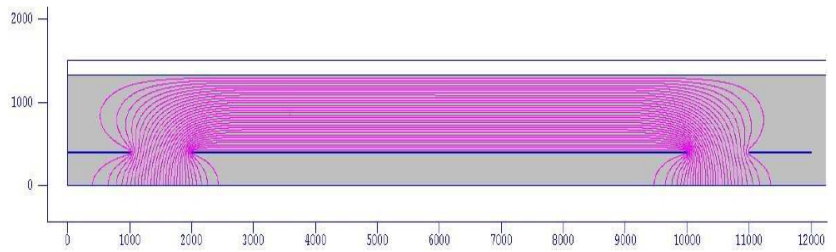

Figure 4.11: Model A: white frame on the top is an aluminium tube, the blue line shows the electrode cover and purple curves show the electric field.

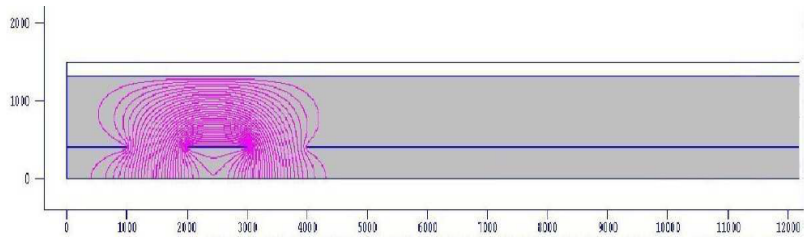

Figure 4.12: Model B: white frame on the top is an aluminium tube, the blue line shows the electrode cover and purple curves show the electric field.

One of the minimization factors was the breakdown voltage of the surroundings of the electrodes. The breakdown voltage for glass in ultrahigh vacuum is about 13 - 14 kV/mm and for the instant adhesive it is $\sim$ 44 kV/mm. During the construction of the sample holder it is possible that the whole gap between two electrodes will be filled with adhesive. For this reason, a single microcapillary was prepared, covered with the "1" configuration of electrodes (see Figure 4.10) and wired and was surrounded with the adhesive. In this way the breakdown

voltage of the adhesive could be tested. By the circumstances of the measurement the sample holder should bear a maximum voltage difference of 1.5 kV. The test was done with 2.5 kV. The difficulties of the preparation such a small, breakable, but very well defined sample holder also limited the minimization of the uncovered areas. By all these circumstances finally the uncovered areas on the surface of the capillary were 1 mm, like the width of the short electrodes. The two Poisson Superfish figures are adjusted to these exact dimensions, using the imaginary capillary length of 12 mm. To prepare the appropriate sample, as electrodes we used adhesive copper tape (the copper has very good electric conductivity). The copper foil was 100 μm thin, self adhesive on both of its sides and was wrapped around the capillary. The advantage of the copper foil is the easiness of the electrode wiring. The applied wires were 100 μm of diameter molybdenum wire (see Figure 4.13). Because of the parameters of the target holder installed in the UHV chamber, the electrode covered capillary should be inserted into an aluminium tube of an outer diameter of 3 mm.

The drillings of the three holes into the aluminium tube were required for two different reasons. The first was to have the chance to enable an outlet to connect the wires, attached to the electrodes of the capillary, to a voltage supply source. The second was to be able to provide constant adhesive, which glued the capillary into the interior of the aluminium tube. The three holes each had a diameter of 2 mm and those were centered at a distance of 3.5, 10.5 and 17.5 mm. The whole length of each aluminium tube was 20 mm. These hole configurations were suitable for both electric configurations.

Figure 4.13: Glass microcapillary covered with electrodes and wires.

The idea was to run a mounting wire through the interior of the capillary and clamp it tight later, while the the aluminium tube was aligned through being fixed immoveable in a milled edge. The completed construction device (see Figure 4.14) consists of two clamping parts and one middle component containing the precisely milled edge. The three main components are made of Polytetrafluoroethylene. The surface tension and the coefficient of friction of teflon are so low, that even the instant adhesive used in this project could not stick with it.

As mentioned before, the maximum voltage difference of about 1.5 kV between the neighboring electrodes should be accomplishable. To make the process of wiring as simple as possible our plan was to connect two outside electrodes directly to the conductive aluminium tube. In this way, the electrodes could be put to ground potential by just grounding the aluminium tube. Since the wire affixed to the middle-electrode, it needs to be connected directly to the voltage supply source, it is very important to electrically insulate the wire-section starting from where it emerges out of the drilled hole in the aluminium tube up to the point where it is connected to the source, outside the UHV chamber.

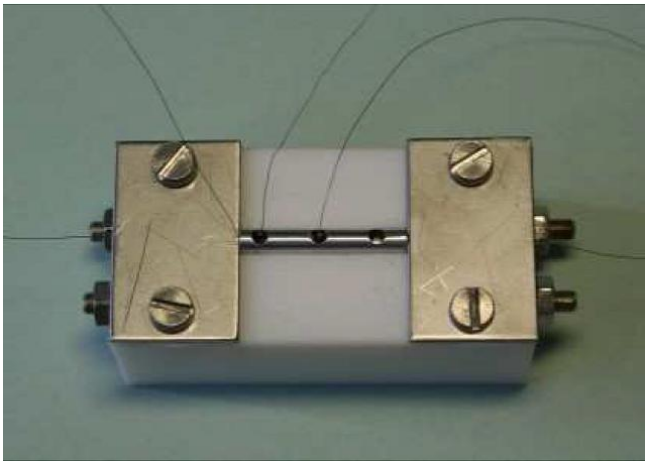

Figure 4.14: Device for placing and wiring the electrode covered glass capillary into the aluminium sample holder.

4.1.6 Summary

I have developed a process to produce the appropriate single glass capillary samples for our particle guiding investigations. In collaboration with the Atomic and Plasma Physics group at the Institute of Applied Physics, TU Wien, I have developed and built the first temperature controlled sample holder both for heating and cooling the capillary sample. To the investigation of the influence of an external electric field on the self-organized formation process of charge patches inside a microcapillary, we invented and constructed a set of miniature capillary samples with their special sample holders.

4.2 Transmission of slow highly charged ions through a single glass microcapillary

We investigated the transmission of 4.5 keV Ar^{9+} ions through a glass microcapillary [66, 68, 78]. The measurements were performed at Vienna University of Technology (TU Wien).

We studied the charging up mechanism inside the microscopic single glass capillary. Therefore we investigated the time dependent transmission probability of HCIs passing through the single glass tube.

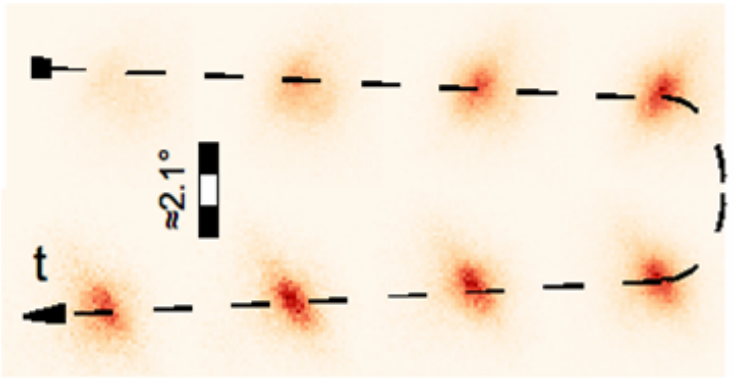

Figure 4.15: The movement of the beam spot on the PSD.

The spots in Figure 4.15 illustrate qualitatively the movement of the spot of the transmitted beam on the PSD as a function of time. The capillary was initially charged at a tilt angle of roughly ±5°. After the charging process the tilt angle was changed to approximately ±4°. Each segment of the picture shows the average of the 1 minute measurement. The last segment represents the stable condition since no significant change was observed afterwards.

Figure 4.16 shows the time-evolution of the transmitted intensity. We found that the experimentally observed values can be fitted with an exponential function $(1 - \exp^{(-t/\tau)})$. As a result of a two-parameter fit, one obtains a characteristic time of $\tau \approx 640$ s.

We did further systematic investigations of the time dependence for a set of other tilt angles (see Figure 4.17). We found that the experimentally observed

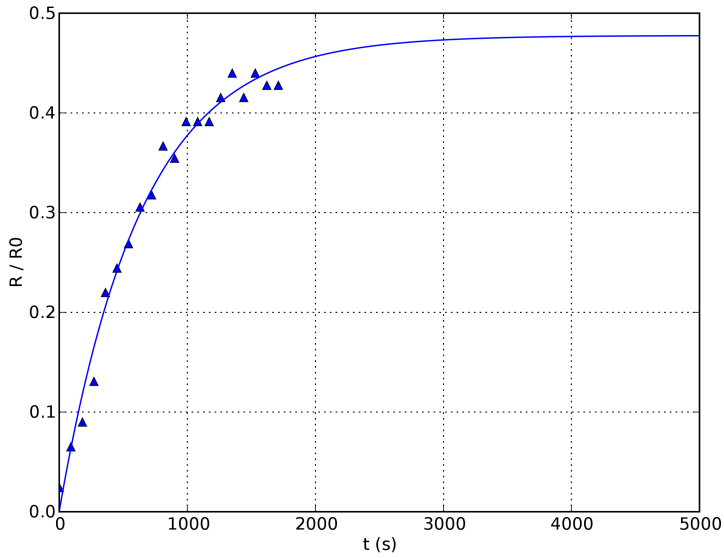

Figure 4.16: Time dependence of the normalized count rate of the transmitted Ar^{9+} ions, showing the charging process for a capillary tilt angle of 1.5°. Triangles: experiment. The normalized rate is fitted with the exponential function, $1 - \exp^{(-t/\tau)}$ (solid line), with a resulting time constant τ of approximately 640 s. The reference count rate, R_0, approximately 700 1/s, corresponds to the count rate of ions passing the straight capillary, which was measured prior to the charging process.

values can also be fitted with the exponential curve $(1 - \exp^{(-t/\tau)})$. For tilt angles smaller than the capillary acceptance angle we immediately observed stable transmission because of the geometrical transmission. When the tilt angle compared to the beam axis is larger than the acceptance angle of the capillary, the injected ions hit the inner wall of the tube at least once. In agreement with the expectation, with increasing tilt angle the characteristic time of the charging-up increases.

Figure 4.18 shows the time-evolution of the transmitted intensity, the deflection and the spot-size on the PSD. The data are shown qualitatively and

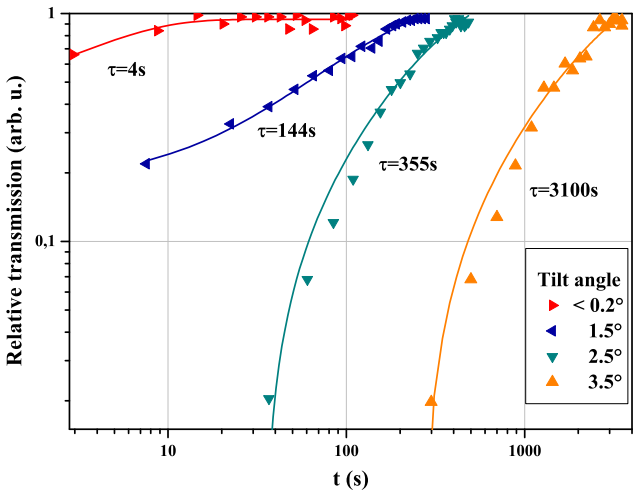

Figure 4.17: Time dependent relative transmission through the single glass capillary for various tilt angles. The values are normalized to 1 to the equilibrium state. The corresponding characteristic times of the charging up process are as follows: a) $\tau = 4$s, b) $\tau = 143$s, c) $\tau = 355$s, d) $\tau = 3100$s.

fitted by simple exponential laws to guide the eye. From the analysis of the data and also from Figures 4.15 and 4.18 it can be clearly seen that the spot moves on the surface of the micro-channel plate (MCP) detector slowly during the charging-up process. This means the observed projectiles cannot be vacuum ultraviolet (VUV) photons, which can also be produced in the chamber. If the transmitted particle were photons, the movement of the spots should be instantaneous to their final position on the PSD after tilting the capillary.

Interestingly, the time-constants of transmission and deflection seem to coincide, whereas the focusing of the beam, as shown by the size of the image on the PSD, changes faster.

As a next step, we investigated the guiding process of the single glass microcapillary after reaching stable conditions. We measured the dependence of

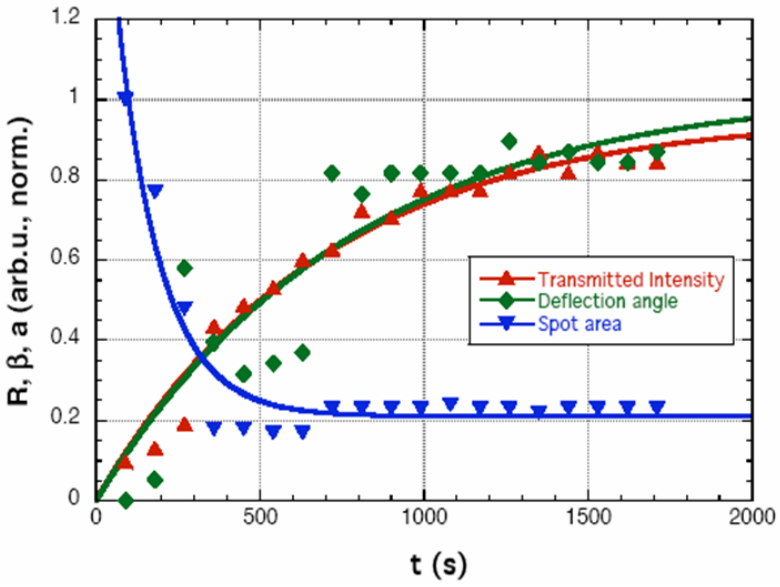

Figure 4.18: Time evolution of the transmitted intensity, the deflection angle and the spot size.

the position of the ion on the PSD and the tilt angle between the beam axis and the capillary respectively. Figure 4.19 shows the relation between the deflection angle, β of the projectiles and the tilt angle Ψ of the sample in one measurement process. The deflection angles of the transmitted projectiles were calculated from the beam positions at the detector, using the first momenta of the spatial charge distribution in the detector plane. The glass capillary was tilted up to 5° against the beam axis with a step size of 0.5 into one direction, and then in the same way to the other direction. The transmitted flux was of the order of 18000 counts/s. According to Figure 4.19, by increasing the tilt angle of the capillary with respect to the beam direction, the deflection angle of the transmitted beam increased in the same way, and into the same direction. This behavior, which has also been observed in the case of nanocapillaries, can be understood by means of charge patches forming on the inner wall until

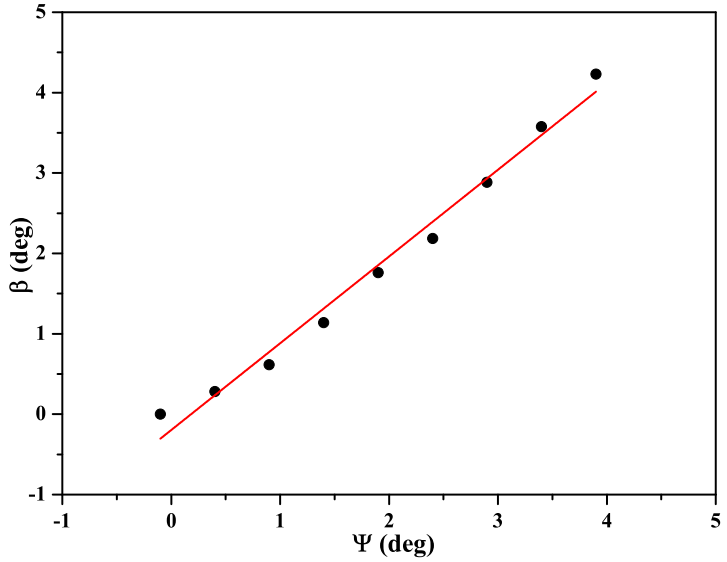

Figure 4.19: Defection angle β of the ion beam as a function of capillary tilt angle Ψ with respect to the beam direction. The solid line represents the $\beta = \Psi$ linear function.

the following ions are eventually deflected enough not to hit the wall, but pass through the whole capillary to reach the PSD. Interestingly, the guiding holds up to the microscopic dimensions of our glass tube. For obvious reasons, one expects the identity of the tilt angles with deflection angles, which is also found when fitting the data linearly, as also indicated in Figure 4.19. This proves that the beam was guided well through the capillary, for tilt angles as large as 4°.

Finally, we investigated the transmission of 4.5 keV Ar^{9+} ions through the capillary as a function of the tilting angle of the capillary, Ψ (Figure 4.20). We also measured the angular distributions of the transmitted ions. The presented

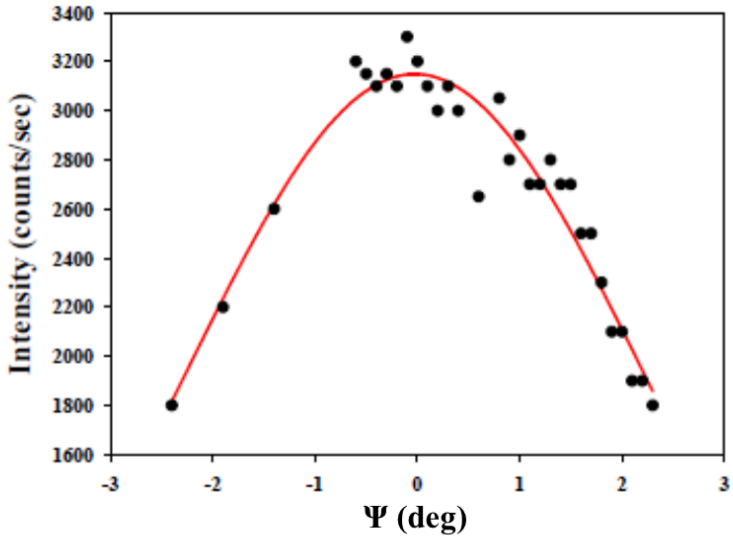

Figure 4.20: Transmission of 4.5 keV Ar^{9+} projectiles passing through a single glass macrocapillary depending on the tilt angle Ψ. The solid line is a Gaussian fit of the measured data.

data in Figure 4.20 shows the transmission of ions through the capillary as a function of tilt angle, covering a range of roughly $\pm 3°$.

Figure 4.21 shows examples of the transmitted angular distributions of the ions for various tilt angles. These angular distributions are calculated from the spatial ones at the PSD by a proportionality constant, which has been obtained by fitting the deflections of several measurements as function of the tilt angle and assuming agreement between these values. The distribution of the direct beam, passing a 0.5 mm aperture is shown, in order to get an impression of the initial distribution, which is not corrected for the finite diameter of the aperture. Therefore the Ψ axis cannot be taken as representative for the intensity profile (a) in Figure 4.21. For the case of transmitted ions the axis values are justified because of the small diameter of the capillary in comparison with the spatial latitude at the channel plate, which is of the order of mm. The angle in the

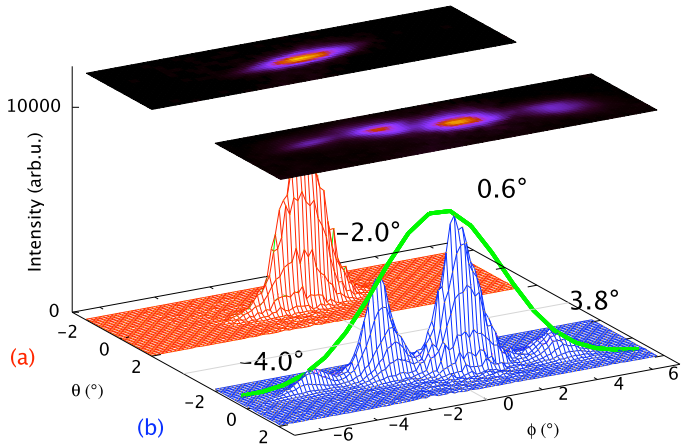

Figure 4.21: Angular distributions of the direct beam, collimated by a 0.5 mm aperture (a) in comparison with the guided distributions (b) for four different tilt angles as indicated. The z-axis shows the number of ion impacts per unit area. The green curve is a gaussian fit of the maxima of the distributions. Ψ is the lateral deflection angle in the horizontal plane, the elevation angle is Θ. The elliptical shape of the beam results from imaging aberrations in the mass-charge- separation plane.

vertical plane, Θ, is shown in a similar way. The spread in this plane is smaller than in the horizontal one, which is an experimental feature, resulting from imaging aberrations. From an analysis of the angular distributions, we estimate the initial angular distribution of the beam to a FWHM to be about 2.2° in the horizontal plane and 0.7° in elevation, Θ. After being transmitted through the capillary, the widths change to about 1.9° and 0.9° respectively, which is especially interesting because it suggests that there is focussing in the tilt plane, whereas the beam is slightly defocussed in the vertical plane. Eventually, the intensity profile is indicated by a Gaussian fit curve around the beam axis with a FWHM of approximately 3.3°.

Due to the fact, that the region between the capillary and the PSD is not field-free, but shows a strong potential gradient compared to the kinetic energy of the ion, we can state (i) that the charge state distribution of the transmitted ions is narrow with a mean value at least close to the incident beam, and (ii) that it is ions that are recorded on the PSD and not e.g. UV photons. The cause of the electric field lies in the fact, that the front layer of the detector is biased roughly -1.7 kV with respect to the ground potential. The trajectories of the ions are influenced when encountering the detector; this has been studied in simulations with SIMION [23] for the original trajectory to be reconstructed. It turned out that a linear relation between the deflection angle at the capillary and the detected position is still valid within the experimental boundaries.

4.2.1 Summary

We measured the transmission of 4.5 keV Ar^{9+} ions through a microscopic sized single cylindrical shaped glass capillary of a microscopic size and large aspect ratio.

I showed first that a guiding electric field for HCI can also build-up inside a straight micro-scale single capillary, thereby slow HCI can be transmitted through the microcapillary, keeping their initial charge state in a similar manner as for the case of nanocapillaries. Our results clearly indicate the existence of the guiding effect even in the case of large tilt angles.

We demonstrated that the self-organized formation of charged patches inside the capillary is a time dependent process, causing stable transmission after a charge up period.

We showed that the angular distributions of the transmitted ions have narrower widths than the incident beam, thus the straight capillary can be used as a beam focussing tool.

4.3 The effect of temperature on the guiding suffered by slow highly charged ions through microscopic glass capillaries

As a completely new aspect we investigated the temperature dependence of the ion-guiding [69] with our temperature dependent guiding apparatus [67]. One control parameter to optimize guiding is the residual electrical conductivity of the insulating material. Its strong, nearly exponential temperature dependence is the key to transmission control and can be used to suppress transmission instabilities arising from large flux fluctuations of the incident ions, which otherwise would lead to Coulomb blocking of the capillary. For a fixed tilt angle of the capillary axis with respect to the incident beam direction the intensity, position and angular distribution of the transmitted ions are recorded as a function of time. In Figure 4.22 we show the intensity of the transmitted ions as a function of capillary tilt angle as measured for different capillary temperatures. The experimental points are taken under steady-state conditions, i.e. after reaching a time-independent value of the transmitted intensity. Usually, the tilt angle steps between two subsequent measurements were kept smaller than 1°. Each curve is measured starting in almost straight direction, as determined by maximizing the transmitted intensity. The tilt angle was then increased stepwise until the capillary transmission became negligible. Afterwards, starting at this deflection, the capillary is tilted back stepwise and eventually into the other direction. For each tilt angle the total ion count rate onto the detector is summed up, a dead-time correction is applied and finally the transmission curves determined in this way are normalized with respect to the straight direction. Our data can be accurately fitted by Gaussians, yielding the so-called guiding power [59], i.e, a measure for the width of the transmission curve, as a result.

From Figure 4.22 it is obvious that the guiding works best for a capillary at room temperature (i.e, the lowest temperature shown in the figure), since the corresponding Gaussian has the greatest width. The capillary can be tilted by ± 5° before the intensity of the transmitted HCI drops by a factor of 10. Increasing the temperature leads to a considerable narrowing of the transmission function and a corresponding decrease of the guiding power. Eventually, above 60°C, one does not find further narrowing but a temperature-independent transmission function, which in fact exactly corresponds to the geometric transmission through the capillary (hatched region in Figure 4.22), showing a factor 10 drop in intensity within less than ± 0.8°. Due to that, at high temperature the conductivity is enhanced. Our own conductivity measurements for the ma-

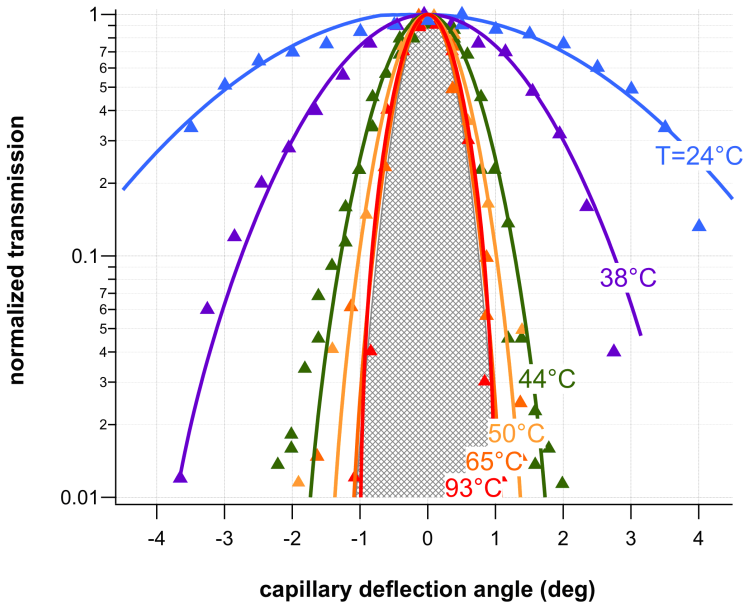

Figure 4.22: For different capillary temperatures the intensity of the transmitted ions through a single glass capillary is measured as a function of capillary tilt angle with respect to the beam axis. The flux of the incident 4.5 keV Ar^{9+} ions was kept constant ($\sim 5 \times 10^5$ ions $mm^{-2}\ s^{-1}$) which corresponds to about 5000 ions entering the capillary per second. Gaussian fits through the data points at the respective temperature are shown as solid lines. The hatched region corresponds to pure geometric transmission through the capillary without any guiding.

terial borosilicate show a two orders of magnitude increase in conductivity for a temperature increase of 50°C consistent with data from the literature [43] the charge patches seem to be more quickly removed than formed and guiding is no longer possible.

We have also studied the effect of the incoming ion flux on the guiding capability of our capillary. The corresponding data (all taken at room temperature)

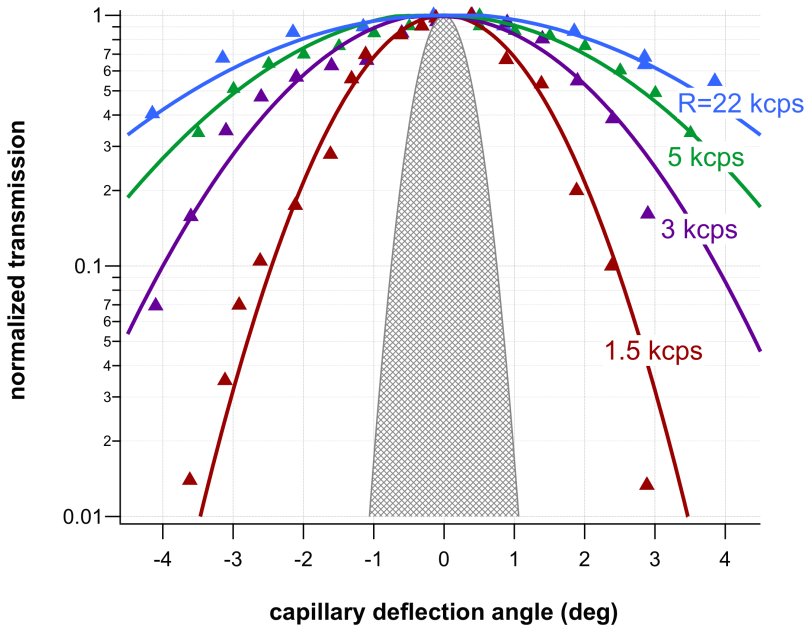

Figure 4.23: The intensity of the transmitted ions through a single glass capillary for different incident ion fluxes at room temperature (24°C) as a function of the capillary tilt angle. Gaussian fits through the data points (normalized to 1 in forward direction) are shown as solid lines. The curve label (in kilo-counts per second) corresponds to the number of 4.5 keV Ar^{9+} projectile ions entering the capillary per second (see text). The hatched region again indicates geometric transmission through the capillary without any guiding.

are shown in Figure 4.23. The curves are labeled using the average ion rate through the 100 μm reference aperture, which roughly equals the mean number of transmitted ions per second through the capillary in the straight direction. Again the region corresponding to pure geometric transmission is shaded. Qualitatively, the guiding power, i.e., the width of the curve, decreases for decreasing

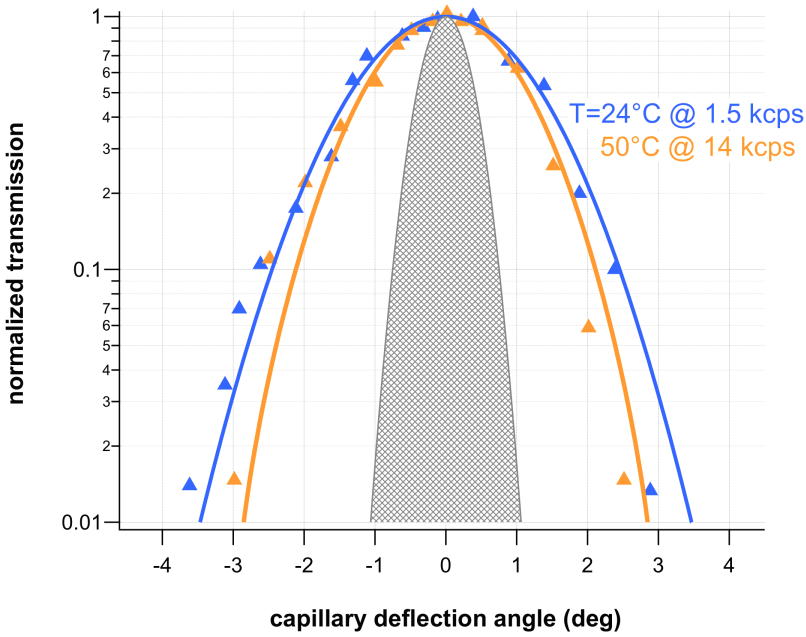

Figure 4.24: Comparison of two normalized transmission curves for 4.5 keV Ar^{9+} ions guided through a glass capillary. The two cases shown differ by a factor of 10 in the projectile flux on the one hand and an estimated factor close to 10 in the conductivity of the capillary (due to a temperature difference of 26°C) on the other hand. The given parameter values are the temperature of the capillary as well as the transmitted ion count rate measured through the reference aperture.

incident ion flux, approaching geometric transmission in the limit of zero ion impact per second.

Since self-organized guiding needs a dynamical equilibrium between charge-up by a series of ion impacts at the internal walls and the charge removal by diffusion/conductivity along the surface or into the bulk [17, 18], one should be able to counterbalance the effect of increased charge removal due to higher conductivity/temperature by increasing the incident ion flux or vice versa. There-

fore, in Figure 4.24 we compared two cases, in which the ion fluxes differ by about a factor of 10, but at the same time the temperature is changed by 26°C, which also roughly corresponds to a factor of 10 in the conductivity of the glass (see above). Indeed, the Gaussian fits through the data points of the curves nearly coincide, indicating that only the ratio between the charge deposition rate and the charge removal rate is relevant for guiding.

All data presented so far have been measured at room or higher temperatures. By actively cooling the capillary (and thereby decreasing its conductivity further) to temperatures well below the freezing point of water we soon encountered a regime where no steady-state transmission behavior could be established. Depending on the capillary tilt angle the time dependent transmission rapidly varied between maximum and zero transmission [37, 24]. In addition, the beam spot on the position sensitive detector (resulting from the impact of transmitted ions) started to move randomly as shown in Figure 4.25 for a capillary cooled to −25°C.

The movement of the center position of the beam spot of transmitted ions was recorded for a capillary tilted by 3° and cooled to −25°C. During the four hour long measuring period (the time information is coded into the curve as grey scale) the random movement of the beam spot covers an angular range of almost 5°. Since this is much larger than the geometric opening angle of the capillary, the respective charge-patch responsible for the strong deflection has to be located close to the exit of the capillary, but seems to change its position rather arbitrarily. This behavior is in strong contrast to that of a hot capillary (40°C), where the beam spot position is stable over hours only showing small spatial fluctuations (see upper curves in Figure 4.25) associated with the time development of charge patches inside the capillary.

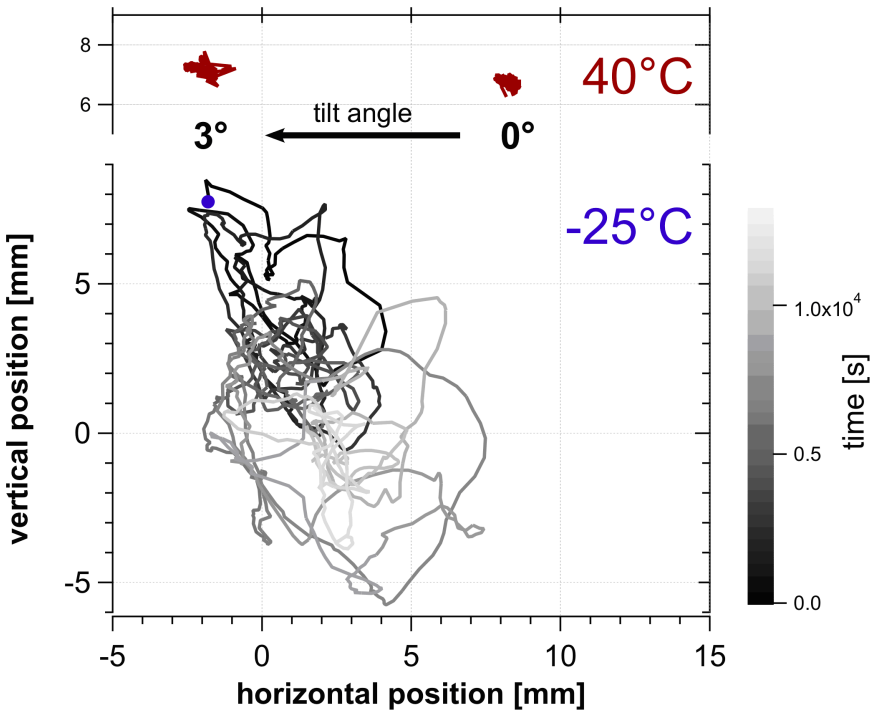

Figure 4.25: Position of the beam spot on the detector after passage through the capillary, once for the case of a cold capillary T = -25°C tilted by 3° with respect to the incoming beam axis (lower curve), in comparison with the case of a hot capillary T = 40°C tilted by 0° and 3°, respectively, (upper curves). The beam position has been evaluated by a 2D Gaussian fit of the time-binned spatial distribution on the detector. 4.5 keV Ar^{7+} ions have been used as projectiles.

4.3.1 Summary

We measured the temperature dependence of ion-guiding for the first time. A control parameter to optimize guiding is the residual electrical conductivity of the insulating material. Its strong, nearly exponential temperature dependence

is the key to transmission control and can be used to suppress transmission instabilities arising from large flux fluctuations of incident ions, which otherwise would lead to Coulomb blocking of the capillary.

We demonstrated the strong dependence of transmission of Ar^{9+} ions through a single microscopic glass capillary on temperature and on the ion flux. We showed that, by varying the glass temperature, we are able to manipulate the electrical conductivity of the borosilicate glass by several orders of magnitude. Thereby the effect of conductivity on the build-up and removal of charge patches in the capillary can be studied.

We showed that the temperature of the glass capillary has a large influence on the transmission of ions and it can be compensated for by adjusting the incident ion flux. The conditions of the guiding can be adjusted from guiding at room temperature to no guiding, i.e. simple geometrical transmission at high temperatures.

4.4 Energy dependence of electron transmission through a single glass microcapillary

Transmission of electrons of energy 300-1000 eV was studied in order to gain more insight into the electron transmission process through a single straight glass capillary of microscopic scale. The measurements were conducted in the tandem Van de Graaff accelerator laboratory at Western Michigan University.

Two glass capillaries with slightly different geometries were used to investigate the energy dependence of electron transmission. The capillaries, hereafter referred as sample A have the following parameters: diameter $d = 0.18$ mm, length $l = 14.4$ mm, aspect ratio $l/d = 88$, and sample B: diameter $d = 0.23$ mm, length $l = 16.8$ mm, aspect ratio $l/d = 73$.

During the first phase of the experiment, the transmission of 300, 500, 800, and 1000 eV electrons through sample A and 300 and 500 eV through sample B was investigated (the values of the energies are nominal, the exact energy values are always shown in the figures). The transmitted intensities were normalized with respect to the incident beam. Angular dependence data were taken after transmission reached the steady state at every tilt angle Ψ. This took about 2 hours after first putting the beam on the sample. The spectrometer angle Θ was varied in small steps to collect transmitted spectra, keeping Ψ constant. The process was repeated for different tilt angles at each energy. The background pressure in the scattering chamber was $\sim 10^{-6}$ torr. Significant intensities of the electrons transmitted through the capillary were observed up to $\Psi \sim 6^{\circ}$ for 500, 800 and 1000 eV, whereas, intensities were observed only up to 3° for 300 eV for both samples.

Some of the measured electron energy spectra obtained at 500 and 1000 eV at tilt angles $\Psi = 0^{\circ}$, 0.5°, 1.0°, 1.5°, 2.0° and 3.0° for $\Psi \approx \Theta$, where maximum transmitted intensity was observed, are shown in Figure 4.26. These are the nominal energies, the values of which were set on the high-voltage power supply. It can be seen that the overall transmitted intensity decreases strongly as the tilt angle increases. Notably, the spectra show evidence for increasing energy losses when the sample is tilted to larger angles suggesting that a fraction of the electrons undergo inelastic scattering with the inner surface while traversing the sample. This is most prominent when the tilt angle exceeds 2.0° - 2.5°, where the direct beam dominance is lost.

The spectra in Figure 4.26 also indicate the existence of two different regions of transmission due to the dominance of inelastically transmitted electrons at higher tilt angles compared to elastically transmitted electrons at lower angles.

Some previous studies of electron guiding in PET nanocapillaries for 500-1000 eV electrons also showed that the transmitted electrons lose energy when they traverse through the capillaries [14, 53].

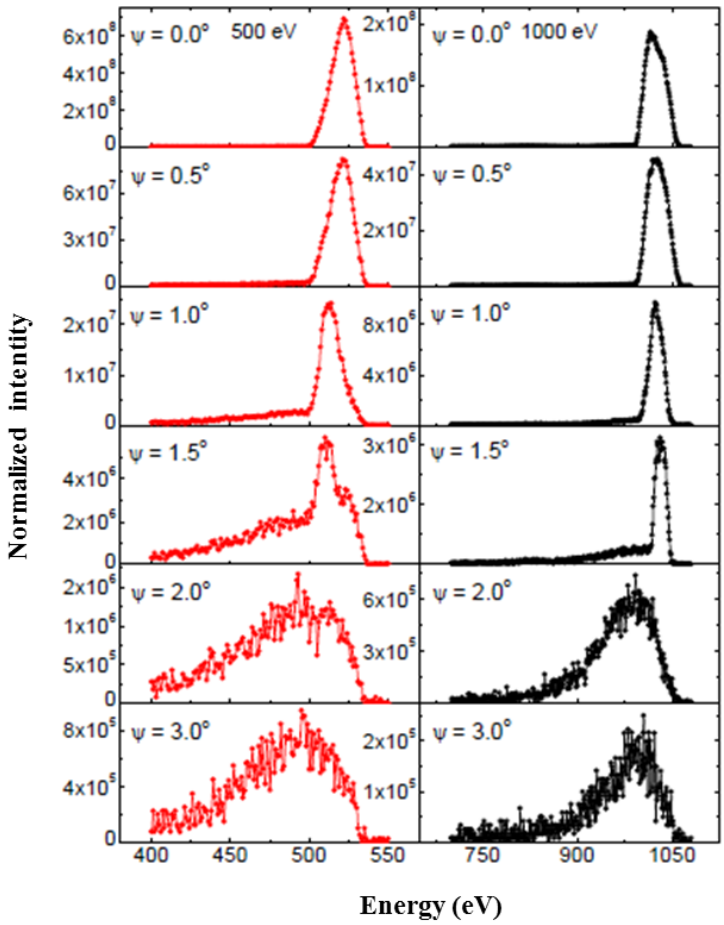

Figure 4.26: Energy spectra of transmitted electrons for 500 and 1000 eV. All the spectra were taken for $\Psi \approx \Theta$, where maximum transmitted intensity was observed.

In contrast, a study of Al_2O_3 nanocapillaries for slightly lower energy electrons (200-350 eV) has reported no observation of appreciable energy loss [15]

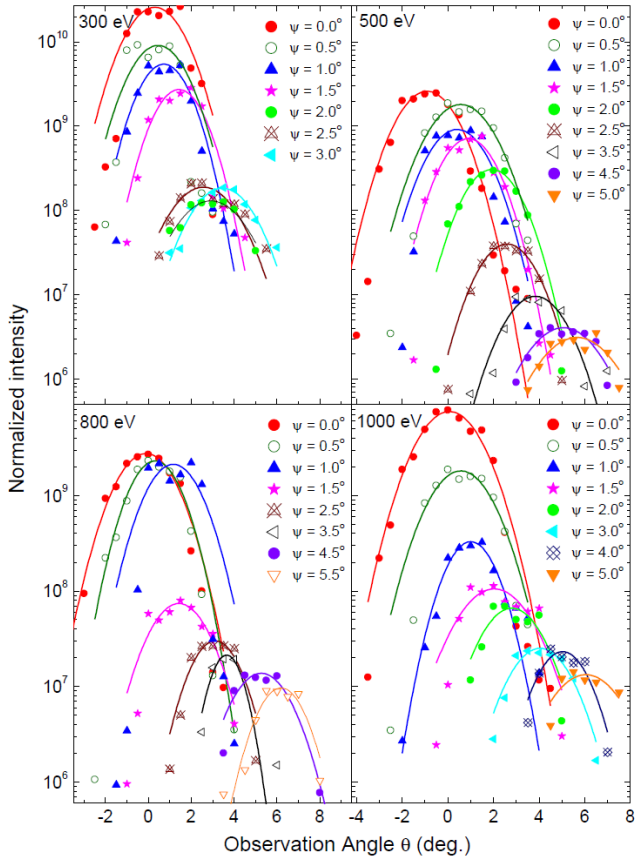

Figure 4.27: Angular distributions of the normalized integrated intensities as a function of observation angle Θ for various tilt angles Ψ for 300, 500, 800 and 1000 eV for sample A. The solid lines represent symmetrical Gaussian fits to the data.

like for the slow HCI transmission through nanocapillary foils [7, 25, 39, 50, 55, 56]. Figure 4.27 shows the angular distributions of the transmitted electrons for 300, 500, 800, and 1000 eV for sample A. Sample B produced almost similar distributions. The angular distributions of transmitted electron intensities were obtained by integrating over the entire regions of the spectra. All the intensities are normalized with respect to the current measured on the sample. The acquired integrated intensities are plotted as functions of the spectrometer angle Θ for different sample tilt angles Ψ, for all the energies. It can be seen from the Figure 4.27 that electron transmission depends strongly on the sample tilt angle Ψ and the incident electron energy.

The transmitted electron intensities show a decrease with the tilt angle Ψ agreeing with observations for slow ions [7, 25, 55, 66, 68] and previous electron studies [14, 15, 53]. It is evident from Figures 4.26 and 4.27 that the intensities are found to display two distinct regions of decline at lower tilt angles and slower drop at the higher tilt angles.

In addition to the transmitted intensities, the centroid observation angles (spectrometer angle at which the highest integrated transmitted intensity is observed) and the respective tilt angles of Figure 4.27 are plotted for 300, 500, 800 and 1000 eV for sample A in Figure 4.28. We note that the sample B revealed almost similar results. The results show a linear relationship for all the energies giving evidence that electron transmission through glass microcapillaries is in agreement with what has been observed for slow HCI guiding [7, 66] and electron transmission through nanoscale capillaries [14, 53].

Unlike slow HCIs, the energy spectra of electrons transmitted through the single glass capillary exhibit significant energy losses as seen in Figure 4.26. In order to understand this energy loss, the centroid energies (weighted mean values of the spectra of the transmitted electrons) and full-width-half-maximum (FWHM) values of collected energy spectra were analysed. The centroid energies were defined by

$$E_c = \Sigma \frac{E_i I_i}{I_i}, \tag{4.3}$$

where E and I are the energy and corresponding intensity at a given point of the spectra, respectively. In order to get the FWHMs of the spectra, they were fitted with Gaussian functions. The FWHM values, Υ-s can be written as

$$\Upsilon = 2\sqrt{2\log 2}\sigma, \tag{4.4}$$

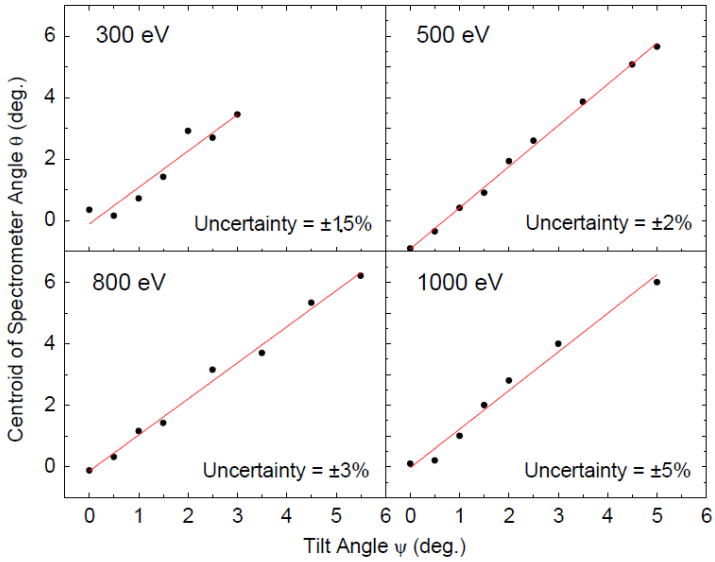

Figure 4.28: Variation of centroid spectrometer angle Θ with sample tilt angle Ψ for 300, 500, 800 and 1000 eV for sample A. Uncertainties of the linear fittings are shown in the bottom right corners for each energy.

where σ is the standard deviation of the Gaussian distribution. The parameters were calculated using the software Origin 8.0. In order to study the variation of the energy loss at capillary tilt angle Ψ, the centroid energy values for all the spectra ($\Theta = \Psi$) were calculated and plotted against the different tilt angles for 300, 500, 800 and 1000 eV electrons.

As shown in Figure 4.29, the general trend of centroid energies for all incident electron energies shows a decrease with increasing sample tilt angle. In Figure 4.29 the data were fitted with a first order exponential curve, $K + J\exp(\Psi/\alpha)$, where α is the decay constant and J and K are constants expressing the angular behavior of the energy loss. The centroid energy values below $\Psi \approx 2^{\circ}$ are nearly constant for all energies. For $\Psi > 2^{\circ}$ a fast decline starts, followed by a much slower fall-off at higher tilt angles for most energies (500, 800 and 1000 eV).

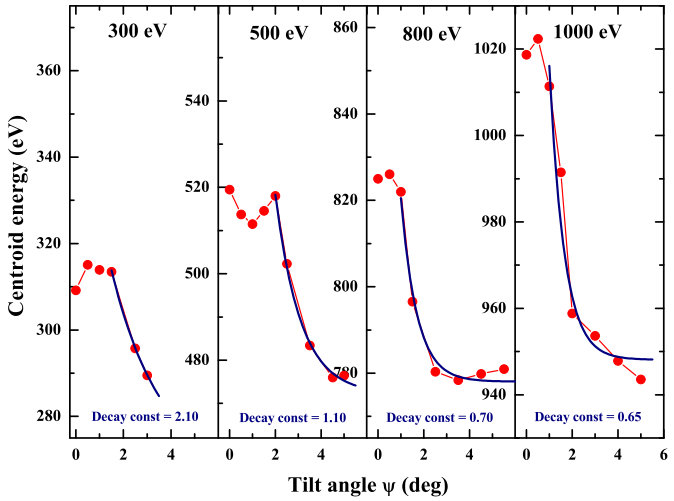

Figure 4.29: Centroid energy vs. sample tilt angle Ψ at 300, 500, 800, and 1000 eV for sample A. Blue lines show first order exponential decay fittings. Respective decay constants (DC) are shown at the bottom of each graph.

Since an electron beam of divergence $\sim 2.2^{\circ}$ was used for the measurements, $\Psi < 2.2^{\circ}$ represents the direct transmission region.

The constant of the angular decline for 300 eV was found to be as high as 2.1° whereas for 1000 eV it was less than half this value, showing a noticeable decrease with increasing energy.

The FWHM values for all the $\Psi \approx \Theta$ spectra are also plotted as functions of the tilt angle at 500, 800 and 1000 eV for sample A and at 300 eV for sample B as shown in Figure 4.30. The variation of FWHM values with increasing tilt angle was found to be out of phase with that of the centroid energy values shown in Figure 4.29. As expected, an abrupt increase in the FWHM value was observed near the boundary between the direct and indirect regions for all incident beam energies. Since an increase in FWHM is attributed to a broadening of the transmitted energy spectra, the sharp increase of FWHM in

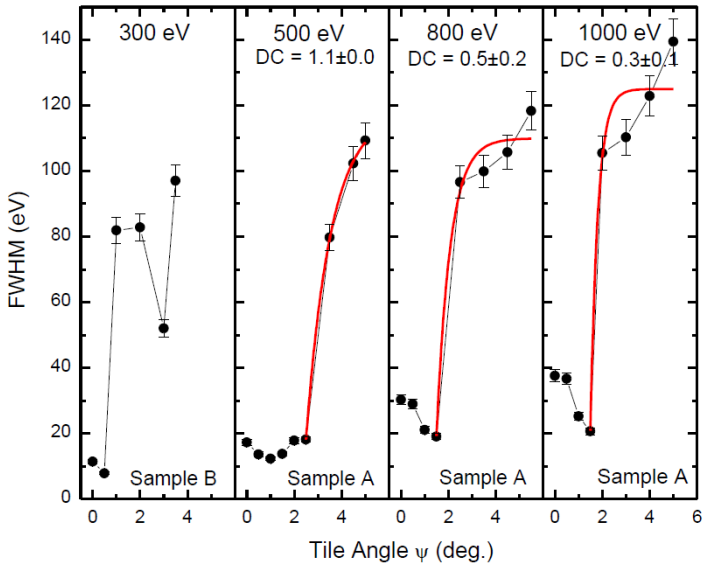

Figure 4.30: FWHM vs. sample tilt angle Ψ for 300, 500, 800, and 1000 eV electrons. Here the 300 eV curve is for sample B whereas the others are for sample A. The respective decay constants (DC) are shown at the bottom of each graph.

the boundary region suggests an increased energy loss with increasing sample tilt angle, agreeing with the previous result on the centroid energies. Furthermore, different transmission characteristics are visible in the two regions, with sharp increases in FWHM in the indirect region compared to the direct region, a result that can be attributed to continuous energy loss with increasing tilt angle in the indirect region. To analyze the elastic and inelastic characteristics of the spectra further, the variation of the intensities of the electrons scattered inelastically with respect to those scattered elastically with sample tilt angle Ψ was analysed for $\Psi \approx \Theta$ spectra for all energies for both samples. The intensity of the inelastically transmitted electrons was obtained by integrating the inelastic parts of the spectra, energies of 200-300, 400-500, 700-800 and 700-990 for 300, 500, 800 and 1000 eV, respectively, whereas energies of 300-330, 500-550, 800-

860 and 990-1080 for 300, 500, 800 and 1000 eV, respectively, were considered as the elastically transmitted range. The obtained results for $I_{\text{inelastic}}$ / I_{elastic} are illustrated in Figure 4.31.

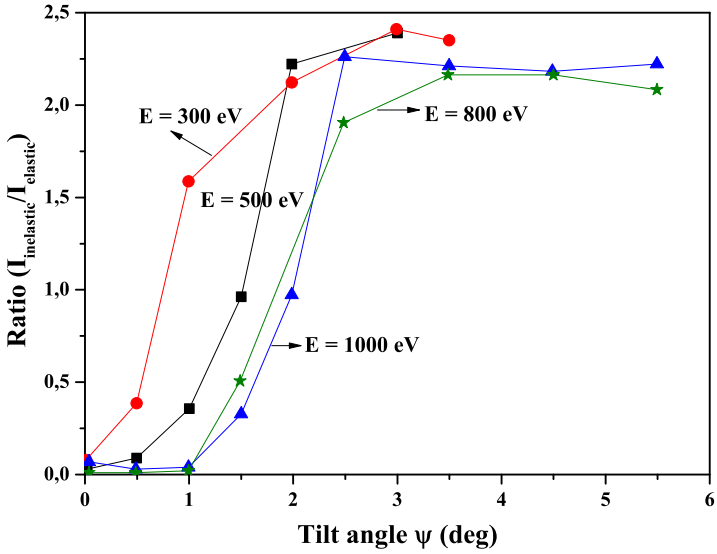

Figure 4.31: Variation of inelastic to elastic ratios of transmitted electrons with capillary tilt angle for sample A and B at different electron energies. Black and green stars show the ratios for sample B at 300 and 500 eV. The green and red dots are the results for sample A at 800 and 1000 eV.

According to Figure 4.31 all ratios follow the same trend, an increase in inelasticity with increasing tilt angle. For tilt angles beyond 2.5° (indirect region) the inelastic transmission reaches a constant value of about 2:1 to the elastic contribution for all incident energies. This result also demonstrates the difference in transmission characteristics in the direct and indirect regions. The indirect region showing more inelastic characteristics compared to the direct region. In Figure 4.31, lower energies show a higher inelastic contribution for

smaller tilt angles, suggesting the small percentage of the beam can still make a considerable contribution to the total transmitted fraction even after losing some of its initial energy.

Coulombic repulsion has been established as the driving force behind HCI guiding through capillaries for which beam interactions with the capillary surface are inhibited due to charge accumulation, giving rise to elastic transmission of charged particles. We believe such guiding effects exist in electron transmission as well [15, 14], but it is less effective compared to HCIs due to the inability of electrons to make strong charge patches. Since only a small amount of charge needs to be deposited close to the capillary entrance at smaller tilt angles to deflect succeeding electrons, together with contributions of the direct beam, transmission at lower Ψ in Figure 4.29 is more elastic (higher centroid energy values). When the tilt angle is increased, the direct beam contribution decreases and more charge is needed to elastically deflect the incoming electrons to a larger angle. Hence, Coulomb repulsion diminishes, giving way to more inelastic (lower centroid energy) and slowly decaying scattering processes. When an electron beam with higher primary energy (higher penetration depth) interacts with an insulator surface, electrons will have longer escape depths to reach the surface. This explains why the first order exponential fittings to the decay curves in Figure 4.29 show decreasing (faster) decay constants for higher energies.

The variation of centroid energies as a function of Θ for different sample tilt angles Ψ at 500 eV for sample A is shown in Figure 4.32 (only $\Psi = 0.0°$, $1.0°$, $2.5°$, $3.5°$, $4.5°$ and $5.0°$ are plotted for better visualization). At $\Psi = 0.0°$ the centroid energy is almost equal to the bare beam energy value (energy of the beam without the sample, shown by the horizontal solid line at 519 eV). The results in Figure 4.32 show that the majority of the transmission through the capillary at $\Psi = 0.0°$ is due to the direct beam with no interaction with the inner wall, as the centroid energies near the centroid angular value ($\Theta \approx \Psi$) are almost equal to the bare beam energy (519 eV).

The average centroid energy values reside on a plateau for almost all tilt angles and decrease only at the edges of the distribution. It is believed that the defocusing (broadening) of the guided ions, giving rise to higher angular FWHM values, is a result of the electric field produced by the ions deposited at the exit of capillaries.

Due to this potential, emitting charged particles can gain a perpendicular energy $E = qU$. The emission angle of the charged particles (α) can be obtained from

$$\tan\alpha = V_{\perp}/V_{\parallel} = (qU/E_p)^{1/2}, \tag{4.5}$$

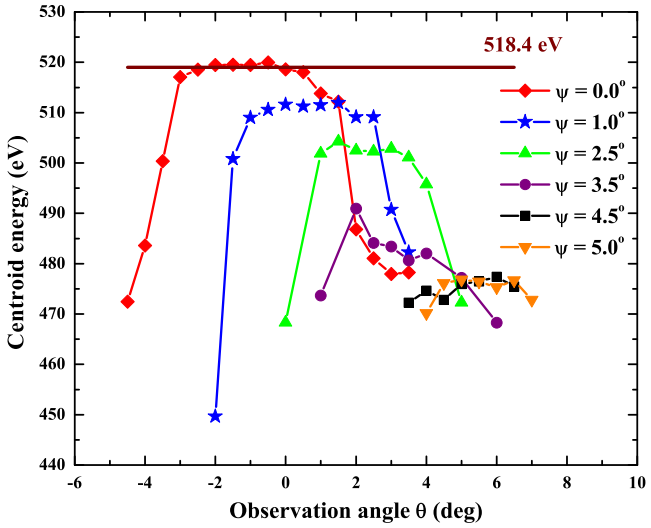

Figure 4.32: Centroid energy vs. observation angle Θ for sample A at 500 eV. Solid straight line at 518 eV indicates the bare beam (without the sample) energy value. Only some tilt angles measured are shown for simplicity.

where $V_\perp$ and $V_\parallel$ are the velocities perpendicular and parallel to the capillary axis, while q and E_p are the projectile charge and energy respectively [50]. It is obvious that the exit potential, U, of the capillary has a direct impact on the emission angle of the charged particles. Since U depends on the charge deposition on the capillary, material properties, such as electrical resistivity, play a key role in determining the emission angle for a given material and in turn, FWHMs. In recently published results for 3 keV Ne^{7+} transmission through PET nanocapillaries (aspect ratio 50), FWHMs of 3° and 2.8° at $\Psi = 0°$ have been reported in two different cases [50, 54], whereas for 4.5 keV Ar^{9+} transmission through a microscopic glass capillary of aspect ratio 68 an FWHM of 2.2° has been seen at a similar tilt angle. This lower transmission width is attributed

to the inability of the material to hold the charges with decreasing resistivity. Furthermore, in Stolterfoht *et al.* [50] increasing angular FWHM upon charge deposition has also been reported, which also indicates that increasing exit potentials yield broader transmission profiles. Defocusing effects have also been observed in most of the electron transmission experiments conducted using both nanocapillary foils [14, 53], as well as straight glass capillaries [70], suggesting the existence of a charge distribution at the exit. But compared to broader transmission profiles for HCIs observed in similar energy and aspect ratio cases (4.5 keV Ar^{9+} through a microscopic glass capillary of aspect ratio 68), electron transmission profiles obtained in this experiment (500 eV electrons through a glass capillary of aspect ratio 73) show almost twice lower FWHM value (1.1°) at $\Psi = 0°$. This suggests that the electron distribution at the capillary exit is weaker than that of ions under similar conditions. The observation of lower centroid energies at the outer edges of the transmitted broadened beam in the present work (Figure 4.32) would then be a result of the weakness of the exit charge distribution leading to interactions of the transmitted electrons with the capillary inner surface at the point of exit. Additionally, since the intensity of the electron beam seen at the capillary exit is much smaller than that at the entrance, charge up time for the exit can be longer and perhaps never reaches its equilibrium during the course of the measurement. It is emphasized that in the behavior seen in Figure 4.29, the beam interactions with the inner capillary exit have been minimized (or excluded) by considering electron transmission along the centroid angular position (i.e., along the axis of the capillary) for $\Theta = \Psi$. So, energy losses seen in Figure 4.29 must be caused by the weakness of the entrance charge patch to deflect incoming electrons to larger angles, and are not caused by the exit charge patch. It is evident that the incident electron beam is subjected to energy loss due to its interaction with the capillary inner wall, resulting in two regions, direct and indirect, having pronounced differences in transmission characteristics. This result points to the fact that electron transmission is a fundamentally different process than HCI transmission, as no energy loss or inelastic contributions to the transmission have been reported for HCIs so far. These differences and the energy loss mechanism will be discussed in detail later in the chapter.

Studies on slow HCI guiding through various kinds of nanocapillary foils have revealed that the fraction of transmitted ions depends on the primary energy E_p of the incident beam as well as the tilt angle Ψ in an exponential manner. According to previous works, the fraction of ions transmitted is given by

$$f(\Psi) = f(0)\mathrm{e}^{-\frac{Ep}{qU_s}\sin^2\Psi} \tag{4.6}$$

where $f(0)$ is the fraction transmitted at $\Psi = 0°$, q is the initial charge state of the incident ions, and U_s is the average potential across the capillary diameter due to charge deposition at the entrance [50, 59]. So, for small tilt angles the transmitted fraction can said to fall off as a function of exp(-Ψ^2).

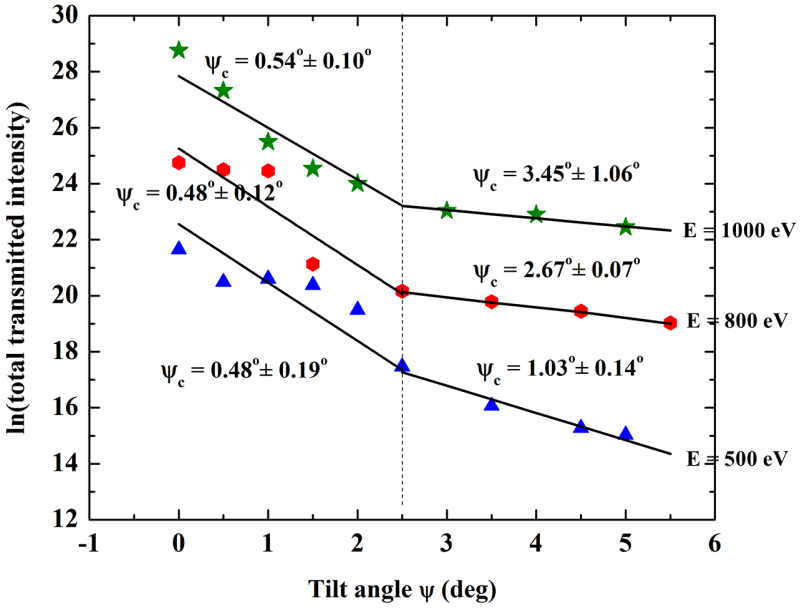

Figure 4.33: Natural logarithmic plots of the maximum peak heights of the Gaussian fits to the angular distributions for sample A from Figure 4.27. Intensities for 800 and 1000 eV have been shifted by -2 and -4, respectively, along the vertical axis for ease of visualization. Values of $\Psi < 2.5°$ represent the direct transmission region of electrons, and values of $\Psi > 2.5°$ the indirect transmission region. Values of Ψc are the characteristic guiding angles.

To understand the electron transmission characteristics further, the natural logarithm of the maximum peak height of the Gaussian fit to the angular distribution for each capillary tilt angle at each energy from Figure 4.27 was plotted against the respective tilt angle as shown in Figure 4.33. The linear dependence in both regions indicates that the transmitted electron intensity falls off as a function of $e^{-\Psi}$, as already observed for electrons through a PET foil [14, 53], and disagrees with slow HCI guiding [50, 59], where the dependence has a quadratic exponent, see Eq. 4.7.

The transmitted intensities were found to reveal two distinct regions, as expected, which have very different characteristics. For tilt angles $\Psi < 2.5°$ (direct region) the transmission falls off with a steeper slope than in the second region for $\Psi > 2.5°$ (indirect region). The characteristic guiding angle Ψ_c, defined as the tilt angle for which the transmitted intensity falls to 1/e of its value at $\Psi = 0°$, is a measurement of the ability of the material to guide the charged particles along the capillary [59]. For the case of slow HCIs, it can be determined from

$$I_\Psi = I_0 \exp\left(-\frac{\sin^2\Psi}{\sin^2\Psi_c}\right), \tag{4.7}$$

where I_Ψ and I_0 are the transmitted intensities at a given tilt angle and at $\Theta = 0°$ respectively. As for the case of HCI transmission, since the intensity falls off as exp(-Ψ) [54] the characteristic guiding angle for electron transmission can be found from the slope of the $\ln(I_\Psi)$ vs Ψ curve with transmitted fraction given by:

$$I_\Psi = I_0 \exp\left(-\frac{\Psi}{\Psi_c}\right), \tag{4.8}$$

The acquired results for the guiding angles are also given in Figure 4.33. In the region of direct transmission (Figure 4.33), where $\Psi < 2.5°$, the characteristic guiding angle was found to be the same for all the energies within the experimental uncertainties, and has a smaller value than in the indirect region, where $\Psi > 2.5°$. In the indirect region, Ψ_c increases (slower fall-off) with increasing energy with the likely exception of energies below 500 eV. This indicates a clear difference between slow positive ion transmission characteristics [59] and previous results for fast electron emission [14], which showed a decrease in the guiding ability with increasing energy for all incident energies. The large scatter of the data points in the direct region is likely due to incomplete charge-up of the inner walls. Increase in the tilt angle corresponds to an increase in the surface

charge density as the beam is deposited in a smaller area [58]. Therefore, the charging process at smaller tilt angles is slower than for larger tilt angles. The values for Ψ_c for ion and electron transmission through PET nanocapillaries have shown different characteristics from each other. It has been observed that the Ψ_c values for ions are greater than those for both the elastic and inelastic regions of electrons. This suggests that the guiding ability of PET is smaller for electrons than for ions and it is even smaller for the case of low energy electrons through glass capillaries. Both for ions and electrons transmitted through PET Ψ_c decreases with increasing energy, whereas it increases for the case of glass capillaries, suggesting an increase in electron guiding ability with energy, while it decreases for the other two cases. If the inner surface of the capillary is insufficiently charged so that the field produced at the entrance is not strong enough to deflect the incoming beam, the electrons will interact with the sample surface and/or the bulk and scatter as a result.

In order to investigate if the scattering effects which take place in the indirect region of transmission obey the single collision Rutherford predictions, the experimental data were compared with theoretical predictions. For this, the yield at a given tilt angle and energy can be written in terms of the Rutherford cross section, which is given by

$$\frac{\mathrm{d}Y}{\mathrm{d}\Omega} = C_n \frac{Z_1 Z_2}{E_p^2 \sin^4\left(\frac{\Psi+\alpha}{2}\right)}, \tag{4.9}$$

where, C_n is a constant obtained by normalizing the cross section to unity, Z_1 the charge of an electron and Z_2 the charge of the nucleus of the atom which it scatters from, E_p the incident electron energy, Ψ the sample tilt angle, and α a small offset angle introduced to remove the singularity of the cross section at $\Psi = 0°$. The ratio Y(Ψ)/Y(Ψ=0) was calculated for the obtained data for tilt angles $\Psi > 2.5°$ for all the energies, where Y(Ψ) and Y(Ψ=0) are the total electron yields at angles Ψ and $\Psi = 0°$, respectively. Experimental data were compared with the curve

$$\frac{Y(\Psi)}{Y(0)} = \frac{\sin^4\left(\frac{\alpha}{2}\right)}{\sin^4\left(\frac{\Psi+\alpha}{2}\right)}, \tag{4.10}$$

and the results are plotted in Figure 4.34. Good agreement between the calculation and experimental data was found for 300 and 500 eV, but for the higher energies, 800 and 1000 eV, there is an evident deviation from the Rutherford calculations.

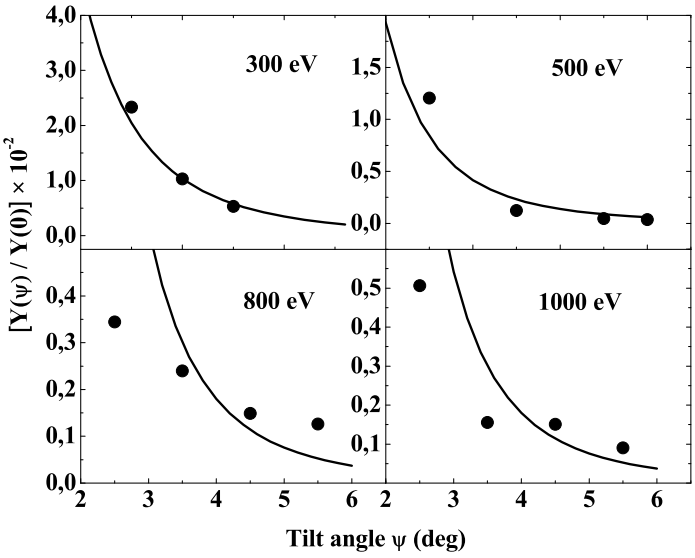

Figure 4.34: Y(Ψ)/Y(0) of the obtained data vs. tilt angle for all energies, where Y(α) is the yield at tilt angle Ψ and Y(0) is the yield at angle $\Psi = 0°$. Dots indicate the experimental data points and the solid lines are the theoretical predictions of the Rutherford scattering cross section. The 300 eV data are from sample B and the other data from sample A. Results for 500 eV have been multiplied by 2 for better visualization.

This suggests the dominance of single-collision Rutherford scattering at lower incident energies and the emergence of a different process at higher energies. According to Rutherford predictions, the yields, as well as the characteristic guiding angles, should decrease with increasing energy. In agreement with the predictions, the yield for 500 eV in the region $\Psi > 2.5°$ (where Rutherford scattering is important) is less than at 300 eV. Also, the total electron yields due to secondary electron emission are a maximum at a primary electron energy of $\sim$ 400-450 eV [57]. So, scattering effects at 800 and 1000 eV should result in smaller yields than at lower energies. As the primary electron energy increases,

the penetration depth of the electrons increases, which would give smaller characteristic guiding angles (faster fall-off) for $\Psi > 2.5°$. However, contrary to the Rutherford predictions the results show an increase in the yield and the guiding angles (slower fall-off) for $\Psi > 2.5°$ above 500 eV. Therefore, a second process may be taking over for the transmission at higher energies. This second process is attributed to charge deposition resulting in Coulombic repulsion.

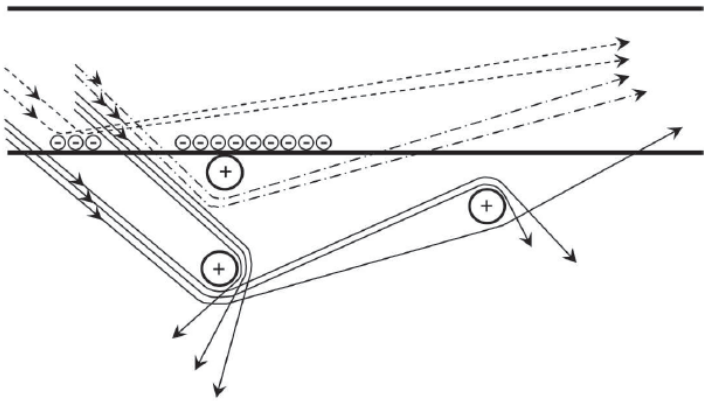

Figure 4.35: Collision geometry of the scattering of lower and higher energy electrons. Coulombic scattering of electrons from surface charge buildup is shown by the dashed lines. Lower energy electrons (dot-dashed lines) scatter (quasi-) elastically from atoms close to the capillary surface and can be transmitted towards the exit. Higher energy electrons (solid lines) penetrate deeper into the bulk of the capillary and lose energy due to various inelastic processes, causing loss of the electron within the sample or transmission through the capillary if the escape depth is low enough.

When electrons are incident on the sample surface, they are either repelled electrostatically due to Coulomb forces from already existing charge patches, shown by the dashed lines in Figure 4.35, or they interact with the surface or the bulk. If lower energy electrons interact with the surface, they can scatter (quasi-)elastically from atoms close to the surface and be transmitted toward the exit as shown by the dot-dashed lines in the figure. As a result, transmission is governed by a combination of charge patch deflection and Rutherford scattering for the lower energies. But, if the incident energy is higher (solid lines), electrons

penetrate further into the bulk of the capillary and lose energy due to various inelastic processes such as ionization or excitation of inner-shell electrons. If the escape depths of these electrons are sufficiently small, they can be transmitted through the capillary with energy loss, and, if not, the electrons will become lost within the bulk of the material. However, for deeper penetration into the bulk, the probability of secondary electrons to escape the sample is smaller, which causes more charge buildup on the surface. So, charge deposition and Rutherford scattering co-exist at a given energy, with both Rutherford scattering and Coulomb deflection causing transmission at lower energies and the charge deposition dominating at higher energies. The differences in electron and slow-ion transmission can be attributed to several reasons. Electrons are less efficient in charge deposition on the surface of the capillary than ions. The electron projectiles can scatter off the surface at the point of impact and make the surface more positive due to secondary electron emission. This makes the charge patch weaker, whereas ions have the advantage of causing secondary electron emission that always makes the patch stronger. The resulting charge patch due to electrons is reduced, making it difficult to create a sufficient Coulomb field to repel the incoming electrons from the wall to guide them along the capillary axis. As a result, more of the incoming electrons penetrate into the surface, where they undergo inelastic scattering and become lost, or they are transmitted through the capillary again after losing energy, if able to escape from the bulk.

Transmission of 300, 400, 500, 600, 800, and 1000 eV electrons through sample A was investigated again during the second phase of the experiment to study the angular FWHM with sample tilt angle for different energies, using a high-resolution spectrometer. The data collection process was similar to what was described earlier in this chapter. These data were taken after the transmission reached the steady state at every tilt angle Ψ, i.e., more than 2 hours after driving the beam on to the sample. The new parallel-plate spectrometer had ~ 10 times better angular resolution than the previous low-resolution one ($\sim 2.4^\circ$). The energy resolution of the new spectrometer was the same as the previous one, about 3%. A comparison of angular resolutions of the two spectrometers is given in Figure 4.36, where red dots show the angular resolution of the spectrometer which was used in the earlier measurements. Green stars show the resolution of the new spectrometer.The experiment was conducted using an electron beam which had a divergence of $\sim 0.6^\circ$. The direct region of the transmitted electrons was found to be $\Psi < 1^\circ$. The FWHMs of the intensities of the transmitted electrons were obtained by fitting symmetric Gaussians to the angular distributions of the data. Since the angular widths were well

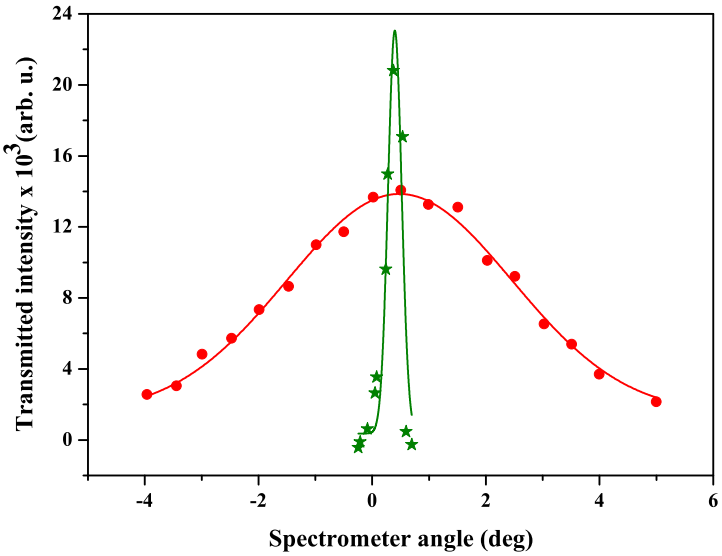

Figure 4.36: Comparison of angular profiles for the low and high resolution spectrometers. Each data point is the integrated intensity of the spectrum obtained at the given spectrometer angle at 500 eV. Data are fitted with symmetric Gaussians indicated by the solid lines, giving values for the FWHM of 2.4° and 0.3°, respectively, for the low (green stars) and high (red dots) resolution spectrometers.

beyond the instrumental errors, a FWHM analysis of the angular distributions was possible, unlike with the previous spectrometer. The 10 times better angular resolution of the spectrometer allowed more detailed investigation of the FWHM variations with the sample tilt angle. As stated, the angular FWHMs were obtained by fitting symmetric Gaussians to the angular distributions at different tilt angles and energies. The results are shown in Figure 4.37.

As seen, the width rapidly increases to a maximum at $\Psi = 1°$ for all the energies, followed by a fast falloff up to $\sim 3.5°$, before beginning a much slower falloff. This gives evidence for the existence of two regions, indirect 1 and

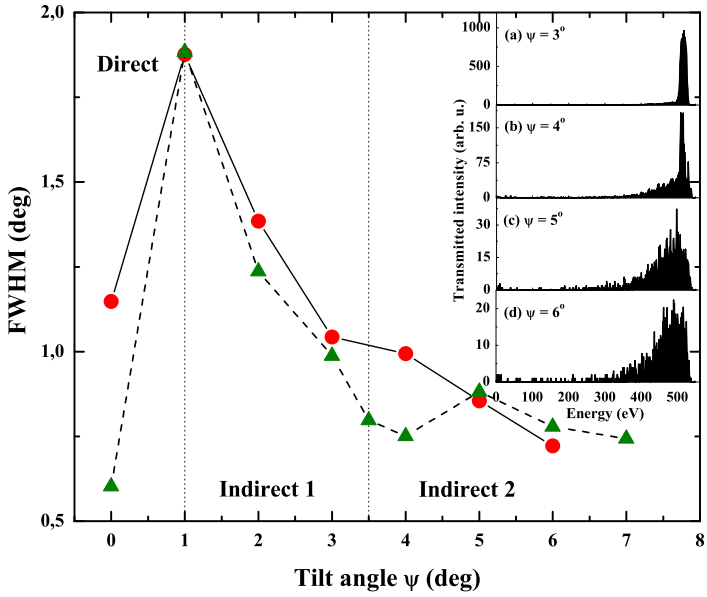

Figure 4.37: Variation of the angular FWHM with sample tilt angle for 500 (red dots) and 1000 eV (green triangles) energies showing two distinct regions within the indirect region. The inset shows the transmitted electron energy spectra for different tilt angles of the capillary at 500 eV.

indirect 2, in contrast to just one region seen previously in Figure 4.33. The narrowness in angular spread of the transmitted intensity at $\Psi = 0°$ for all energies is likely due to the absence of guided electrons within the transmitted intensity since the majority of the intensity contribution is from the direct beam component. On the other hand, the higher divergence of the FWHM at the beginning of the indirect region 1 can be attributed to the onset of guiding and scattering events. In this region, where elastic Coulomb repulsion is more dominant the FWHM, has a much faster falloff in width than the more inelastic

indirect region 2. This feature was not so prominent with the previous low resolution data because of the inability to distinguish the variation of spectra going from indirect region 1 towards indirect region 2, which spans only about 2° of the tilt angle range. These features for FWHM variations for electron transmission through nano- and microscale capillaries are different from those obtained with slow HCI [59, 66, 68], where narrower transmission profiles were observed for small tilt angles.

4.4.1 Summary

We showed that electrons can be transmitted through a single glass microcapillary even if the capillary is tilted with $\sim 5°$ against the beam axis. Due to the inelastic electron scattering from the inner surface the electrons lose energy but they can still pass through the capillary. We found that the intensity of the transmitted particles decreases with increasing tilt angles. We identified two significant regions, the so-called direct and indirect regions, in the transmitted electron intensities.

Direct transmission region means, where electrons do not interact with inner capillary wall before being transmitted through the capillary and indirect transmission region, where they interact at least once before being traversed.

The transmitted electrons suffered significant energy losses with increasing sample tilt in the indirect region. We found that the electrons with higher incident energies suffer larger energy losses with increasing tilt angle. The guiding ability of electrons was analysed by calculating the characteristic guiding angle Ψ_c (the tilt angle for which the transmitted intensity falls to 1/e) at different electron beam energies. We found that in the indirect region above 500 eV for tilt angles $\Psi > 2.5°$ the guiding angle of the capillary increased with increasing energy. This is completely different from what was observed in the case of slow positive ions and for fast electrons on nanocapillary foils, and also deviates from the theoretical predictions. This can be caused by the presence of two different processes during the transmission of the electrons through the sample. Rutherford scattering may be dominant at the lower energies, whereas Coulomb repulsion due to charge deposition overtakes it at higher energies.

4.5 The time evolution of electron transmission

In this subsection the time evolution of the transmission of 500 and 800 eV electrons through a single glass capillary at different tilt and observation angles is discussed.

Investigations of the transmission phenomenon and its variation with time (i.e. integrated charge) of the transmitted beam position have proved to be significant in learning about the dynamics of the guiding process [7, 15, 18, 25, 51, 52, 58, 60].

However, compared to the relatively large amount of research done on time evolution of HCIs [7, 25, 51, 66, 78], so far little has been done to investigate the time dependence of electron transmission, experimentally [15, 52, 71] or theoretically [18]. Consequently, many questions regarding the transmission process remain unsolved.

The same two glass capillaries which were used in the energy dependence measurements described in Chapter 4.4 were used for the measurements presented here. The beam was collimated by an aperture of diameter 1.5 mm and allowed to strike the samples. The transmitted electrons were analysed by an electrostatic parallel-plate analyser coupled to a channel electron multiplier, which was located a few centimeters behind the sample. Both the high and the low angular resolution spectrometers were used at different stages of the experiment.

The experiments were carried out at capillary tilt angles $\Psi = 0°$, $1°$, $2°$ and $3°$ for 500 eV, while measurement for a tilt angle of $\Psi = 2°$ was used for 800 eV. First, angular dependent data were taken by varying the analyzer angle Θ in small steps to collect the transmitted spectra, while keeping the tilt angle Ψ constant. After determining the centroid analyzer angle Θ at the particular Ψ, where the intensity of the transmitted electrons is the highest ($\Theta \approx \Psi$), the analyzer was moved to the centroid position and fixed. The beam was then blocked and the sample was allowed to be discharged for more than 12 hours before starting the collection of the time evolution data. The same procedure was repeated for all tilt angles at both energies.

The dependence of the intensity of the transmitted electron beam as a function of time for 500 eV, at tilt angles $\Psi = 0°$, $1°$, $2°$ and $3°$ with sample A, and for 800 eV, at $\Psi = 2°$ with sample B, are presented in 4.38 a and 4.38 b, respectively. Each data point represents the integrated spectrum over a period of 40 s for 500 eV and 110 s for 800 eV. Intensities of all tilt angles have been normalized with respect to the beam current ($\sim$ 60 pA) at $\Psi = 1°$ for 500 eV as measured on the sample. In the case of $\Psi = 2°$ at 800 eV a slightly de-focused

beam was used, which had about 6 times lower flux. Geometrical calculations of the setup, including beam divergence, indicate that the indirect region of the transmission, where electrons interact with the inner wall of the capillary at

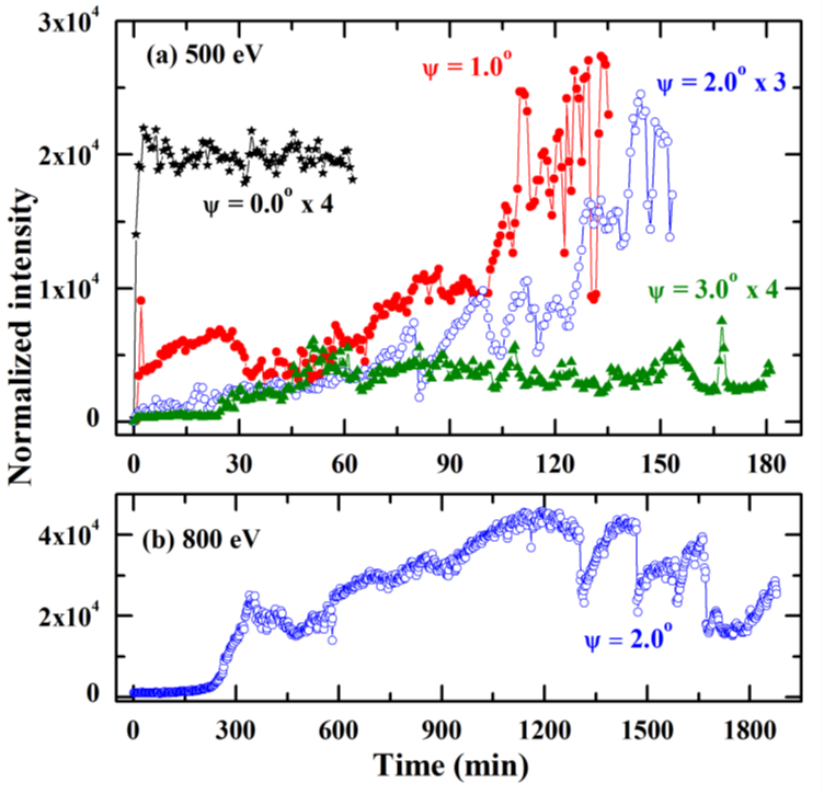

Figure 4.38: Intensity variation of the spectra with time for 500 and 800 eV. Transmitted intensities are normalized with respect to current on the sample at $\Psi = 1^\circ$ for 500 eV. Intensities for $\Psi = 0^\circ$, 2° and 3° in part (a) have been multiplied by 4, 3 and 4, respectively, for better visualization. All data were taken at an observation angle about equal to tilt angle ($\Theta \approx \Psi$), where the maximum transmitted intensity was seen.

least once before being transmitted through, occurs for $\Psi > 1°$. However, the intensity at $\Psi = 1°$ for 500 eV looks like to have component of the direct beam as well.

For $\Psi = 0°$ at 500 eV, electron transmission was detected almost immediately after the beam hit the sample and remained constant over the course of time as shown in Figure 4.38 (a). This result contradicts with previously reported electron transmission through a Al_2O_3 nanocapillary foil [15], where an exponential decay was observed starting at t = 0. The transmission at $\Psi = 0°$ is mainly due to the direct beam. The process is much slower in the indirect region, where it took 30 - 40 minutes for substantial electron transmission to begin for 500 eV, and 200 - 300 minutes for 800 eV (see Figure 4.38). The difference between 500 eV and 800 eV can be due to the lower beam flux used in the latter case. As the intensity goes to equilibrium, the time evolution for $\Psi = 2°$ reflects sharp oscillations after some time for both 500 and 800 eV, whereas it is less obvious for the $\Psi = 1°$ and 3° curves of 500 eV, although the overall behavior of these curves is the same.

To understand this scenario further, the centroid energies and corresponding full-width-half-maximum (FWHM) values of the obtained energy spectra were calculated according to Eq. 4.3 and Eq. 4.4. The changing of the FWHM of the quasi-elastic peaks and the average energy of the transmitted electrons from the first minute of each measurement were studied for all tilt angles till the equilibrium is reached. In each case to determine the corresponding value of the FWHMs and the energies the average of five cycles was taken to improve the statistics. When the capillary was tilted with 2° in the equilibrium region each quasi-elastic peak was plotted and fitted. Figure 4.39 (b) and 4.40 (b) show how the FWHM of the spectra changes with time. In all graphs the average of the FWHMs and the energies of the transmitted electrons are indicated when the guiding reached the equilibrium state.

In the case of 0° the inner wall of the capillary will obtain charge roughly evenly because of the beam divergence. Thereby the peak will be shifted downwards and has asymmetric shape as it can be seen in Figure 4.39 (a). The average energy of the transmitted electrons will be lower and the FWHM will be larger than it would be without putting capillary into the beam direction. Figure 4.39 (b) shows the normalized intensity of the transmitted electrons (red dots) and the FWHMs (black triangles) as functions of the time.

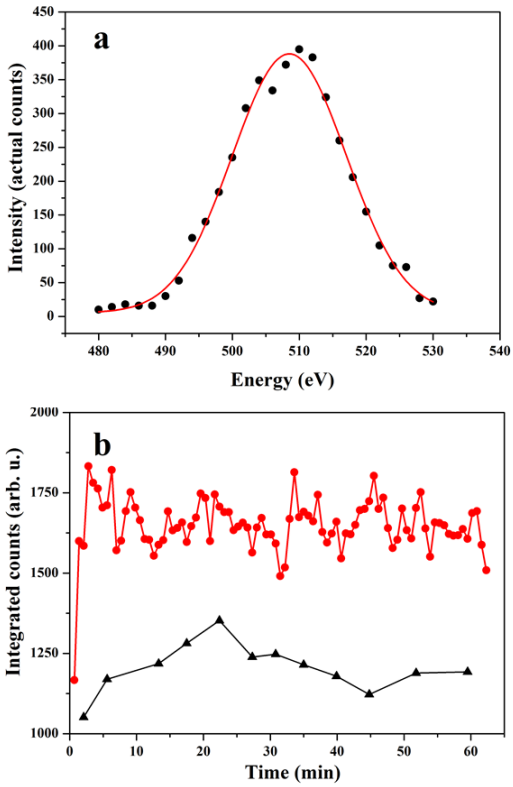

Figure 4.39: a) Spectrum of the transmitted electrons at 500 eV for capillary tilt angle Ψ=0°. b) Time dependence of the electron transmission through the capillary at tilt angle Ψ=0°; normalized intensities (red dots) and FWHMs (black triangles).

When the capillary is tilted by 2° (see Figure 4.40 (a) and (b)) the incident beam charges roughly semicircularly and mainly the opposite side of the inner wall of the capillary. The developing field will have more and more crosswise direction compared to the axis of the capillary, and will deflect the incident electrons. After a while the incident electrons will not touch the opposite wall,

and the number of the deflected electrons will increase. Therefore, the electrons will suffer smaller degree deflections, the yield and the energy of the electrons

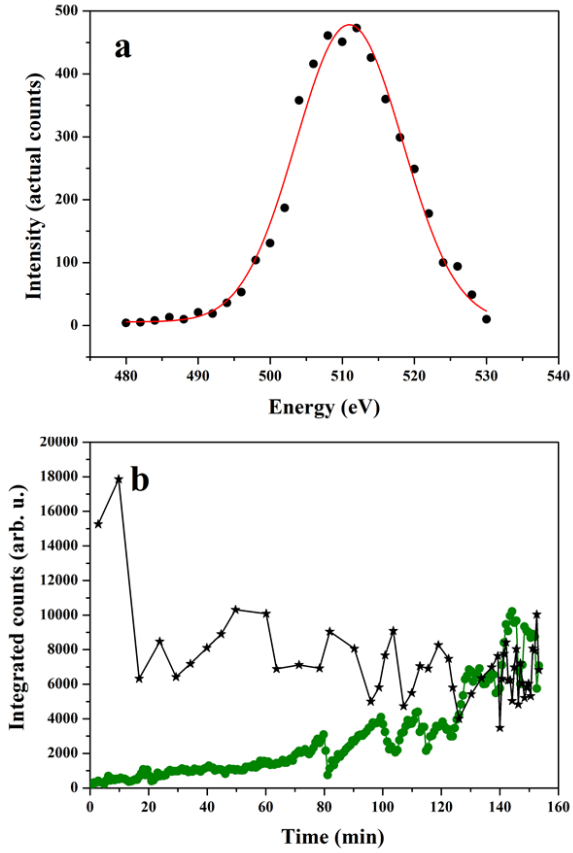

Figure 4.40: a) Spectrum of the transmitted electrons at 500 eV for capillary tilt angle Ψ=2°. b) Time dependence of the transmitted electron yield through the capillary at Ψ=2°; normalized intensities (green dots) and FWHMs (black stars).

will increase, while the FWHM will decrease. Later the force with crosswise direction will be too large and will deflect the electrons to the opposite wall. The yield decreases radically, the energy of the transmitted electrons will also decrease and the FWHM will increase. When this part of the inner wall of the capillary gets charged up and the force again has the advantageous direction, the yield will increase again significantly, the energy will increase and the FWHM will decrease again. These two tendencies will alternate till on the whole inner length of the capillary the forces (mainly of transverse direction), which help to guide electrons through the capillary, are developed. The intensity (green dots) and the FWHM (black stars) fluctuate in opposite phases, as it can be seen in Figure 4.40 (b). As time passes, the shape of the peaks becomes more and more symmetric.

Both the centroid energies and FWHM values for $\Psi = 0^\circ$ remain almost constant over the course of time as shown in Figures. 4.41 (e) and (i) and never reach the bare beam values. The calculated values are compared with the respective bare beam (without sample) values. According to the geometrical calculations, including the beam divergence and finite opening of the sample, $\sim 20\%$ of the incoming beam still hits the inner surface at $\Psi = 0^\circ$, which can give rise to an inner wall charge up of the capillary. The charging rate depends directly on the flux density of the incoming beam. When the experiment was carried out at $\Psi = 0^\circ$, the beam flux was kept at a lower value and also ran only for ~ 60 minutes, giving less time for the charge up process. At $\Psi = 1^\circ$, where some component of the direct beam still passes through the capillary, Figures. 4.41 (f) and (j) show the centroid and FWHM energy values have a similar trend and fall below and above the bare beam values, respectively. However, some oscillatory characteristics can be seen for $\Psi = 1^\circ$. In the indirect region for $\Psi > 1^\circ$, the centroid energies increase while the widths decrease with time for the tilt angles 2.0° and 3.0°, and finally level off at the bare beam values as shown in Figure 4.41(g), (k) and 4.41(h) and (l). Both the centroids and widths for $\Psi = 3^\circ$ reach the respective bare beam values ~ 50 minutes earlier than those for $\Psi = 2^\circ$.

Discharging data for 800 eV are shown in Figure 4.42 (a) were taken immediately after the charging measurements as a continuation. Data were collected by blocking the electron beam for some time (intervals of 5 - 30 minutes) allowing the sample to discharge, and then putting the beam back on the sample for short periods (1 - 2 minutes) to collect transmitted electrons. It is seen that discharging occurs quite rapidly (about an hour for total discharge), and that the transmission goes nearly back to the value it had at the beginning of the measurements falling exponentially with a decay constant equal to 8 minutes.

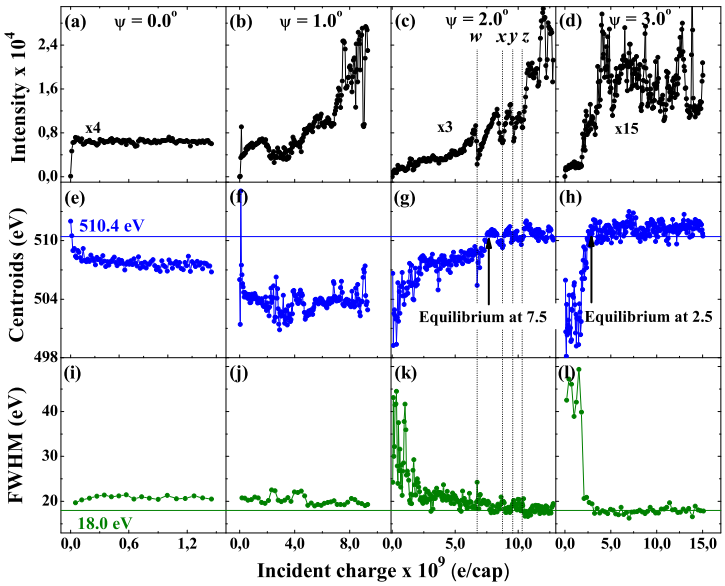

Figure 4.41: Variation of intensity, centroid energies, and FWHMs with integrated charge for 500 eV at different tilt angles Ψ. The centroids have been calculated for all points of each spectrum. For the FWHMs an average of 5 spectra has been considered for better statistics for $\Psi = 0°$, $1°$ and $3°$, whereas for $\Psi = 2°$the FWHM is plotted for every point. Blue and green solid lines show the centroid (510.4 eV) and FWHM (18.0 eV) values for the bare beam. Letters w-z in panel (c) show the sudden discharging of the transmitted intensity at $\Psi = 2°$.

A progression of transmitted spectra for 800 eV at $\Psi = 2°$, as shown in Figure 4.43, indicates an overall increase in transmitted intensity as it approaches equilibrium. The spectra were similar for 500 eV as well. The increasing dominance of (quasi-) elastically transmitted electrons over time compared to inelastically transmitted electrons is evident from the sequence of the spectra. The spectra

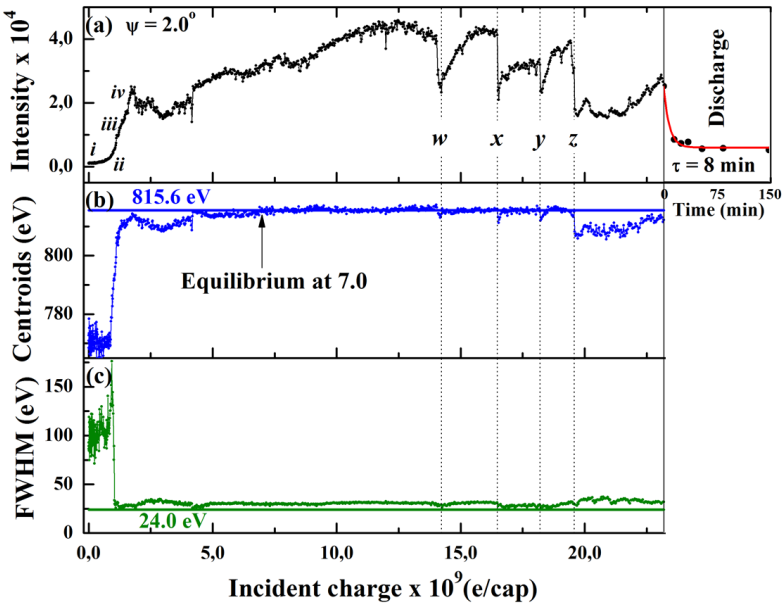

Figure 4.42: Variation in transmitted beam intensity (a), centroid energy (b), and FWHM values (c) for 800 eV electrons at $\Psi = 2^\circ$ as a function of integrated charge. The blue solid line shows the bare beam (i.e., no sample) centroid at 815.6 eV, and the green solid line the bare beam FWHM at 24.0 eV. The dotted lines indicate sudden discharging of the capillary. Discharging data are also shown for a span of about 150 minutes and are fitted with a first order exponential decay curve. The decay constant (τ) is given at the bottom of the discharging panel.

also show sudden rapid decreases in the transmitted intensities in Figure 4.43 (e), (f) and Figure 4.43 (g), (h) within a period of less than 2 minutes. The transmitted spectra of 800 eV electrons show evidence for a double peak structure with a small shoulder of a secondary peak $\sim$ 15 eV lower than the elastic peak as seen in Figs. 4.43 (d)and (h). The lower energy peak could be due

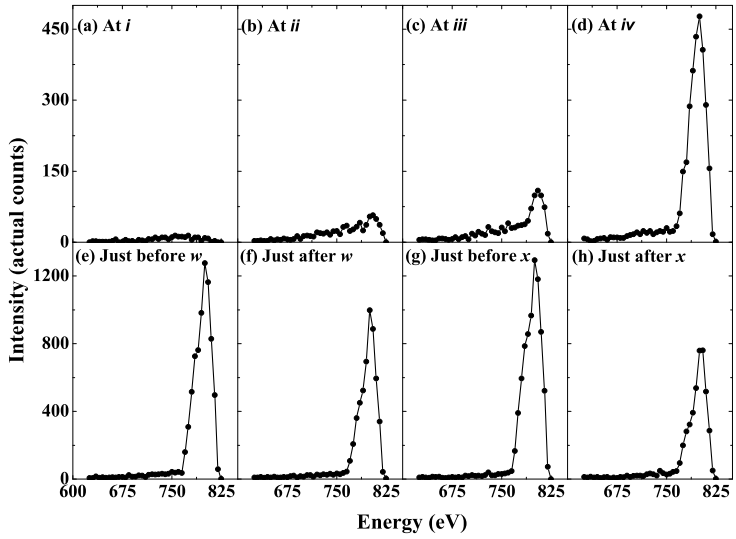

Figure 4.43: Measured electron energy spectra for different integrated charges for 800 eV at $\Psi = 2^{\circ}$. The corresponding locations for each spectrum are indicated in Figure 4.38 a by the letters i-iv and w, x. The elastically transmitted fraction of electrons generally increases with time, compared to the inelastic contribution. Sudden oscillations in the transmitted intensity can be clearly seen from panels e, f and from g, h.

to electrons which lose energy by ionizing weakly bound valence electrons of Si or O atoms in the capillary wall. As a result the combined structure yields a higher width than the FWHM of bare beam.

A striking feature of the charging dynamics is the sharp oscillatory behavior for both along and away from the capillary axis, as seen at $\Psi = \Theta = 2^{\circ}$ for 500 and 800 eV (Figure 4.41 and 4.42). This result can not be seen for the direct beam. It is also possible to see some oscillations for both $\Psi = 1^{\circ}$ and 3° at 500 eV in Figure 4.42 b) and (d), but they are not as pronounced as at 2°. Since some of the direct beam still gets through the capillary at 1°, the

oscillations can be overshadowed by the more intense direct beam component. In the case of 3°, the lower statistics of the transmitted intensity (about 5 times worse than at 2°) probably caused the oscillations not to be so sharp. According to recently reported 22.5 keV Kr^{9+} ion deflection by a borosilicate glass surface [58], the temperature dependence of the sample can trigger a thermally activated transportation mechanism of carriers to enhance the discharging process. This could be responsible for the increase in frequency of intensity oscillations in both the 500 and 800 eV electron data. (A slight increment in incident beam flux over time in the present work might also have contributed to this). Such transmitted intensity characteristics due to discharging have not been reported for electron or ion transmission through nano- or microcapillaries.

When electrons interact with the surface, they can either scatter (quasi-) elastically or inelastically from atoms close to the surface or be repelled electrostatically due to Coulombic forces from already existing charge patches. These processes can cause the electrons to be transmitted toward the exit or penetrate further into the bulk of the capillary and lose energy due to various inelastic processes such as ionization or excitation of inner-shell electrons [81]. When the beam is incident on the inner surface at time t = 0, some electrons start to introduce charge up in a small area around the impact point of the beam, while others penetrate into the bulk of the capillary and scatter elastically or inelastically. If the escape depths of these latter electrons are sufficiently small, they can be transmitted through the capillary with some energy loss, giving rise to the transmission spectra shown in Figures 4.43 (a), (b) and (c). These spectra will have lower average energies resulting in lower centroid values and larger FWHMs for time values near t = 0, as seen in Figures 4.41 (g),(h),(k),(l), respectively. If not, they become lost within the bulk of the material, lowering the overall transmitted intensity. The deposited charges on the capillary surface are spread along the projection area of the beam with time, eventually creating a stronger charge patch close to the entrance which deflects subsequent electrons away towards the exit. This lowers the beam interaction with the surface and gives rise to the quasi-elastically transmitted electrons as seen in Figures. 4.43 (d),(h). As a consequence, the average centroid energy of transmitted electrons increases, whereas the FWHM decreases. Eventually the centroids and FWHMs level off at the bare beam values when transmission equilibrium is reached as seen in Figures 4.41 (c), (d) and (g), (h). Furthermore, increase in tilt angle corresponds to an increase in surface charge density as the beam is deposited in a smaller area. Therefore, the charging process at $\Psi = 3°$ is faster than at $\Psi = 2°$, which is seen in Figure 4.41 by the centroids and FWHMs.

Table 4.2: *Values of the average centroid energy and corresponding FWHM for the different tilt angles*

Tilt angle (°)	Average centroid energy (eV)	Average FWHM (eV)
0°	507.9 ± 0.2	20.3 ± 0.2
1°	503.5 ± 0.7	19.7 ± 0.7
2°	510.9 ± 0.3	17.8 ± 0.6
3°	512.1 ± 0.5	17.5 ± 0.5

A comparison of experimental values of centroid energies and FWHMs in the equilibrium state is given in Table 4.2.

The dependence of the intensity of the transmitted electron beam on the incident charge for 500 and 800 eV at $\Psi = 2^{\circ}$ are presented in Figure 4.44. Each data point represents the integrated energy spectrum over a period of 105s for 500 eV and 110 s for 800 eV. The centroid energies represent the mean value of the obtained energy spectra, see Eq. 4.3.

Both integrated intensities and centroid energies have been plotted with respect to the incident electrons per capillary (e/cap). Different beam collimations were used for the two energies. Geometrical calculations reveal the direct transmission of electrons (no interaction with the capillary inner wall) to occur for $\Psi < 2.5^{\circ}$ and $\Psi < 1^{\circ}$ for 500 and 800 eV, respectively, due to different distances from the electron source to the collimation system that were used. In these measurements, in both cases the spectrometer angle Θ was taken a bit away from the centroid angular position. Neither of the energies seems to have reached the respective incident beam values even in the equilibrium state. The reason of it is seems to be the slightly off axis of the observation angle.

The figures also show the centroid energy values for the primary (bare) beam without the sample by the solid lines. The variation of intensity for both cases has similar characteristics with a sudden burst of intensity near the beginning followed by more stable and constant transmission. Periodic intensity drops are visible in the later region for both energies. The centroid (mean) energy for 500 eV decreases after an initial fast rise, and then levels off at ~ 4 eV below its primary beam value, whereas 800 eV shows a nearly constant value throughout the course of the measurement, which is ~ 1 eV below its respective bare beam value on average.

As shown by the arrows in Figure 4.44, for both energies the transmitted intensity shows notable periodic oscillations during the course of the measurement.

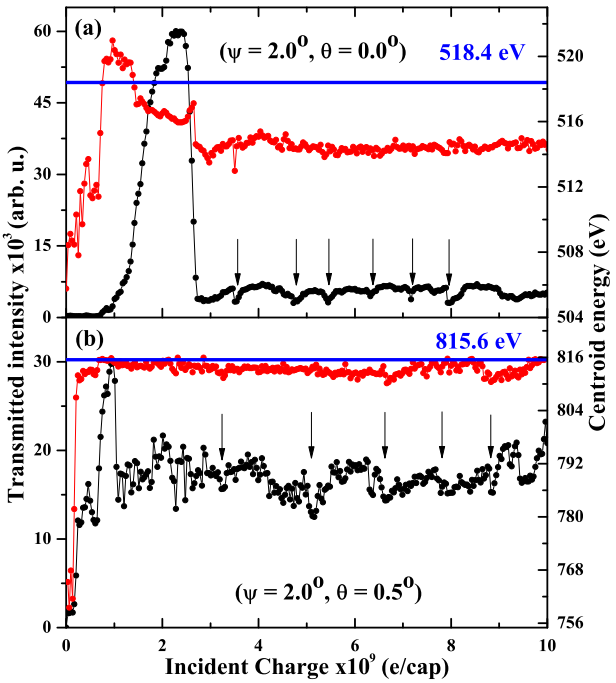

Figure 4.44: Variation of intensity (black points) and centroid energies (red points) with integrated charge at $\Psi = 2^\circ$ for 500 and 800 eV at $\Theta = 0^\circ$ and 0.5°, respectively. Blue solid lines show the centroid (518.4 eV and 815.6 eV) values for the bare beam without the sample. Black arrows point to the sudden intensity drops that occurred periodically.

This kind of behavior is possible when deposited charges near the capillary entrance reach a critical value, causing a sudden discharge along the surface to the conducting coating at the entrance, or possibly to the bulk, leading to a sudden drop in the transmitted intensity [71]. For the case of 500 eV, initial trans-

mission is contributed by the direct beam component, as $\Psi = 2^\circ$ is within the direct region of transmission due to the geometry of the setup. Since Coulombic deflection is at its minimum at the beginning, the intensity of the transmission of the elastically scattered electrons due to deflection is low initially. As a result, the majority of the transmission is comprised of direct beam, which gives rise to the higher centroid energy values seen at the beginning of Figure 4.44 (a). But as the scattering processes sets in, the dominance of the direct beam slowly diminishes, causing a decline in the centroid energy values before it reaches equilibrium around $\sim 3 \times 10^9$ e/cap. The variations of centroid energies at 800 eV are much different than for 500 eV. Centroid energies increase at the beginning and level off at the equilibrium value $\sim 1 \times 10^9$ e/cap. Since $\Psi = 2^\circ$ for the 800 eV setup is well within the indirect region, no direct beam contribution is possible here. Inelastic scattering from the uncharged capillary surface at initial stages thus reduces the centroid energies at the beginning before relatively more elastic Coulombic deflection processes initiate. Coulombic repulsion has been established as the driving force behind HCI guiding through capillaries, for which beam interactions with the capillary surface are inhibited due to charge accumulation, giving rise to elastic transmission of charged particles. Such guiding effects are believed to exist in electron transmission as well [70], but it is less effective compared to HCIs due to the inability of electrons to make strong charge patches.

Closer view on the recovery after breakdown for the intensity oscillations is shown in Figure 4.45. All data presented represent recoveries after the first breakdown in the respective spectra. The data are fitted with exponential functions. The solid red lines indicate the fitting curve C + D $e^{\frac{-Q}{Q_o}}$, where C, D, and Q_0 are fitting constants and Q is the incident charge. The results for the three curves of each set share similar features with the initial recovery times in Figures 4.45 (a), (d), (g) (initial charging) having a higher charge constant (Q_0) than the subsequent recovery times as seen in Figures 4.45 (b), (c), (e), (f), (h), (i), which are smaller and have nearly equal values for all three cases. It is noteworthy to mention that charging constants were almost the same, except for the initial charging, even beyond the oscillations shown in Figure 4.45. The charge constants after the first recovery for 800 eV are found to have slightly higher values than those for 500 eV, whereas the high flux 500 eV results, see Figure 4.45 (d), (e), (f), were found to yield higher Q_0 values compared to low flux 500 eV data in Figure 4.45 (g), (h), (i). From the bottom two panel rows of Figure 4.45 for 500 eV, it can be inferred that the flux density of the beam has a direct impact on capillary charging. More than two times higher beam flux in Figures 4.45 (d), (e), (f) has increased Q_0 by ~ 1.5 times for the case of charge up in

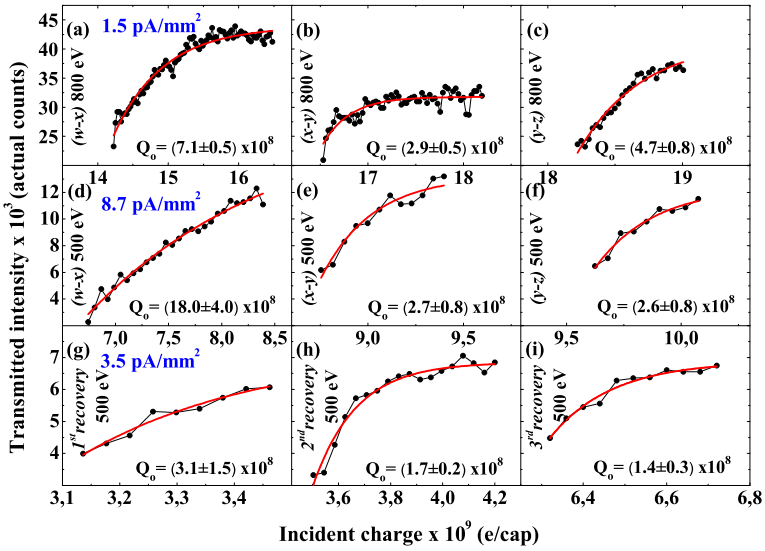

Figure 4.45: First order exponential fittings to the recoveries after breakdown in the intensity oscillations for 800 and 500 eV seen at w-x, x-y and y-z in Figure 4.41 c and Figure 4.42 a, respectively. Similar results are plotted for 500 eV at $\Psi = 2^\circ$ and $\Theta = 0^\circ$ for the three recoveries after the first breakdown of the capillary in Figure 4.44. Red solid curves represent the fittings. The flux density for each case is given in the first panel column. Decay constants obtained from the fittings are given at the bottom of each plot.

Figures 4.45 (e), (f) compared to 4.45 (h), (i). The higher charging constants found for 800 eV compared to those for 500 eV indicate the ability to hold more charge at higher energy. This is attributed to lower secondary electron emission at higher energies. The oscillatory characteristics for both the cases (along and away from the capillary axis) were observed after the transmission equilibrium was reached. The transmission equilibrium is a competition of charging and discharging processes occurring at the same time. As charges deposit on the inner surface, they can migrate along the surface changing the distribution, as

well as into the bulk. As the deposited charge density increases and equilibrium is reached between charging and discharging, the primary beam interaction with the surface minimizes as it interacts more strongly with the charge patch. This indicates that when the deposited charges near the capillary entrance reach a critical value, a sudden discharge occurs along the surface to the conducting coating at the entrance, or less probably to the bulk, leading to a sudden drop in the transmitted intensity. The drops in intensity are not likely due to beam deflections; they indicate a charge breakdown instead. Furthermore, the quasi-elastic peaks of transmitted electron spectra in Figure 4.43 (e), (f) and (g), (h) indicate that the source of transmission remains the same just before and just after an oscillation. Figure 4.43 (f) and (h) indicate that the remaining charge patches after the partial discharge are still capable of elastically deflecting the incoming electrons. After the partial discharge, the charge accumulation slowly recovers and the process continues.

4.5.1 Summary

We studied the charge dependence of the electron transmission for incident electron energy at 500 eV and 800 eV at different capillary tilt angles. We demonstrated that the electron transmission through a single glass microcapillary has time- (charge-) dependent behavior. When the transmitted intensity goes to equilibrium, the centroid energies and the corresponding full width at half maximum (FWHM) of the transmitted electron distributions are found to vary in phase and out of phase with the transmitted intensity, respectively. Transmission comes to equilibrium when the charging and discharging processes compensate for each other. We found, however, that the stable equilibrium was never fully reached even for large integrated charge due to repeated sudden partial discharge of the charge patch from time to time. Such non-equilibrium has not been previously observed for electron or ion transmission through capillaries.

Chapter 5

Outlook

In the fourth chapter, which contains the results of my work, I have summarized my results at the end of each subsections. Instead of repeating those again, here I give an outlook for the possible applications of the results, and I introduce the plans for the future. The data presented in my PhD thesis strongly support that the guiding effect known from nanocapillaries is also valid up to microscopic dimensions of the order of millimeter. Due to the guiding effect, one can position the beam and adjust its direction mechanically, without the necessity of electric or magnetic deflection and focusing systems. This opens the possibility of producing cheap alternatives to complex electron-optical tools with their electronic equipment still having reasonable brilliance. Eventually, such micro-capillaries could be interesting alternative ion-optical tools for various applications, especially where the size, the costs or the accessibility are critical factors. Concerning the quality of the beam, we have strong evidence, that the charge-state of the ions is kept during the guiding through the glass capillary, which is an important feature for possible applications.

Nano-beams can be used to manipulate molecules and atoms on surfaces, so demand is growing for their use in the fabrication of semiconductor materials. The creation of nano-sized protrusions on insulating surfaces using slow highly charged ion beams of well-defined size makes it possible to form regular structures on surfaces without inducing defects in deeper lying crystal layers. One intriguing challenge is the production of ordered patterns of nanohillocks by HCI impact on insulator surfaces. A new pathway for controlled projectile positioning has opened: based on self-organized guiding of charged particles through single glass capillary without change of the initial charge state.

Capillary guiding can also be used in biological and medical applications. With the use of a single glass capillary, one can irradiate a single organelle, or even a part of one. The advantage of glass is that it is transparent and thus enables researchers to observe the irradiation point directly using an optical microscope. This directly impacts research into the biological effects of heavy ion irradiation, which have been studied extensively during the last decades. As a medical application, heavy-ion radiotherapy has the advantage that energetic charged particles are able to effectively kill cancer cells with minimal damage to the surrounding tissue by concentrating the deposited energy, near the Bragg peak, directly into the tumor. However, a crucial point of the tumor irradiation with heavy ions is the question that how accurate is the beam transport to the cancer cells.

In accordance with my thesis it is clear that there are still many open questions regarding to particle guiding. Therefore we have well defined plans for our future investigations. Here I would like to specify only a few of them: we plan to investigate the influence of different external fields on the guiding effect using special samples. This could lead to a possible enhancement of transmission or a better beam emittance at the exit of the capillary. We will investigate the transmission of projectiles with single charges through a single glass microcapillary. Measurements to study the transmission of proton microbeam [81] through different metallic and insulating samples will also be performed. We want to perform high energy-resolution measurements to investigate electron guiding through different insulating samples. We plan to investigate positron transport through a single microcapillary for possible future technical applications either in producing intense, well focused positron beams for atomic collision experiments or use as a tool in producing antimatter. We will study the focusing properties of single insulating capillaries of microscopic size and the properties of positron transmission through various target materials.

Chapter 6

Összefoglalás

Doktori értekezésemben töltött részecskék kölcsönhatását vizsgáltam egyedi, mikroszkopikus méretű üvegkapillárisokkal. Az első, szigetelő mintával, polimerekbe (polyethylene terephthalate, Mylar) maratott nanométeres, hengeres kapillárisokkal történt kísérletek [7] azt a nem várt eredményt hozták, hogy a szigetelő kapillárisok képesek átvezetni töltésállapot változás nélkül a nagytöltésű ionokat, még akkor is, ha a geometriai feltételek ezt nem tennék lehetővé. Az töltött részecskék kapillárisokon történő átvezetése a kapillárisokban kialakuló elektromos mezővel hozható összefüggésbe. Ehhez a kapillárisok belső falának töltést kell felhalmozni, egyrészt ahhoz, hogy az elektromos taszítás megakadályozhassa az ionok közeli ütközéseit a felülettel, ezáltal meggátolva az elektronbefogást a felületből, másrészt ahhoz, hogy az ionokat a kijárati nyílás felé terelje. A feltöltődési fázisban a beeső ionok egy önszervező folyamatban pozitív töltésfoltot helyeznek el a kapilláris belső felszínén, amely ezután felületi és tömbi diffúzióval vándorol a felületen és a tömbben. A később beérkező ionok visszaverődhetnek a töltésfolt Coulomb taszítása következtében, végül a kapilláris belső falával való ütközés nélkül jutnak át azon. Átvezetés akkor figyelhető meg, amikor a falba való ütközés (feltöltődés) és a tömbi vagy felületi transzport (kisülés) között egyensúlyi állapot alakul ki. A jelenlegi elméleti eredmények azt mutatják, hogy a lerakódó töltések jelentős része a kapilláris bemeneténél helyezkedik el. Már ez az egy töltésfelhalmozódás által keltett elektromos tér elegendő a beérkező ionok kapillárison történő átvezetéséhez. A kapilláris nyalábtengelyhez képesti dőlésszögétől, a kapilláris hosszától és a beérkező töltés mennyiségétől függően további kisebb feltöltődött foltok alakulhatnak ki a kapilláris belső felületén. Annak ellenére, hogy az elmúlt néhány

évben nagyszámú kutatócsoport csatlakozott ehhez a területhez, és sokféle kísérletet végzett el szigetelő, pl. Al_2O_3, SiO_2, üveg kapillárisokkal, a kölcsönhatások számos részlete még ismeretlen. Az első mérésekhez multi-kapillárisokat használtak mintaként, amellyel számos hibaforrást vihettek be a kísérletekbe. A fóliába maratott vagy bombázással kialakított csövecskék tökéletes párhuzamosságát nem lehet biztosítani. Hasonló nehézséget jelent a megfigyelések elméleti leírása is. Az egymás közelében lévő töltött kapillárisok kölcsönhatnak egymással, így a pontos ionpályák meghatározásához a kapilláris kötegek kollektív hatását is figyelembe kell venni, ami igen bonyolulttá teszi az elméleti leírást. Ezért, a kísérleti körülményeket egyszerűsítendő, könnyen reprodukálható méréseket végeztem. Kutatómunkám során egyedi mikroszkopikus méretű kapillárisokkal vizsgáltam a töltött részecske terelés jelenségét, mert a jelenlegi technikai feltételek mellett egyedi nanoméretű csővel nem lehet megvalósítani a kísérleteket. Részben, mert bonyolult ilyen típusú mintát előállítani, másrészt pedig maga a kísérlet kivitelezése is nehézségekbe ütközik.

A kapillárissal végzett kísérletek kulcsfontosságú eleme a megfelelő minta előállítása. Méréseink során egyedi, mikroszkopikus méretű hengeres üveg-kapillárist használtunk, melyeknek hosszúsága, $l \sim 14$ mm, belső átmérője, $d \sim 0.17$ mm, így a hossz - átmérő aránya (l / $d \sim 80$) volt. A töltött részecske tereléses kísérletek kritikus pontja, hogy mennyire tudjuk biztosítani, majd reprodukálni a nyaláb és a kapilláris tengelyének párhuzamosságát. A szisztematikus vizsgálatokhoz szükséges minták előállítására egy eljárást fejlesztettem ki az MTA Atommagkutató Intézetében [66].

A doktori értekezésben tárgyalt kísérletek a töltött részecskék típusát tekintve két fő részre, az ion- és az elektrontereléses vizsgálatokra tagolódik. Az ionátvezetéses kísérleteket 4.5 keV energiájú, Ar^{9+} ionokkal végeztem el. A nyalábot a Bécsi Műszaki Egyetem 14.5 GHz-es ECR (Electron Cyclotron Resonance) ionforrása segítségével állítottuk elő. Az ionterelés szögfüggésének méréséhez a feltöltetlen kapillárist a bemenő nyaláb tengelyével párhuzamosan állítottuk be, majd lépésenként növeltük a kapilláris dőlésszögét a nyalábtengelyhez képest. Ezen kísérletekkel elsőként mutattam meg, hogy a nanokapillárisoknál tapasztalt töltött részecske átvezetés mikroszkopikus méretű kapillárisok esetében is megfigyelhető. Azt tapasztaltam, hogy jelentős átvitel tapasztalható még a nyalábtengelyhez képest nagy szögben döntött kapillárisok esetében is. Ezen eredmények egyértelműen bizonyítják, hogy az átviteli tér felépülése időfüggő folyamat, melynek kialakulása után stabil az átvitel [66, 68]. Azt is kimutattuk, hogy az átjutott ionok szögeloszlása keskenyebb a primer nyalábénál, azaz a kapillárisnak fókuszáló, nyalábformáló tulajdonsága van [66, 68, 78, 79].

A terelési folyamat optimalizálásának egyik módja a szigetelő anyag elektromos vezetőképességének megváltoztatása. Az üveg elektromos vezetőképességének erős hőmérsékletfüggése van, ami közel exponenciális-függés. Ez lehet a kulcsa a terelési mechanizmus szabályozásának. Ahhoz, hogy a kapillárissal történő ionterelés jelenségének hőmérsékletfüggését vizsgálni tudjuk, a Bécsi Műszaki Egyetem Atom és Plazmafizikai Csoportjával együttműködésben kifejlesztettem és megépítettem az első hűthető-fűthető mintatartót [67]. Eredményeinkkel elsőként mutattuk meg, hogy a kapilláris hőmérsékletének megváltoztatásával több nagyságrenddel tudjuk változtatni a boroszilikát üveg elektromos vezetőképességét, ezáltal tanulmányozható a kapilláris belsejében a töltésfolt felépülése és a kisülés folyamata [69]. Az ionterelés állapotát az alacsony hőmérsékleten bekövetkező ionterelés blokkolásától, a szobahőmérsékleten létrejövő maximális hatékonyságú átvezetésen át, az ütközésmentes geometriai átvitelig tudtuk szabályozni [69].

Az elektronok egyedi kapillárissal történő terelésének vizsgálata a kalamazooi Western Michigan University Van de Graaff gyorsító laboratóriumában történt, ahol 300 - 1000 eV energiatartományban vizsgáltuk elektronok üvegkapillárison történő átvitelét. Méréseinkkel megmutattuk, hogy a mikroszkopikus méretű szigetelő cső is képes átvezetni az elektronokat, még a kapillárisnak a bemenő nyaláb tengelyéhez képesti nagy dőlésszöge ($\Psi \sim 5^\circ$) esetén is. Az elektronok a kapillárison való áthaladásuk során, szemben az ionos kísérletekben tapasztaltakkal, jelentős energiaveszteséget szenvednek az üveg falával történő rugalmatlan ütközés következtében [70, 72, 74, 77]. A vizsgált energiák esetén azt tapasztaltuk, hogy mind az iontereléstől, mind a lassú elektronok transzportjától eltérő módon, a kapilláris dőlésszögétől függően két, egy direkt és egy indirekt régiót különböztethetünk meg az átmenő elektronok intenzitásának függvényében. A direkt régióban az elektronok nem ütköznek a kapilláris belső falával áthaladásuk során, míg az indirekt régió esetén az adott geometria mellett az elektronok legalább egyszer ütközhetnek a minta belső falával. A direkt régióban az átmenő elektron intenzitásának csökkenése független a bemenő elektron energiájától. Ezzel szemben az indirekt régióban energiafüggés figyelhető meg, a nagyobb energiájú bemenő elektronnyaláb energiavesztesége nagyobb, és az energiaveszteség növekszik a növekvő kapilláris dőlésszöggel [71]. Az elektronterelés hatékonyságát a karakterisztikus terelési szög Ψ_c (az a kapilláris dőlésszög, amelynél az átjutott részecskék intenzitása 1/e értékre csökken) kiszámolásával határoztuk meg. Azt az eredményt kaptuk, hogy a kapilláris terelési szöge az indirekt régióban, 500 eV energia fölött növekvő energiával nő. Ez az eredmény eltér a lassú pozitív ionok és gyors elektronok esetén nanokapilláris mintákkal végzett mérések során tapasztaltakkal, és a je-

lenlegi elméleti jóslatokkal is ellentmondásban van. Ennek oka, hogy a terelés folyamán alacsonyabb energiáknál a Rutherford szórás, magasabb energiáknál a Coulomb taszítás játszhatja a domináns szerepet [70].

Az elektronátvitel energiafüggése mellett vizsgáltuk az elektronok szigetelő kapillárison való átvezetésének időfüggését is 500 eV és 800 eV energiájú részecskékkel. Megmutattuk, hogy az elektronok egyedi üveg mikrokapillárissal történő terelése időfüggő folyamat. Megfigyeltük, hogy ellentétben az ionos méréseknél tapasztaltakkal, az elektronoknál a kapilláris besugárzását követően azonnal bekövetkezik az átvitel. Kezdetben az elektronok rugalmatlan szóródása következtében az átmenő töltött részecske-intenzitás alacsony. A kapilláris bemenetnél az idővel fokozatosan növekvő, lerakódott töltésfolt egy idő után rugalmas ütközéssel eltéríti a beérkező elektronokat, ekkor az átmenő elektronok intenzitása megnő. Amikor a kapillárison átjutott elektronok intenzitása egyensúlyi állapot közelébe kerül, akkor ezen részecskék átlagos energiája és az ahhoz tartozó energia-eloszlás félértékszélessége fázisban, illetve ellentétes fázisban van az intenzitással. A töltésfolt folyamatos növekedése, majd kisülése következtében, ellentétben az ionterelési mechanizmussal, stabil egyensúlyi állapot nem következik be, még nagy bemenő nyalábintenzitás esetén sem [71, 76].

A doktori értekezésemben tárgyalt eredmények egyértelműen azt mutatják, hogy a nanokapilláris mintánál felfedezett töltöttrészecske-terelő jelenség mikroszkopikus méretű, egyedi kapillárisoknál is megfigyelhető. Egy új lehetőség a töltött részecskék irányítására a töltött részecskék egyedi üvegkapillárison történő töltésállapot-változás nélküli önszerveződő átvezetése lehet. A szigetelő kapillárisokról szerzett eddigi ismereteink lehetőséget nyújtanak új ionvezetési technika kidolgozására. Az eddigieknél sokkal egyszerűbben és kevesebb anyagi befektetéssel lehet ion-optikai elemeket előállítani. Az ionnyaláb előállítása nem igényel vezérelhető tápegységet, és maguk az ionok építik fel egy önfenntartó folyamat során a fókuszáló teret.

Nanoméretű kiemelkedések szigetelő felületeken történő kialakítása jól meghatározott méretű nagytöltésű ionnyalábbal magában hordozza annak a lehetőségét, hogy a mélyebben fekvő kristályrétegek deformálása nélkül, szabályos struktúrákat tudjunk kialakítani a felületeken. Érdekes kihívás lehet nagytöltésű ionokkal rendezett mintázatú nanodombok kialakítása szigetelő felületeken.

A kapilláris ionterelő képessége a biológia és az orvoslás területén is felhasználható lehet. Egy egyedi üvegkapilláris segítségével nemcsak egy sejt, hanem annak egy meghatározott része is besugározható. Az üvegből készült minta előnye, hogy átlátszó, ezáltal a besugárzási pont közvetlenül megfigyelhető egy optikai mikroszkóp segítségével. Ez a lehetőség a kutatásokat a nehézionnal történő besugárzás biológiai hatásainak vizsgálata felé irányítja, amely az elmúlt

évtizedekben intenzíven kutatott területté vált. Mint orvosi alkalmazásnak, a nehézion terápiának, megvan az a nagy előnye, hogy a részecskék a Bragg csúcshoz közel eső energiát közvetlenül a tumorba juttatják, ezáltal minimális roncsolást okozva a környező szövetekben. A tumor nehéz-ionokkal történő besugárzásának kritikus kérdése, hogy mennyire tudjuk pontosan a megfelelő helyre eljuttatni a részecskéket. Ebben lehet szintén jelentős szerepe az egyedi üvegkapillárisoknak.

A doktori értekezésemben leírtak alapján egyértelmű, hogy még számos megválaszolatlan kérdés maradt a részecsketerelés mechanizmusával kapcsolatban. Így jól meghatározott terveink vannak a téma kutatásának folytatására. Vizsgálni fogjuk különféle külső elektromos térnek az ionterelés folyamatára gyakorolt hatását az általunk megtervezett speciális mintákkal. Ezáltal várhatóan növelni tudjuk az ionterelés hatékonyságát. Tervezzük egyszeresen töltött részecskék átvezetésének vizsgálatát egyedi szigetelő mikrokapillárissal. Vizsgálni fogjuk proton mikronyaláb terelődési mechanizmusát különféle egyedi, szigetelő mintákon keresztül. Nagy energiafeloldású mérések kivitelezését is tervezzük az elektrontranszport folyamatának további tanulmányozásához. Ehhez különféle szigetelő mintákat fogunk tervezni és készíteni. Vizsgálni fogjuk pozitron terelődési mechanizmusát egyedi kapillárisokon keresztül, egyrészt technikai alkalmazás céljából, másrészt azért, hogy jól fókuszált, nagy intenzitásu nyalábot állítsunk elő atomi ütközéses kísérletekhez, illetve antianyag előállításához.

Acknowledgements

I would like to thank all people who helped and encouraged me realizing this thesis during my years as a PhD student. First of all, I am indebted to my advisor Dr. Károly Tőkési for supervising my thesis and for his guidance in my research.

I would like to express my gratitude towards Prof. Friedrich Aumayr for the great possibility to join his group and to work together with his group. My special thanks are to Dr. Gregor Kowarik for the many useful discussions.

I highly appreciate the fruitful discussions with Prof. Joachim Burgdörfer related to the theoretical interpretation of my measured data.

I am grateful to Prof. John Tanis for inviting me to Kalamazoo to perform the electron guiding measurements in his group.

I am very thankful to Dr. Dezső Varga for his advice and ideas how to solve experimental difficulties.

I would like to thank Dr. József Pálinkás for his support that made it possible to attend two international conferences.

Most importantly, I express my sincere gratitude to my parents who have continuously supported me and have provided the foundations of what I am today.

Bibliography

[1] S. Ninomiya, Y. Yamazaki, F. Koike , H. Masuda, T. Azuma, K. Komaki, K. Kuroki, and M. Sekiguchi, Phys. Rev. Lett. **78** (1997) 4557.

[2] Y. Yamazaki, S. Ninomiya, F. Koike , H. Masuda, T. Azuma, K. Komaki, K. Kuroki, and M. Sekiguchi, J. Phys.Soc. Jpn. **65** (1996) 042902.

[3] K. Tőkési, L. Wirtz, C. Lemell, and J. Burgdörfer, Phys. Rev.A **64** (2001) 1199.

[4] K. Tőkési, L. Wirtz, C. Lemell, and J. Burgdörfer, Phys. Rev. A **61** (2001) 020901(R).

[5] K. Tőkési, L. Wirtz, C. Lemell, and J. Burgdörfer, Nucl. Instr. and Meth. Phys. Res. B. **164-165** (2000) 504.

[6] K. Tőkési, L. Wirtz, and J.Burgdörfer, Nucl. Instr. and Meth. Phys. Res. B. **154** (1999) 307.

[7] N. Stolterfoht, J.-H. Bremer, V. Hoffmann, R. Hellhammer, D. Fink, A. Petrov, and B. Sulik, Phys. Rev. Lett. **88** (2002) 201.

[8] R. Hellhammer, Z. D. Pesic, P. Sobocinski, D. Fink, J. Bundesmann, N. Stolterfoht, Nucl. Instr. and Meth. Phys. Res. B. **233** (2005) 213.

[9] Gy. Vikor, R.T. Rajendar Kumar, Z. D. Pesic, N. Stolterfoht, and R. Schuch, Nucl. Instr. and Meth. Phys. Res. B. **233** (2005) 218.

[10] M. B. Sahana, P. Skog, Gy. Vikor, R.T. Rajendar Kumar, and R. Schuch, Phys. Rev. A. **73** (2006) 040901(R).

[11] S. Matefi-Tempfli, M. Matefi-Tempfli, L. Piraux, Z. Juhasz, S. Biri, E. Fekete, I. Iván, F. Gall, B. Sulik, Gy. Vikor, J. Pálinkás, and N. Stolterfoht, Nanotechnology **17** (2005) 3915.

[12] P. Skog, I.L. Soroka, A. Johansson, and R. Schuch, Nucl. Instr. and Meth. Phys. Res. B. **258** (2007) 145.

[13] T. Ikeda, Y. Kanai, T. M. Kojima, Y. Iwai, T. Kambara, and Y Yamazaki, M. Hoshino, T. Nebiki and T. Narusawa, Applied Phys. Lett. **89** (2006) 163502.

[14] S. Das, B. S. Dassanayake, M. Winkworth, J. L. Baran, N. Stolterfoht, and J. A. Tanis, Phys. Rev. A. **76** (2007) 042716.

[15] A.R. Milosavljević, Gy. Víkor, Z. D. Pesić, P. Kolarz, D. Sević, B. P. Marinković, S. Mátéfi-Tempfli, M. Mátéfi-Tempfli, and L. Piraux, Phys. Rev. A **75** (2007) 030901(R).

[16] A. R. Milosavljevic, K. Schiessl, C. Lemell, K. Tőkési, M. Mátefi-Tempfli, S. Mátefi-Tempfli, B. P. Marinkovic, J. Burgdörfer, Nucl. Instr. and Meth. Phys. Res. B. **279** (2012) 190.

[17] K. Schiessl, W. Palfinger, K. Tőkési, H. Nowotny, C. Lemell and J. Burgdörfer, Phys. Rev. A. **72** (2005) 062902.

[18] K. Schiessl, K. Tőkési, B. Solleder, C. Lemell, and J. Burgdörfer, Phys. Rev. Lett. **102** (2009) 163201.

[19] K. Schiessl, PhD Dissertation, TU Wien (2009).

[20] E. Galutschek, R. Trassl, E. Salzborn, F. Aumayr and HP.Winter, Journal of Physics: Conf. Ser. **58** (2007) 395.

[21] M. Fürsatz, W. Meissl, S. Pleschko, I. C. Gebeshuber, N. Stolterfoht, HP. Winter, and F. Aumayr, J. Phys. Conf. Proc. of HCI **58** (2007) 319.

[22] L. Kövér, D. Varga, I. Cserny, J. Tóth, K. Tőkési, Surf. Interface Anal. **19** (1992) 9.

[23] D.A. Dahl, J. Mass Spectr. **200** (2000) 3.

[24] A. Cassimi, T. Muranaka, L. Maunoury, H. Lebius , B. Manil, B.A. Huber, T. Ikeda, Y. Kanai, T. M. Kojima, Y. Iwai, T. Kambara, Y. Yamazaki, T. Nebiki, and T. Narusawa, Int. J. Nanotechnol. (2008) 5.

[25] P. Skog, HQ. Zhang, and R. Schuch, Phys. Rev. Lett. **101** (2008) 223202.

[26] J. Burgdörfer, P. Lerner, and F. W. Meyer, Physical Review A **44** (1991) 5674.

[27] L. P. Ratliff, E. W. Bell, D. C. Parks, A. I. Pikin, and J. D. Gillaspy, Appl. Phys. Lett. **75** (1999) 590.

[28] E. Akcöltekin, T. Peters, R. Meyer, A. Duvenbeck, M. Klusmann, I. Monnet, H. Lebius and M. Schleberger, Nature Nanotechnol. **2** (2007) 290.

[29] A. S. El-Said, R. Heller, W. Meissl, R. Ritter, S. Facsko, C. Lemell, B. Solleder, I. C. Gebeshuber, G. Betz, M. Toulemonde, W. Möller,2 J. Burgdörfer and F. Aumayr, Phys. Rev. Lett. **100** (2008) 237601.

[30] R. Heller, S. Facsko, R. A. Wilhelm, and W. Möller, Phys. Rev. Lett.**101** (2008) 096102.

[31] T. Schenkel, J. Meijer, A. Persaud, J. W. McDonald, J. P. Holder, and D. H. Schneider, J. Vac. Sci. Technol. B **20** (2002) 2819.

[32] J. J. L. Morton, A. M. Tyryshkin, R. M. Brown, S. Shankar, B. W. Lovett, A. Ardavan, T. Schenkel, E. E. Haller, J. W. Ager and S. A. Lyon, Nature **455** (2008) 1085.

[33] Y. Iwai, T. Ikeda, T.M. Kojima, Appl. Phys. Lett. **92** (2008) 023509.

[34] F. Aumayr, H. Kurz, D. Schneider, M. A. Briere, J. W. McDonald, C. E. Cunningham, and HP. Winter , Phys. Rev. Lett. **71** (1993) 1943.

[35] T. Neidhart, F. Pichler, F. Aumayr, H.P. Winter, M. Schmid, P. Varga, Nucl. Instrum. Methods Phys. Res., Sect. B **98** (1995) 465.

[36] M. Tona, H. Watanabe, S. Takahashi, N. Nakamura, N. Yoshiyasu, M. Sakurai, T. Terui, S. Mashiko, C. Yamada, S. Ohtani, Surf. Sci. **601** (2007) 723.

[37] R. Nakayama, M. Tona, N. Nakamura, H. Watanabe, N. Yoshiyasu, C. Yamada, A. Yamazaki, S. Ohtani, M. Sakurai, Nucl. Instrum. Methods Phys. Res., Sect. B **267** (2009) 2381.

[38] H. Q. Zhang, P. Skog, and R. Schuch, Phys. Rev. A **82** (2010) 052901.

[39] C. Lemell, A. S. El-Said, W. Meissl, I. C. Gebeshuber, C. Trautmann, M. Toulemonde, J. Burgdörfer and F. Aumayr, Solid-State Electron. **51** (2007) 1398.

[40] C. Lemell, K. Schiessl, H. Nowotny, and J. Burgdörfer, Nucl. Instrum. Methods Phys. Res., Sect. B **256** (2007) 66.

[41] J. Waclalawek, Projektarbeit, TU Wien (2011) unpublished.

[42] A.K. Jonscher, Journal of Physics D: Applied Physics **32** (1999) R57.

[43] P. Love, J. Phys. C Solid State **16** (1983) 5985.

[44] M. Tona, Y. Fujita, C. Yamada, and S. Ohtani, Phys. Rev. B **77** (2008) 155427.

[45] W. Meissl, M. C. Simon, J. R. Crespo López-Urrutia, H. Tawara, J. Ullrich, HP. Winter and F. Aumayr, Rev. Sci. Instrum. **77** (2006) 093303.

[46] F. Aumayr, A. S. El-Said, and W. Meissl, Nucl. Instrum. Methods Phys. Res., Sect. B **266** 2729 (2008).

[47] J. Harris and R. O. Jones, Journal of Physics C **7** (1974) 3751.

[48] P. M. Echenique and J. B. Pendry, Journal of Physics C, **8** (1975) 2936.

[49] P. M. Echenique, R. H. Ritchie, N. Barber´an, and J. Inkson, Physical Review B **23** (1981) 6486.

[50] N. Stolterfoht, R. Hellhammer, Z. Juhász, B. Sulik, V. Bayer, C. Trautmann, E. Bodewits, A.J. de Nijs, H.M. Dang, and R. Hoekstra, Phys. Rev. A **79** (2009) 042902.

[51] Y. Kanai, M. Hoshino, T. Kambara, T. Ikeda, R. Hellhammer, N. Stolterfoht, and Y. Yamazaki, Phys. Rev. A **79** (2009) 012711.

[52] W. Wang, D. Qi, D. Yu, M. Zhang, F. Ruan, J. Chen and X. Cai, J. Phys.: Conf. Ser. **163** (2009) 012093.

[53] S. Das, B.S. Dassanayake, N. Stolterfoht, and J. A. Tanis, Rev. Mex. Fis. S **56** (2010) 66.

[54] N. Stolterfoht, R. Hellhammer, J. Bundesmann, D. Fink, Y. Kanai, M. Hoshino, T. Kambara, T. Ikeda and Y. Yamazaki, Phys. Rev. A **76** (2007) 022712.

[55] M. B. Sahana, P. Skog, Gy. Víkor, R. T. Rajendra Kumar, and R. Schuch, Phys. Rev. A **73** (2006) 040901(R).

[56] H. F. Krause, C. R. Vane and F. W. Meyer, Phys. Rev. A **75** (2007) 042901.

[57] H. Seiler, J. Appl. Phys. **54**, R1 (1983).

[58] N. Bundaleski, H. Khemliche, P. Rousseau, A. Cassimi, L. Maunoury and P. Roncin, J. Phys.: Conf. Ser. **133** (2008) 012016.

[59] R. Hellhammer, D. Fink, and N. Stolterfoht, Nucl. Instrum. Methods Phys. Res. B **261** (2007) 149.

[60] G. P. Pokhil, K. A. Vokhmyanina and A. I. Mironchik, Jour. Surf. Investigation: X-ray, Sync, Neut. Tech. **3** (2009) 326.

[61] G. P. Pokhil, A. I. Mironchik, L. A. Zhilyakov, T. Ikeda, Y. Yamazaki, Bulletin of the Russian Academy of Sciences: Phys. 74, No. **2** (2010) 221.

[62] A. Arnau, F. Aumayr, P.M. Echenique, M. Grether, W. Heiland, J. Limburg, R. Morgenstern, P. Roncin, S. Schippers, R. Schuch, N. Stolterfoht, P. Varga, T.J.M. Zouros, and HP. Winter, Surf. Sci. Rep. **27** (1997) 113.

[63] Z.G. Song, C.K. Ong, and H. Gong, Appl. Surf. Sci. **119** (1997) 169.

[64] A. Cassimi, L. Maunoury, T. Muranaka, B. Huber, K. R. Dey, H. Lebius, D. Lelievre, J. M. Ramillon, T. Been, T. Ikeda, Y. Kanai, T. M. Kojima, Y. Iwai, Y. Yamazaki, H. Khemliche, N. Bundaleski and P. Roncin, Nucl. Instrum. Meth. Phys. Res. B **267** (2009) 674.

[65] S. Matefi-Tempfli, M. Matefi-Tempfli, L. Piraux, Z. Juhasz, S. Biri, E. Fekete, I. Ivan, F. Gall, B. Sulik, Gy. Vikor, J. Palinkas, and N. Stolterfoht, Nanotechnology **17** (2005) 3915.

[66] R.J. Bereczky, G. Kowarik, F. Aumayr and K. Tőkési, Nucl. Instr. and Meth. B **267** (2009) 317.

[67] R.J. Bereczky, G. Kowarik, K. Tőkési and F. Aumayr, Nucl. Instr. and Meth. B. **279** (2012) 182.

[68] Kowarik, R.J. Bereczky, F. Aumayr and K. Tőkési, Nucl. Instr. and Meth. B **267** (2009) 2277.

[69] G. Kowarik, R.J. Bereczky, F. Ladinig, D. Schrempf, C. Lemell, J. Burgdörfer, K. Tőkési and F. Aumayr, arXiv: 1109.3953v1.

[70] B.S. Dassanayake, S. Das, R.J. Bereczky, K. Tőkési, J.A. Tanis, Phys. Rev. A **81** (2010) 020701(R).

[71] B.S. Dassanayake, R.J. Bereczky, S. Das, A. Ayyad, K. Tőkési and J.A. Tanis, Phys. Rev. A **83** (2011) 012707.

[72] B.S. Dassanayake, S. Das, A. Ayyad, R.J. Bereczky, K. Tőkési and J.A. Tanis, Nucl. Instr. and Meth. B **269** (2011) 1243.

[73] Accepted ITS LEIF proposal, No: P09076A(2009).

[74] R.J. Bereczky, B.S. Dassanayake, S. Das, K. Tőkési, J. A. Tanis, Journal of Physics: Conference Series **194** (2009) 2014.

[75] R.J. Bereczky, G. Kowarik, C. Lemaignan, F. Aumayr, K. Tőkési, Journal of Physics: Conference Series **194** (2009) 2019.

[76] B.S. Dassanayake, S. Das, R.J. Bereczky, K. Tőkési, J. A. Tanis, Journal of Physics: Conference Series **194** (2009) 2011.

[77] B.S. Dassanayake, S. Das, R.J. Bereczky, K. Tőkési, J.A. Tanis, Journal of Physics: Conference Series **194** (2009) 2016.

[78] R.J. Bereczky, G. Kowarik, C. Lemaignan, A. Macé, F. Ladinig, R. Raab, F. Aumayr, and K. Tőkési, CAARI 2010 AIP (2011) 119.

[79] R.J. Bereczky, G. Kowarik, C. Lemaignan, F. Aumayr, K. Tőkési, Journal of Physics: Conference Series **194** (2009) 2019.

[80] Z. Juhász, B. Sulik, R. Rácz , S. Biri, R.J. Bereczky, K. Tőkési, Á. Kövér, J. Pálinkás, N. Stolterfoht, Phys. Rev. A **82** (2010) 062903.

[81] K. Tőkési, I. Rajta, R.J. Bereczky, K. Vad, Nucl. Instr. and Meth. B. **279** (2011) 173.